Department of Mechanical Engineering

The University of Sheffield

Fatigue crack characterization by image correlation

A thesis submitted for the degree of Doctor of Philosophy

by

Pablo López-Crespo

March 2007

IMAGING SERVICES NORTH
Boston Spa, Wetherby
West Yorkshire, LS23 7BQ
www.bl.uk

PAGE HAS NO CONTENT

PAGINATED BLANK PAGES ARE SCANNED AS FOUND IN ORIGINAL THESIS

NO INFORMATION IS MISSING

Summary

The structural integrity of many materials from aircraft structures, pressure vessels and offshore structures is closely related to the cracks existing in the component. The stress intensity factor is widely recognized as a major parameter for assessing the severity of a crack, and is extensively used in fatigue lifetime predictions. This work presents a new methodology for experimental determination of the effective stress intensity factor from image correlation data. In addition, the methodology allows the reconstruction of the full stress field. Based on a multi-point over-deterministic method, the full-field displacement information collected from the neighbourhood of the crack tip is combined with an elastic model based on Muskhelishvili's complex variable formulation to determine the opening and the sliding mode stress intensity factors. Utilization was made of edge-finding routines for locating the crack tip coordinates from the displacement fields. The technique was applied successfully to study real fatigue cracks in different aluminium alloy specimens, subjected to static and cyclic loads. Good agreement was also obtained for a crack emanating from a hole, where complex passing stress fields exist. Different factors such as crack face contact and rubbing effects, local mixed-mode arising from wedge opening or tilting of the crack front are identified as being responsible for the differences between the nominal and measured values. Finally the non-contacting tool was extended to the analysis of crack face interaction and crack closure problems, and it was found to be able to estimate the opening load.

Contents

Acknowledgements

I would like to acknowledge my two academic supervisors Professor Eann A. Patterson and Professor John R. Yates for encouragement, guidance and mind-stimulating discussions.

I would also like to thank Dr Anton Shterenlikht for all the help given in the different stages of the PhD and for sharing generously his knowledge with me.

Thanks are also due to Professor Phil J. Withers and Dr Richard L. Burguete for their many scientific contributions to this work.

I am also very grateful to Zineb Saghi and Silvio Sorrentino for the help provided in analytical and programming subjects.

Dr João Quinta da Fonseca, Dr Rachel A. Tomlinson, Dr Richard J. Greene, Professor George C. Sih and Professor Akio Otsuka are also gratefully acknowledged for their kindness in sharing their expertise with me when requested.

Thanks are also given to Richard Kay for all his help in the workshop and to Jean A. Hoskins for helping me in many departmental issues.

Many thanks also to my *fatigue colleagues*, Philip Siegmann, Paco Díaz, Dave Asquith, Sabino Ayvar, Rubén Cuamatzi, Martín Castillo and Han Tai for interesting discussions and help provided throughout this period.

Last, but not least, I would like to thank my parents, Inmaculada and Anselmo, my sister Cristina and my brothers Enrique and Anselmo for their continuous support.

Nomenclature

α_k, β_k	real and imaginary parts of complex coefficient a_k
γ	contour in the mapping plane
δ	crack opening displacement
ΔK_{eff}	effective stress intensity factor range
ζ	complex coordinate in the mapping plane
η	complex coordinate on the contour in the mapping plane
μ	shear modulus, $\mu = \frac{E}{2(1+\upsilon)}$
υ	Poisson's ratio
ϱ	relative residual
σ_{cl}	closure stress
σ_{max}	maximum applied stress
σ_{min}	minimum applied stress
σ_{op}	opening stress
σ_y	yield stress
Σ	diagonal matrix employed in the singular value decomposition
φ, ψ	Muskhelishvili's analytical functions
χ	function of Poisson's ratio
$\omega(\zeta)$	conformal function
Ω	function of the conformal mapping, $\Omega = \frac{\omega}{\overline{\omega'}}$
a	crack half-length
a_k, b_k, c_k	complex coefficients for Fourier series representation
A	coefficient matrix of the system of equations Ax = b

b	right-hand side vector of the system of equations Ax = b
C_k^j, D_k^j	
E_k^j, F_k^j	coefficients dependent of point j
cond(A)	condition number of matrix A
E	Young's modulus
F	error function
g	major semi-axis of an ellipse
h	minor semi-axis of an ellipse
i	square root of -1
I(x, y)	image intensity function
j	collected displacement data point
k	summation index in Fourier series
K_I	opening mode stress intensity factor
K_{II}	sliding mode stress intensity factor
K_{III}	antiplane shear mode stress intensity factor
K_{min}	stress intensity factor at minimum load
K_{max}	stress intensity factor at maximum load
K_{th}	threshold stress intensity factor range
L	contour in the physical plane
m	shape parameter in conformal function
N	limit in Fourier series
p	maximum number of collected displacement data points
P	applied load
P_{cl}	applied load at closure
P_{op}	applied load at opening
q	parameter measuring the difference between infinite series and truncated series
r, θ	polar coordinates
r_p	Irwin approximation of the extend of the plastic zone
R	scale parameter in conformal function
s	singular values of matrix A
u, v	horizontal and vertical displacements

U, V	orthogonal matrixes employed in the singular value decomposition
x, y	rectangular coordinates
z	complex coordinate in the physical plane, $z = x + iy$

Chapter 1

Introduction

1.1 Motivation for the research

Current design of engineering structures demands an increasingly precise knowledge of the damage occurring during service in the materials. Due to lack of accurate knowledge, in order to assure structural integrity, large safety factors are traditionally employed. This leads to an increasing weight and not optimized structures which very often, as in the case of aircraft industry, means important economic losses. The stress intensity factor (SIF) is one of the most widely used parameters for the assessment of defects or cracks and fatigue crack growth characterization. However the difficulties associated with its measurement oblige frequently to develop finite element models which become increasingly more time consuming as the geometry and the state of stress become more complex. The aim of this thesis is to develop a methodology to calculate from experiment the SIF and in general, to establish a tool for characterizing cracked structures. The methodology will combine an advantageous experimental technique such as image correlation with a very powerful Muskhelishvili's complex function analysis.

1.2 Scope of the thesis

Under small-scale yielding conditions the SIF can be used to describe crack tip stress and strain fields that are dominated by a ($r^{-0.5}$) singularity, where r is the distance to the crack tip, measured in the radial direction. If significant plastic deformation occurs, the linear elastic model ceases to describe the crack tip response and

Hutchinson-Rice-Rosengren (HRR) singular field, ($r^{-1/(1+n)}$) becomes the most suitable, where n is the strain hardening coefficient. If the crack tip plasticity is increased further, the region of very large plastic deformation associated with crack tip blunting swamps the HRR region and analysis becomes difficult. Local damage models or a global CTOA are used by the fracture community in such situations.

The aim of the current research is to study crack problems only from an elastic viewpoint. Accordingly utilization is made of the Linear Elastic Fracture Mechanics, and so the elastic field is assumed to be dominant over the HRR or higher strain fields. Both large strain and HRR-dominated zones will be well-contained within the region of K-dominance, and the plastic zone will be small compared with the crack size.

1.3 Context of the project

In the last 15 years, several research projects, closely related to the current one, were carried out in the Department of Mechanical Engineering at the University of Sheffield. In all the cases cracked structures were studied by means of different experimental techniques, namely photoelasticity, Moiré interferometry, caustics and thermoelastic stress analysis. The common goal shared by all these projects was the experimental extraction of quantitative information describing the crack driving force.

The important progress in the last few years in developing optical correlation algorithms, made image correlation a fast, robust and easy-to-use technique for displacement or strain measurement.

The present project is a logical continuation of the aforementioned research field developed in the department, extended to the increasingly important experimental technique of image correlation.

The work presented in this thesis was sponsored by the Engineering and Physical Sciences Research Council (EPSRC, grant GR/S18045/01) from UK and Airbus UK. The work fits within a collaborative project between the University of Sheffield and the University of Manchester. Accordingly, sections 3.1 to 3.5 were developed under the supervision of Dr Anton Shterenlikht from the University of Manchester.

1.4 Description of contents

A survey of the literature is presented in Chapter 2, which is subdivided into three sections. The first one explains diverse analytical and experimental approaches for SIF determination. The second one introduces some basic concepts of fatigue crack closure and discusses different methods employed for its measurement. The last section of Chapter 2 describes very briefly some of the principles of the image correlation technique. In Chapter 3 a mathematical model, based on Muskhelishvili's formulation, for obtaining the SIF from displacement information is developed and then verified with simulated data. Some steps of the analytical developments are omitted from this chapter and moved to the appendixes in order to make more fluent the reading of the chapter.

An accurate description of the equipment and methods is given in Chapter 4, including a justification of the materials and specimens and an explanation of the apparatus employed during the experimental tests.

In the following three chapters different experimental results together with pertinent discussion and conclusions are unfolded. Chapter 5 presents the methodology for finding the location of the crack tip. In Chapter 6 the results of applying the elastic model developed in Chapter 3, combined with the procedure for locating the crack tip from Chapter 5 to three types of cracked specimens are shown. The tool is then extended in Chapter 7 to the analysis of fatigue crack closure phenomena.

Chapter 8 includes a general discussion providing an overview of the work, followed by some recommendations for future work. Finally in Chapter 9 the major conclusions are drawn.

Chapter 2

Literature review

2.1 Review of the methods for estimating the stress intensity factor

2.1.1 Analytical methods

The elastic stress and displacement fields in an infinite plate containing an elliptical hole under uniform normal stress at infinity, were determined by Inglis in 1913 [1]. It was found that the stress near the tip of a flaw or notch can be many times greater than the applied stress at infinity.

The solutions most commonly used for stresses and displacements confined to a small region in the vicinity of a crack-tip [2], were developed from Westergaard's stress function [3]. These can be found in their most standard form in many fracture mechanics texts (see for example [4]).

In 1966 Sih [5] demonstrated using Muskhelishvili's (sometimes referred to as Goursat-Kolosov's) complex representation of the plane problem, that a real constant term is assumed to be zero in Westergaard's equations. Furthermore he showed that this constant term should be calculated from the boundary conditions. He also proposed a modified Westergaard's formulation where the apparent error was rectified. Later, the source of this omission was traced [6] to an earlier work, which Westergaard based his equations on. Starting from Muskhelishvili's representation, the modified Westergaard's equations were deduced, including the constant term which was lacking according to Sih [5]. Subsequently it was demonstrated with photoelastic results [7-9] that both the original Westergaard's and

the modified Westergaard's equations are a specific case of a more general formulation, because they cannot take into account geometry boundary conditions. The difference between both approaches has been quantified and examples have been given of situations where the use of Westergaard's equations leads to qualitatively incorrect results in pure mode I [10] and varying the level of I + II mixity [11].

The complex variable methods popularized by Muskhelishvili [12] provide the flexibility to solve plane crack problems with stress field modified by any geometrical boundary [8]. That is, they are able to solve accurately crack problems with initially non-uniform passing stress fields, where the non-uniformity is created by the boundaries [13]. This allows cracks growing in the vicinity of stress raisers, such as geometric features, and singularities such as other cracks or contact to be characterised.

The method of Muskhelishvili was initially used for evaluating the state of stress in different geometries with cracks [14]. Later on, the approach was extended to stress intensity factor (SIF) calculations, and the closed expressions for SIF were obtained as a function of geometry parameters and load applied to the body for progressively more complex problems: rectangular tensile sheet with symmetric edge cracks [15], circular disk with an internal crack under a loading of external hydrostatic tension [16], central crack in a rectangular panel [17], slant crack in a plate submitted to a biaxial load [11], curved crack in an infinite sheet under biaxial tension, crack in an infinite plate subjected to uniform biaxial bending [18], etc.

2.1.2 Experimental methods

Great effort has been devoted over the past 50 years to studying the stress distribution ahead of a crack tip and to estimating experimentally the SIF, with optical techniques being probably the most utilized. Within them, photoelasticity is the most popular and oldest. The first works [19-20] did not mention specifically the term SIF because it was not introduced until some years later, but they calculate stresses near a crack tip, for a stationary as well as for a running crack. Initially all the methods employed data from only one or two points in the fringe field and did not

fully utilize all the information available. These methods were found to be highly sensitive to inaccuracies when measuring the fringe order and the coordinates of the points employed. In 1979, the advent of desktop computers allowed a large number of spatially distributed data to be used, and the multiple-point over-deterministic method (MPODM) [21] was developed. The method involves a fitting of the theoretical stress field to arbitrarily chosen photoelastic data. The resulting over-determined set of equations was solved with a Newton-Raphson iterative method in order to calculate both the mode I and mode II SIF.

Since then, the MPODM has been the preferred method and the SIF has been calculated from isochromatic fringe patterns in opening mode [22-23, 29], in-plane shear mode[24-28], and out-of-plane shear mode problems [30-32], dynamic analyses [33-34], contact problems [35-36], interfacial cracks in bi-materials [37-38], functionally gradient materials [34] and has been applied to studies of crack closure [39 and 29].

Subsequently the method was extended to other techniques, such as thermoelastic stress analysis. The principal advantage of thermoelasticity is that the K-dominated zone can be readily recognised, and the data points can be collected in the region where the stress field descriptor is valid. The method was first developed in pure mode I [40] and then extended to mode II loading [41]. The methodology was later combined with the MPODM and quite accurate results were reported with different thermoelastic equipments, in mixed mode conditions [42, 28 and 43]. In addition the technique was found to be sensitive to the effects of crack closure and the presence of tensile and compressive residual stresses.

In the case of caustics, the methodology for SIF calculation is based on the geometrical measurement of the shadow patterns generated with the technique. The pure tension mode SIF can be obtained from a single measurement of the generated curve [44, 45 and 28] while the mixed mode case involves a non-linear least squares analysis to extract K_I and K_{II} from the dimensions of the curve [46].

The SIF has also been calculated from displacement-field patterns obtained with Moiré interferometric techniques [47-48]. The method used a least squares fit of the stress field equations describing the horizontal displacements for solving for K_I. It

also included a modification of the MPODM to eliminate the effect of rigid body motion and also the need for absolute fringe calibration.

The same approach employed for Moiré interferometry [47] has been utilized for measuring the pure mode I SIF with electronic speckle pattern interferometry (ESPI) [49 and 48]. More recently, ESPI data was also used for SIF determination, with an intermediate conversion into stress fields [50].

All the aforementioned techniques present important drawbacks. Photoelasticity requires either plastic models of birefringent material, in the case of transmission photoelasticity, or the bonding of polymer coating to the specimen to be assessed, in the case of reflection photoelasticity. In thermoelasticity only a uniformly emissive surface is needed, but the technique is dependent on the application of cyclic loading, to maintain adiabatic conditions, which must be locked in with a very sensitive infrared sensor. The second main handicap of thermoelastic stress analysis lies in the high price of the equipment. The optical method of caustics requires a flat surface that must be polished to a mirror finish. In Moiré interferometry a grating must be bonded to the object, which needs to be flat in the area of interest. The major disadvantages of ESPI are the high cost of the equipment and the stringent necessity for vibration isolation of the experimental setup, which is often difficult to achieve in the vicinity of the testing machines. All these practical problems are summarized in Table 2.1.

By contrast, image correlation requires no surface preparation or anything to be bonded to the surface, and no special loading regime is needed. In addition it is very cheap, fast and much easier to apply experimentally than the above techniques.

The first time the SIF determination by mean of image correlation was addressed was in 1987 [51]. In that work, the MPODM [21] was applied to displacement fields in a way similar to [47]. An error function was built for each collected displacement, considering the differences between theoretical value predicted by Westergaard solution and the measured value obtained with image correlation. The K_I was left as an unknown to be solved. A total error function was constructed so that all the captured points are taken into account. By using the first derivative of the total error function equated to zero, the K_I was obtained as the value that minimizes the total error function. This procedure was applied to a C-shaped and a three-point bend

Plexiglass specimens, and relatively scattered results were obtained in calculating the

Technique	**Disadvantages**
Photoelasticity	-Requires either plastic models or the bonding of polymer coating to the object
Thermoelasticity	-Needs cyclic load -Expensive apparatus
Caustics	-Requires a flat surface that must be polished to a mirror finish
Moiré	-Requires a grating to be bonded to the object
ESPI	-Needs to be isolated from vibrations -Expensive apparatus

Table 2.1: Main disadvantages of other experimental stress analysis techniques compared with image correlation.

pure mode I SIF. Although an error is produced by not correctly locating the crack tip [47], no methodology was described for finding the crack tip coordinates. In addition, the K_I values were estimated uniquely from displacements perpendicular to the crack face, thus ignoring all the information contained in the displacements parallel to the crack face. For this reason the proposed approach was valid for strictly opening mode, and any mode II effects could not be taken into account.

Moreover, the performance of image correlation algorithms at that time was not as accurate as at present, as can be seen in Figure 2.1, where large displacement errors exist in the vicinity of the crack.

In spite of all these criticisms, this early work [51] set up the basis of the SIF determination with image correlation.

By considering both displacement fields perpendicular and parallel to the crack face, an attempt was made to extend the approach to mixed mode SIF calculation [52]. The results were compared with photoelasticity, and satisfactory results were only

found in the opening mode component of the SIF. The uncertainty in the crack tip position was avoided by assuming a machined 1.4-mm hole to be the crack tip.
As the image correlation algorithms were becoming more and more accurate, increasingly more research was carried out to determine the SIF from image correlation data, in heterogeneous [53-54] and homogeneous [55-56] materials.

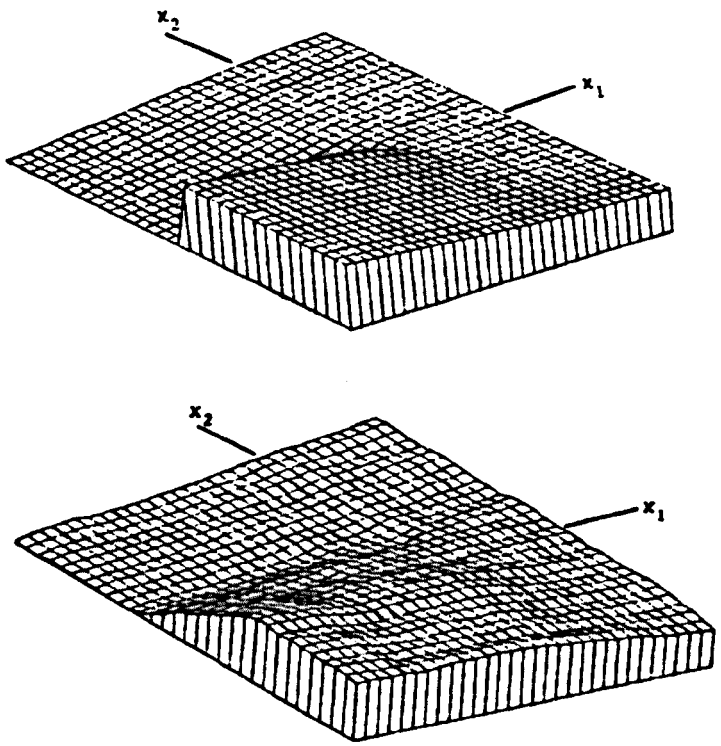

Figure 2.1: Displacement fields in the vicinity of a crack. Top: theoretical vertical displacements, and bottom: vertical displacements measured by image correlation. (After McNeill et al. 1987).

Hild and Roux [55] paid attention to the crack tip location. An iterative method was employed to estimate the position of the crack tip, where an objective error function was evaluated and the tip coordinates were found to minimize the differences between the displacements predicted by the analytical solution and the measured displacements. The approach was applied to a naturally sintered ceramic (silicon carbide). The ceramic beam specimen was sandwiched between two steel beams and subjected to a three-point bend test. The resulting state of stress in the vicinity of the

crack was affected by the friction of the contact surfaces between the ceramic sample and the steel beams. Again, satisfactory results were obtained only in the mode I SIF. Yoneyama et al. [56] included the crack tip coordinates as unknowns in a Newton-Raphson iterative method, for calculating the opening and edge sliding modes SIF at different mixed mode conditions. The mathematical model adopted was that of Westergaard, which was demonstrated to be less general than the Muskhelishvili's approach employed in this thesis. The authors used a compliant brittle polymethylmethacrylate (PMMA) model material and its surface was first painted with black ink and then covered with a white dot pattern using spray painting, so that a speckle-like pattern was created. A blunt, 0.25 mm radius, notch was introduced, instead of a sharp fatigue crack, that was employed in this thesis. The fact of studying a notch instead of a fatigue crack over-simplifies the problem, and makes the task of finding the crack tip easier.

The great majority of works where the SIF was calculated experimentally, used the series of equations of the Westergaard's type, and only some works utilized the complex variable formulation of Muskhelishvili, maybe because the latter are less standardized and more intricate than the former [11]. In the case of displacement data, such as those provided by image correlation, to the knowledge of the author, no work has been reported using Muskhelishvili's complex function approach. Only the author and his co-workers [50] used the displacement fields to estimate the SIF. However, in that case the displacements were converted into strains via spatial differentiation and finally the stresses were calculated from the strains by making use of Hooke's law. The resulting stress fields were fitted in a mathematical model, previously developed for photoelasticity [26], to extract the SIF. The numerical differentiation is an inherently noisy process, and performing two transformations upon the raw data introduces errors. To avoid these unnecessary sources of errors, it was proposed to use the Muskhelishvili's formulation in terms of displacements.

2.1.3 Conclusions

Experimental techniques have proved very advantageous in determining the SIF in structures and components for which no theoretical or numerical solution is available.

Recently, image correlation technique has matured into a stable and reliable method for measuring the displacement fields. In the last few years, the technique has started to be applied in the field of Linear Elastic Fracture Mechanics. As a consequence, increasingly better results have been obtained in the SIF determination with image correlation. However, the few published works are limited by the application of a simplified crack tip stress field, i.e. Westergaard's solution, where the influence of the boundary conditions is ignored. Moreover, the authors also used artificially generated cracks in compliant materials instead of sharp fatigue cracks, in uniform passing stress fields.

Geometrical boundary conditions can be accounted for with Muskhelishvili complex formulation. However, all the works that used Muskhelishvili's approach, developed expressions in term of stresses. Therefore, in order to use the data from image correlation, the expression for SIF calculation need to be developed in terms of displacements. To the knowledge of the author, no previous work linked SIFs with displacement fields following Muskhelishvili's approach.

2.2 Review of the methods for evaluation of fatigue crack closure

2.2.1 Mechanism of fatigue crack closure

The concept of crack closure was first introduced by Elber in 1970 [57-58]. According to the author, a fatigue crack in a body subjected to tension-tension cyclic load, is completely open only at high load levels, that is, at low load levels a fraction of the crack near the tip remains closed throughout both the loading and unloading

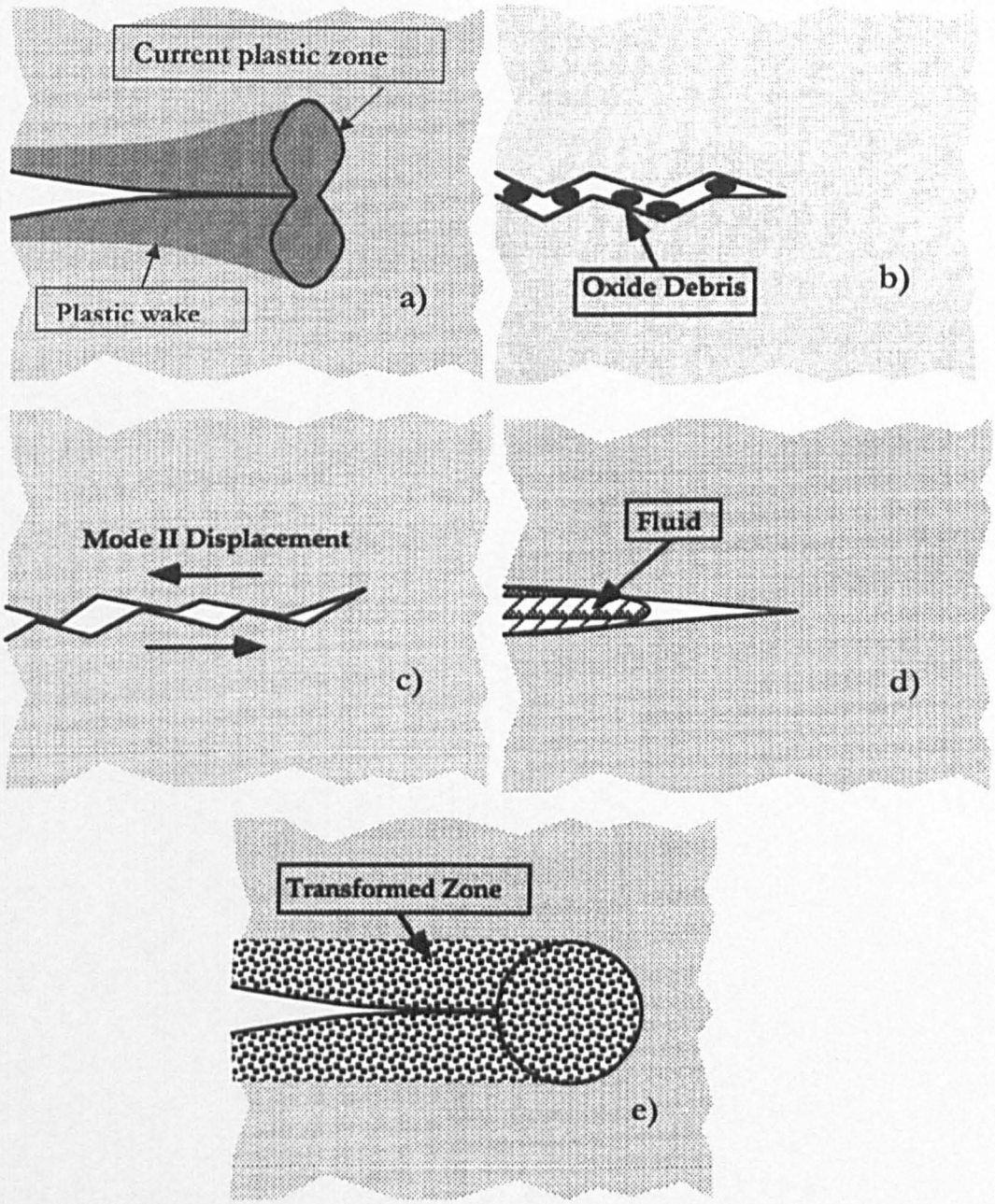

Figure 2.2: Schematic illustration of the different crack closure mechanisms: a) plasticity-induced crack closure, b) oxide-induced crack closure, c) roughness-induced crack closure, d) viscous fluid-induced crack closure and e) phase transformation-induced crack closure.

phase of the cycle. Elber explained the phenomenon as residual tensile deformation left in the wake of the crack tip while it grows. This first closure mechanism was termed plasticity-induced crack closure. Later, additional sources of closure were identified, arising from corrosion layers formed within a fatigue crack, microscopic

roughness of the fatigue fracture surfaces, viscous fluids penetrated inside the crack and stress- or strain-induced phase transformations at the crack tip [59]. Consequently four more closure mechanisms were recognized, associated to the different sources of closure respectively, namely oxide-induced crack closure, roughness-induced crack closure, viscous fluid-induced crack closure and phase transformation-induced crack closure. These are illustrated in Figure 2.2. As can be seen in the figures, the different mechanisms are a consequence of the response of the material not only at the crack tip and ahead of the fatigue crack, but also in the wake of the crack.

A sharp crack in a perfectly linear elastic body closes only when zero load is reached or under compressive load. However, the fact that materials are not perfectly elastic, imply the existence of a plastic component in the deformations. The propagation of a fatigue crack yields a wake of material plastically deformed, and as the crack grows, residual tensile strains remain in the material behind the advancing crack tip, as can be appreciated in Figure 2.2.a.

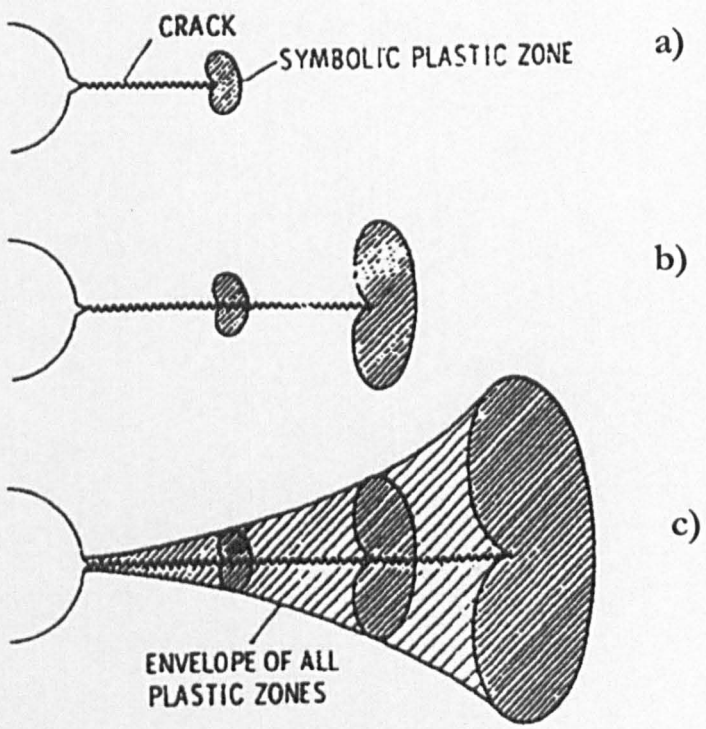

Figure 2.3: Scheme of the development of an envelope of prior plastic zones around an advancing fatigue crack. (After Elber 1971).

If the crack growth is happening under constant amplitude, crack growth will imply an increase in the stress intensity factor range and therefore in the size of the plastic zone. Figure 2.3 shows the enlargement of the plastic zone for three different crack lengths, and the envelope of plasticity in the wake (Figure 2.3.c). By monitoring the applied stress and measuring the evolution during a cycle of the displacement above and below the plane of the crack, just behind the crack tip, the effect of plasticity-induced crack closure can be brought into view.

Figure 2.4 shows schematically the relation obtained between the applied stress, σ, and the displacement, δ. In the first section (region A-B in Figure 2.4) a linear behaviour is observed, which is equal to the stiffness of the same material with an ideal notch. That is, in the unloading phase, the fatigue crack stays fully open until the nominal stress decreases from the maximum stress, σ_{max} to the closure stress, σ_{cl}. The increase in stiffness shown between B and C is related to the change from crack fully open to closed crack. In the last stage of the unloading, between C and D, the curve σ-δ shows again a linear behaviour, being the slope of C-D identical to the stiffness of the same material without fatigue crack. However, in closure studies, it is common practice to use the concept of compliance instead of the stiffness. The compliance of a cracked body is defined as the inverse of the stiffness.

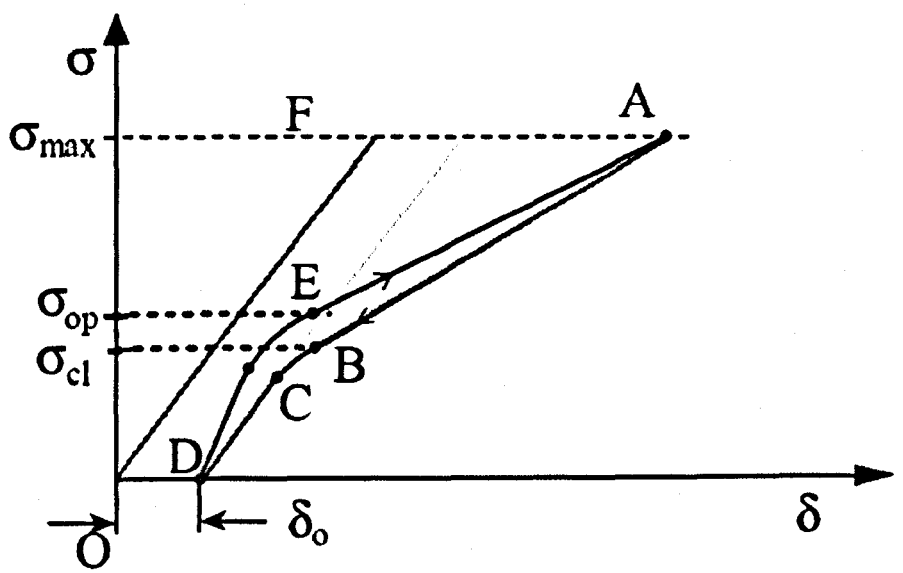

Figure 2.4: Schematic of the relationship between the applied stress and the displacement measured with strain gauges when premature contact between the crack faces occurs. The difference between opening and closing stresses is also illustrated.

During the loading phase of the cycle, although the relation between the applied stress and the displacement is similar to that during the unloading phase, it is not exactly the same. This fact yielded a distinction between the closure stress, σ_{cl}, and the opening stress, σ_{op} (see Figure 2.4).

The linear behaviour of the upper part of the curve (region AB in the unloading phase or region EA in the loading phase) is observed when no growth or significant plastic deformation is occurring. If loads which can produce significant plastic deformation and crack growth are applied (region above A not shown in Figure 2.4), a further increase in compliance may appear [60].

The oxide-induced crack closure occurs when the presence of humidity produces oxidation of the recently formed fracture surfaces during fatigue crack growth, Figure 2.2.b. During near-threshold crack growth, at low amplitudes of cyclic crack tip opening displacements, the existence of local mixed mode crack opening, microscopic roughness of the fracture surface and some plasticity-induced closure may produce an increment in the contact of the crack faces during tensile fatigue [61]. As a consequence, a continual breaking and reforming of the oxide happens, leading ultimately to the creation of excess corrosion deposits between the crack faces. These corrosion products have a thickness comparable with the size of the crack tip opening displacements and yield premature contact between the crack faces.

Roughness-induced crack closure exists when the premature contact between the crack faces can arise from an irregular or rough fracture surface morphology [62]. It occurs in a wide range of ductile materials, usually at near-threshold levels at low load ratios, R ($R = K_{min}/K_{max}$). The size-scale of the fracture surface roughness is comparable with the crack tip opening displacements and significant sliding mode displacements exist. In this case the fatigue crack can close prematurely for being wedged open at discrete contact points along the crack faces.

Viscous fluid-induced crack closure (see Figure 2.2.d) occurs when the insertion of a viscous fluid within the growing fatigue crack influences the propagation rate of the cracked component [63]. Although the mechanism is not perfectly understood yet, most of the authors believe that the hydraulic pressure generated by the complete penetration of the crack by the fluid causes a reduction of the effective stress amplitude experienced at the crack tip, which decelerates the fatigue crack growth

rate. As the internal fluid pressure is directly proportional to its viscosity, the decelerating effect is enhanced with higher viscosities of the fluid. Nevertheless, the crack closure promoted by viscous fluids seems not to be as significant as that arising from the plastic deformations in the wake, the roughness or the oxidation of the fracture surfaces.

The fact that phase transformations at the tip of a fatigue crack result in a deceleration of the crack growth rate is known as phase transformation-induced crack closure [64]. A phase transformation at the crack tip (see Figure 2.2.e) can lead to a positive local volume change in the plastic zone. This volume increment will induce compressive stress in the transformed zone, as the transformed volume is surrounded by a large volume of elastic untransformed material. This form of closure is strongly influenced by the size and geometry of the test specimen and of the fatigue crack.

Typically all crack closure mechanisms are augmented by the application of low stress intensity ranges, ΔK, and low minimum to maximum load ratios, because of the smaller crack opening displacement of the fatigue cycle. In fact, by raising the load ratios the closure effects can be reduced or even eliminated.

The main implication of closure mechanisms in fatigue behaviour is a reduction in the crack driving force for the crack advance and hence an increase in fatigue life.

2.2.2 Methods for experimental evaluation of crack closure

Since the first observations in the early seventies of partial closure of the crack during the unloading part of a cycle, even when tensile loading was still present [57], several methods have been developed to experimentally evaluate the crack closure effect. The methods for measuring crack closure can be divided in three main groups: (1) methods based on direct observation of the crack closure at the crack tip; (2) methods based on the measurement of the compliance in order to identify a virtual change of the crack length during crack closure; and (3) indirect methods based on fatigue crack growth [65].

Direct observations of the crack closure can be made with optical microscopy, scanning electron microscopy, replica technique, photography and interferometry.

The most widely used techniques are those that measure the specimen compliance either at locations remote from the crack tip (global methods) or locations adjacent to the crack tip (local methods). In any case they all aim to automatically quantify the crack growth. These methods include clip gauges, strain gauges, potential drop techniques, eddy current, ultrasonics.

Indirect indications derived from crack growth observations comprise methods based on the observation of the striation spacing of fatigue fractures and crack growth rate observations during variable amplitude loading.

Researchers have used these methods individually or combinations of them for evaluating the crack closure effect. Such a case is the work of Jones et al. [66] who obtained displacement-load profiles in three distinct regions of a CT specimen with three independent techniques. The displacement-load behaviour was determined at discrete distances ahead of the crack tip using optical interferometry. Using an interferometric displacement gauge, they also measured the crack opening displacement at various distances behind the crack tip, as a function of load. In addition, they determined the displacements at the notch mouth with a displacement gauge. They found that the results were dependent on the location of the measurement. Evans and Spence [67] also explored the possibility of measuring closure with three different monitoring techniques. In this case they employed potential drop, strain gauges and the replica monitoring techniques for characterizing the closure at several stresses and over a range of crack lengths. They observed good correlation between the three techniques. Bowman et al. [68] used back face strain gauges, front face clip gauges and a laser extensometer for measuring closure loads, and found that a single back face strain gauge was not enough for obtaining accurate closure measurements and that laser extensometry provided the most reliable results. They also showed that the measurement location was an important factor affecting the results. Adding to the uncertainty over measuring techniques, Vecchio et al. [69] found that closure is also dependent on the geometry of the specimen being tested. Later, by using a scanning electron microscope in conjunction with stereoimaging techniques, Davidson [70] showed that the magnitudes of closure loads were reliant on the specimen geometry, while the stress intensity factor (ΔK) was not.

In the last ten years some researchers started to apply other alternative techniques, such as photoelasticity, thermoelasticity or image correlation, for the quantification of crack closure. One of the first works employing these alternative techniques was conducted by Sutton et al. in 1999 [71]. They were able to estimate crack closure loads with image correlation, by determining the crack tip opening displacement at a distance behind the crack tip, imaging a 0.5 by 0.5 mm region. Díaz et al. [43] were able to evaluate phenomena like the presence of residual stresses or crack closure, giving a direct measurement of the effective stress intensity factor of growing fatigue cracks, by means of thermoelastic stress analysis. The method for quantifying the effective stress intensity range represented an improvement over other more traditional techniques, such as the compliance-based techniques. The effective stress intensity factors are derived directly from stress data from ahead of the crack tip, thus including all influences which are a consequence of the crack wake or from the crack tip plastic zone. Moreover the method allows the extraction of crack wake contact force information, which cannot be obtained with compliance measurements, and avoids problems derived from the subjective interpretation existing in compliance methods. Furthermore, the effective stress intensity factor can be directly used for life prediction. Pacey et al. [29] developed a mathematical model based on the stress potential function approach of Muskhelishvili to describe the stresses near the tip of the crack undergoing fracture surface contact. They fitted the model to stress data from photoelasticity in order to determine the effective stress intensity factor during two load cycles, obtaining results that clearly showed evidence of crack closure. The work presented in this thesis follows the same approach as [29] and [43], and evaluates the SIF taking into account full-field information to estimate effective values of the crack driving force. However, the experimental data is provided by image correlation instead of photo or thermoelasticity.

Despite the considerable research that has been conducted on evaluating closure effects with different techniques, there are still unresolved issues related to the measurement of the closure and its mechanisms.

One such example is the controversy about the point which best characterizes the closure. Due to the hysteresis during a fatigue cycle, the deviation from linearity occurs at different points during loading (σ_{op}) and unloading (σ_{cl}) (see Figure 2.4),

with σ_{cl} being often some 15% lower than σ_{op}[72]. There is not full agreement about which of these values should be taken as the lower limit of the stress intensity range. In addition, some authors suggest that crack growth rates are only dependent on the stress ratio [73-74] and that the crack closure can exist, but its contributions to crack growth is either small or negligible [75]. They also proposed a model according to which two load parameters must be exceeded simultaneously if crack growth is to occur, namely ΔK_{th} and K_{max}. The authors supported the new hypothesis with experimental data obtained with drop potential techniques and strain gauges in Titanium alloy centre-cracked and compact tension specimens.

Other research debates the standard closure assessments, and suggests that the lower limit of the effective stress intensity range lies below P_{cl} [76, 69, 77], and hence significant fatigue damage would occur both above and below the crack closing load. All this controversy was reviewed in 1996 and the following reasons were identified as potential sources of ambiguity [78]:

- Discrepancy generated by the use of different experimental techniques. These include differences between compliance methods and other systems, measurements obtained from the surface and through the thickness measurements and positioning of the technique.
- In the case of compliance-based techniques, interpretation given to the variation in the compliance for the characterization of the closure.
- Sensitivity of the closure behaviour to materials, geometry, environment and test methodology.
- Disagreement on the importance and magnitude of plasticity-induced crack closure.

Some efforts have been made to match bulk evaluations with near crack tip results by various schemes of extrapolating the bulk measurement data [79]. Jones et al. [66] observed that bulk measurements, located remotely from the crack tip, often yield a higher opening load than do gauges positioned close to the crack tip. This fact has been usually explained as the different behaviours of the material under plane stress conditions, in the case of near crack tip gauges, and under plane strain conditions, in the case of far from crack tip measurements. The main two advantages of the bulk measurements are that one does not have to replace the system as the crack grows,

and that they avoid the collection of data too close to the crack tip, which might lead to misleading results due to the crack tip plasticity [80]. On the other hand, it has been stated [81] that more accurate measurements can be made positioning the gauge closer to the crack tip in view of the larger change in compliance.

In addition, some researchers also showed that the resolution of the technique and the position in the crack wake, where a major contribution to crack closure occurs, are critical factors in obtaining accurate results rather than approximate estimations [82-83]. Gan and Weertman [80] and later Pippan [84] deepened knowledge in that subject, and studied the sensitivity of the near crack tip strain gauges to different locations and orientations.

Moreover according to the theoretical analysis based on dislocation theory, developed by Louat et al. [85] the measurement should be performed on the loading line of the specimen [81].

The extraction of the point of transition, which characterizes the closure, from compliance traces, is also a critical issue, as it is not easy to identify with certainty in such plots. Some authors consider the transition point as the lowest point at which the plot becomes linear (point E in Figure 2.4).

Others draw two tangents for the upper part and the low part of the load-crack opening displacement (P-COD) curve respectively, as shown in Figure 2.5.a. The point of intersection of the two tangents gives the load at opening, and it is a kind of median stress between the crack fully open and the crack fully closed.

Other investigators follow the variation of the slope approach, according to which the upper part of the P-COD curve is obtained by regression analysis [85]. Subsequently, going down the curve, the local averaged slopes are obtained for each point by considering a number of neighbouring points on both sides of the data point, and the criterion for identifying the opening load is a difference of 5% with the slope of the upper part in the curve.

A fourth method for determining the closure load is to represent the upper section of the P-COD curve (fragment 1 in Figure 2.5.b) by a linear function and the lower part (fragment 2 in Figure 2.5.b) by a second order polynomial. The coefficients for both approximations are determined by a regression analysis. A requirement is that the coordinates and the slopes of the linear part and the second order part should be

equal for both parts at the tangency point. The tangency point is chosen as the point with minimum error in the regression.

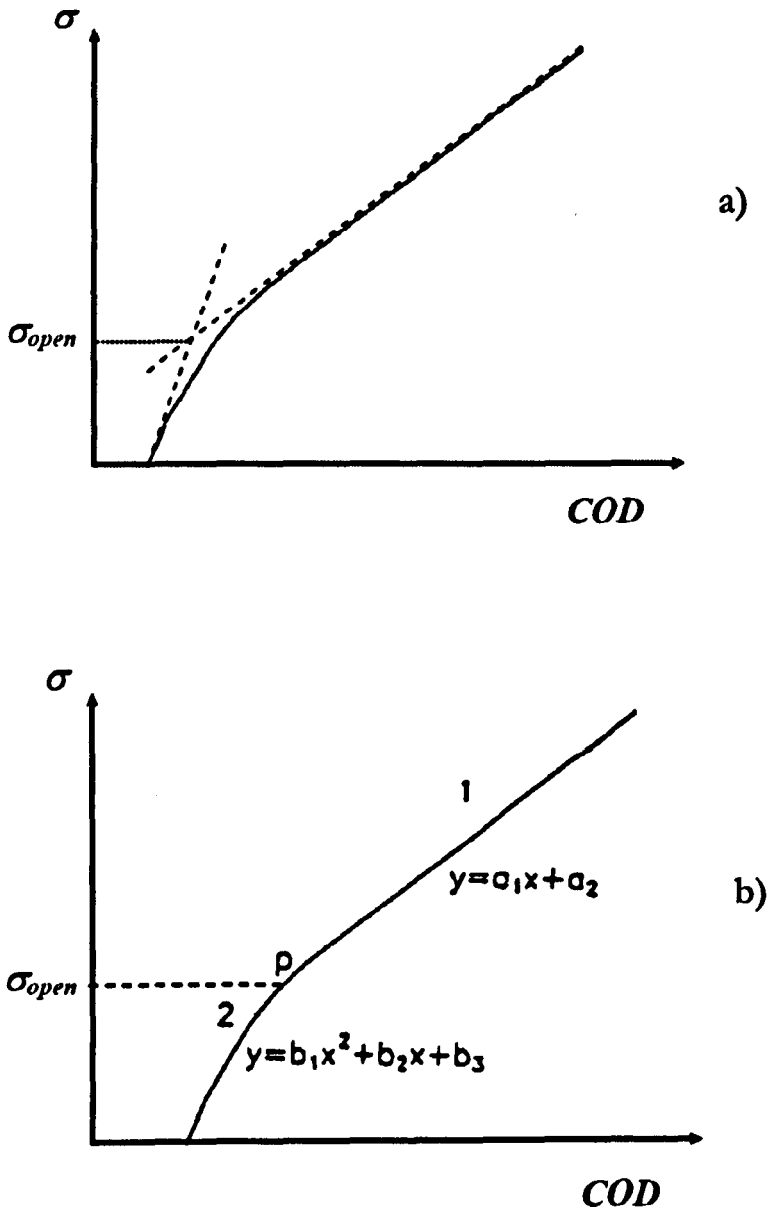

Figure 2.5: Illustration of two methods for crack opening stresses, a) method of the intersection of two tangent lines and b) tangent point method. (After Yisheng and Schijve 1995).

2.2.3 Conclusions

Since Elber first proposed the concept of crack closure, numerous investigations have been devoted to this phenomenon, showing the existence of additional mechanisms for crack closure apart from the initially introduced plasticity-induced crack closure, such as roughness-induced, oxide-induced, viscous fluid-induced or phase transformation-induced crack closure. Extensive work has been carried out for the experimental evaluation of the closure, apart from the initially employed crack opening displacement gauges. New techniques have emerged, and different results have been obtained by using them separately or by combining many of these techniques, providing different accuracies and sensibilities. However, many unknowns still surround the crack closure phenomenon, and the results obtained by different researchers with the different techniques are not always in agreement. The advantages derived from the direct extraction of the effective stress intensity factor range seem to be recognised, although few authors have taken advantage of this fact [29, 43].

By evaluating the stress intensity factor with image correlation, important benefits would be added to the quantifications of closure effect, such as rapidity for performing the measurements and ability to study the phenomenon with a non-contacting technique. These features are the main requirements needed to extend closure phenomena analyses to an industrial environment, allowing the design engineer to take advantage of the possible beneficial effects of the crack closure. In addition, by estimating the effective value of the SIF from full-field displacement information, problems derived from the indirect measurement of crack closure by compliance techniques can be by-passed. Therefore a tool for evaluating the effective stress intensity factor with image correlation appears to be very valuable, not only for comparison purposes, but also for simplifying the procedure for assessing experimentally the crack closure effect.

2.3 Image correlation technique

2.3.1 Principles

Several methods can provide full-field information about displacements. Within this group, the most common are interferometric techniques, such as Moiré interferometry or electronic speckle pattern interferometry (ESPI). These techniques can determine, based on the interferometry phenomenon, the displacements of a surface with high resolution. However, all these interferometric techniques have strict requirements for system stability and very specific requisites: Moiré interferometry needs a grating to be bonded to the surface, which must be flat; and ESPI requires a coherent light source.

The image correlation equipment consists of a CCD camera and a computer. Depending on the quality of the camera and the surface of the object, some illumination system may be required. A typical set up for image correlation is shown in Figure 2.6.

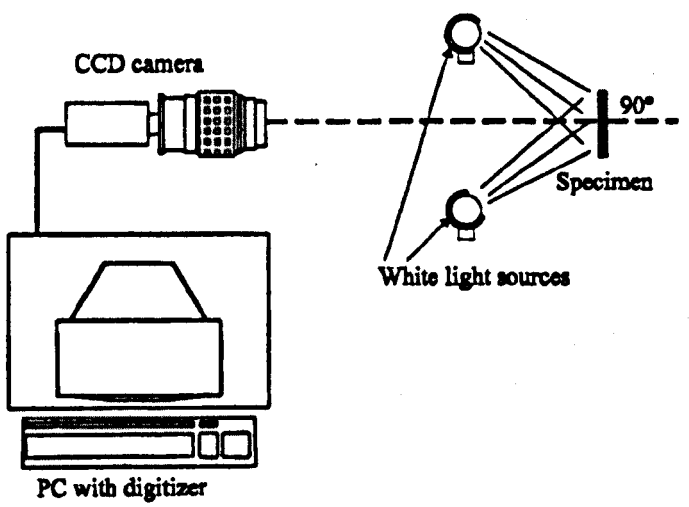

Figure 2.6: Schematic of experimental configuration for image correlation analysis. (After Sutton et al. 2000).

Image correlation is based on computational operations. The technique compares two images acquired at different states, one before and the other after deformation, and tries to match them. This matching is based on the fact that if the intensities of

one image correlate with those of a subsequent image of the same object, it is likely that both images are from the same region. If the object undergoes only translation, the relative offset between the images is the one that makes maximum the correlation function. Unfortunately in most of the cases the deformation experienced by the object is more complex than simple translation, and the relative displacement between the two images is a function of the position. By dividing the images into smaller subimages (also called subsets or interrogation windows) and correlating them, a map of the offsets across the surface can be obtained. For each subimage, there will be a vector joining the centre of this subimage, from the initial state, and the point with highest correlation, in the final state. The resulting map will contain the information of the variation of the displacement with the position, that is, a displacement field of the entire image. The principle of image correlation is summarized in Figure 2.7.

In order to monitor a process with intermediate states in between the initial and the final state, the first image is compared not only with the last image, but also with each image acquired during the whole process. In some cases, depending on the resolution and the level of deformation, it may not be possible to correlate two images acquired at very different states. In these cases, each image is only compared with the image collected immediately before.

The size of the subsets must be sufficiently large to contain enough features so that the subset is unique in the whole image. On the other hand, in order to have a higher resolution in the obtained displacement map, the size of the interrogation windows should be as small as possible (so that the initial image can be divided in more subsets). Therefore, a trade off must be achieved in this sense, so that the subimages are small enough for the required displacement resolution, but large enough to contain enough features.

The features for the matching process are achieved by having a surface pattern that generates varying intensities of diffusely reflected light. When the surface is completely featureless, the characteristic contrast can be achieved by applying only a powder or paint speckle to the surface of the object [52], or by first coating the surface with white paint and then over-spraying it with black paint [89]. In some

cases, at high magnification levels, the microstructure of the material provides natural local contrast, and no surface preparation is required [99].

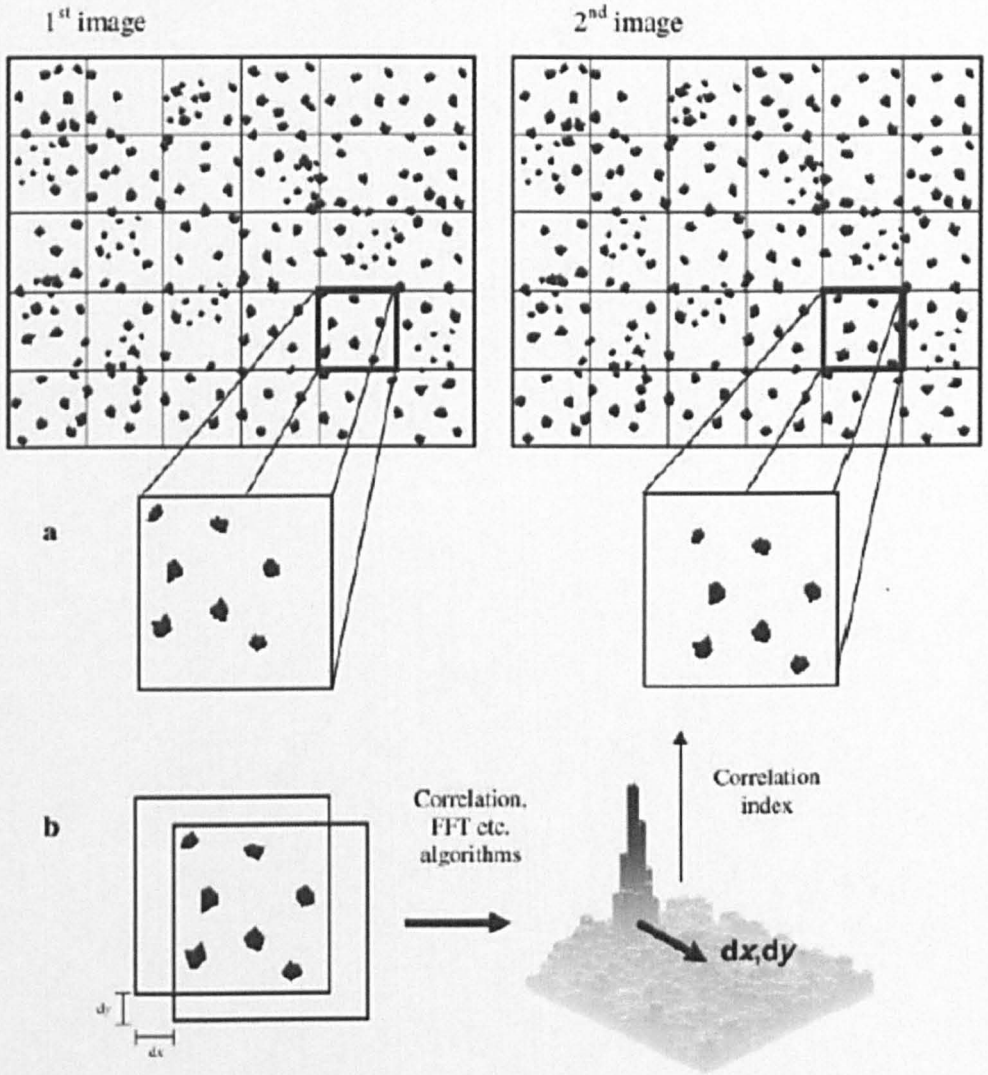

Figure 2.7: Principles of image correlation. (a) In order to obtain a displacement map, the two images acquired before and after deformation, are divided into smaller subimages. (b) Pairs of subimages are then compared computationally, by means of a correlation algorithm. Each displacement vector goes from the centre of the initial state subimage, to the point with highest correlation. (After Quinta da Fonseca et al. 2005).

There are several algorithms to perform the subset comparison. In the course of this work cross-correlation was used, where the displacements are determined by numerically cross-correlating a selected subset from the digitized intensity pattern of the underformed image with the deformed one. A digital image is a two-dimensional

array of intensity values, $I(x, y)$. Given two images, I_1 and I_2, a N × N pixel region of interest is defined for each image. If the image brightness is approximately constant, $\sum I_1^2 \approx \sum I_2^2$, then a measure of the similarity between the two regions of interest can be expressed as a cross-correlation [100]:

$$c(u,v) = \sum_{x=-n}^{n} \sum_{y=-n}^{n} I_1(x, y) I_2(x+u, y+v) \tag{2.1}$$

where u and v are the distances between the centres of the two regions of interest along x and y respectively, and n = N/2.

If I_1 is an image of an object and I_2 is another image of the same object after it undergone some deformation or rigid body movement, then the maximum of the cross-correlation function (2.1) gives the most probable displacement values for the centre of the region of interest in I_1.

In order to speed up the process, in some algorithms the images are first transformed into frequency domain using fast Fourier transform (FFT). Then the cross-correlation function (2.1) is calculated and finally the inverse FFT is computed [101].

2.3.2 History

Image correlation was first used in the early 1980's [86]. The work described how laser speckle patterns of a solid, subjected to two-dimensional loading, could be correlated with an image correlation algorithm, to determine the average displacements and displacement gradients for an object. Over the next years, the concepts proposed in that early work have been modified, for use in optical illumination [87-89] and the emerging technique was applied successfully for measurements of in-plane displacement fields [51, 52, 90, 91]. In [88-89] a new approach for determining surface deformations was presented, based on Newton-Raphson methods for optimization. The new method speeded up the process dramatically, with respect to previous approaches. The depth of colour of the camera was found to affect critically the accuracy of the surface deformations obtained. The depth of colour (also called dynamic range of the camera) is the number of quantization levels in the digitization process used to convert the light intensity into a digital value.

As the image correlation algorithms were refined, researchers began using image correlation methods to address a wide variety of problems, ranging from the measurement of velocity fields in flows [92] to the analysis of strain fields in retinal tissue, under monotonic and cyclic loading [93]. Most significantly the technique was used extensively in fracture mechanics studies, including characterization of displacement fields in the vicinity of stationary and growing cracks [90, 91, 94] and measurements of crack tip opening displacements [95-98]. By using the natural local contrast variation provided by the microstructure, image correlation has also been extended to the study of deformations from optical microscopy images [99].

The different improvements in correlation algorithms in the last decade led to image correlation techniques maturing into a fast, stable and reliable full-field displacement and strain measurement tool.

Chapter 3

Methodology for calculating the stress intensity factor from displacement fields

3.1 Introduction

In the present chapter a mathematical tool based on Muskhelishvili's complex variable methods is developed. It aims to develop the expressions relating the stress intensity factors, K_I and K_{II}, with the in-plane displacement fields. No previous attempt was found to link SIFs with displacement data following Muskhelishvili's formulation.

3.2 Fundamental equations

Let us represent any point (x,y) of a body by the complex variable $z = x + iy$ in the physical plane or z-plane. In the two-dimensional theory of elasticity for homogeneous isotropic bodies, the stresses and displacements can be expressed in terms of two analytical functions $\varphi(z)$ and $\psi(z)$ as [12]

$$\sigma_{xx} + i\sigma_{xy} = \varphi'(z) + \overline{\varphi'(z)} - z\overline{\varphi''(z)} - \overline{\psi'(z)} \tag{3.1}$$

$$\sigma_{yy} - i\sigma_{xy} = \varphi'(z) + \overline{\varphi'(z)} + z\overline{\varphi''(z)} + \overline{\psi'(z)} \tag{3.2}$$

$$2\mu(u + iv) = \chi\varphi(z) - z\overline{\varphi'(z)} - \overline{\psi(z)} \tag{3.3}$$

where

$$\mu = \frac{E}{2(1+\upsilon)}; \quad \chi = 3 - 4\upsilon \text{ (plane strain)}; \quad \chi = \frac{3-\upsilon}{1+\upsilon} \text{ (plane stress)}; \tag{3.4}$$

σ_{ij} are stresses and u, v are displacements, referred all to the rectangular coordinates x, y respectively.

The near-field boundary condition at any point t on the contour L may be expressed as [12]

$$\varphi(t) + t\overline{\varphi'(t)} + \overline{\psi(t)} = i\int_s (\sigma_{xn} + i\sigma_{yn})ds \tag{3.5}$$

where s is the arc on L, and σ_{xn} and σ_{yn} are the stress components parallel and perpendicular respectively, to the tangent of the arc s at point t. Considering the contour L representing a crack, it will be a traction-free contour ($\sigma_{xn} = \sigma_{yn} = 0$), and the boundary condition can simply be written as

$$\varphi(t) + t\overline{\varphi'(t)} + \overline{\psi(t)} = 0 \tag{3.6}$$

3.3 Conformal mapping

A very useful technique for describing an awkwardly shaped boundary condition is to transform the region into one of simpler shape [102]. This transformation can be made with a conformal mapping or conformal transformation. The transformation:

$$z = \omega(\zeta) \tag{3.7}$$

maps from a physical z-plane into a 'mapping' ζ-plane. The function $\omega(\zeta)$ is called the conformal function.

The variables involved in the conformal mapping are summarized in Figure 3.1.

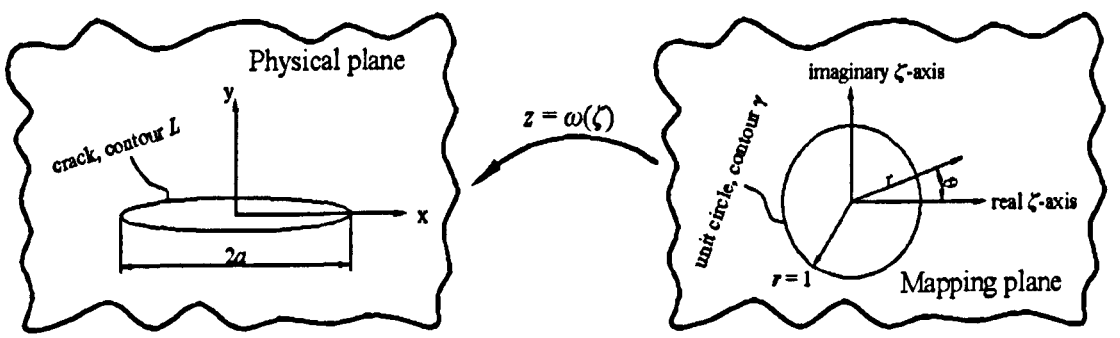

Figure 3.1: Systems of coordinates in the physical and mapping planes.

After substituting equation (3.7) into equations (3.1)-(3.3), the stresses and displacements, in the mapping plane become:

$$\sigma_{xx}+i\sigma_{xy}=\frac{\varphi'(\zeta)}{\omega'(\zeta)}+\frac{\overline{\varphi'(\zeta)}}{\overline{\omega'(\zeta)}}-\omega(\zeta)\frac{\overline{\varphi''(\zeta)\omega'(\zeta)}-\overline{\varphi'(\zeta)\omega''(\zeta)}}{\left[\overline{\omega'(\zeta)}\right]^3}-\frac{\overline{\psi'(\zeta)}}{\overline{\omega'(\zeta)}} \tag{3.8}$$

$$\sigma_{yy}+i\sigma_{xy}=\frac{\varphi'(\zeta)}{\omega'(\zeta)}+\frac{\overline{\varphi'(\zeta)}}{\overline{\omega'(\zeta)}}+\omega(\zeta)\frac{\overline{\varphi''(\zeta)\omega'(\zeta)}-\overline{\varphi'(\zeta)\omega''(\zeta)}}{\left[\overline{\omega'(\zeta)}\right]^3}+\frac{\overline{\psi'(\zeta)}}{\overline{\omega'(\zeta)}} \tag{3.9}$$

$$2\mu(u+iv)=\chi\varphi(\zeta)-\frac{\omega(\zeta)}{\overline{\omega'(\zeta)}}\overline{\varphi'(\zeta)}-\overline{\psi(\zeta)} \tag{3.10}$$

The omitted steps are given in Appendix A.

The conformal function ω is chosen so that a contour L in the physical plane maps onto a unit circle γ in the mapping plane. For ease of calculation it is convenient to use the polar coordinates (r, θ) in the mapping plane, as shown in Fig. 3.1:

$$\zeta=re^{i\theta} \tag{3.11}$$

Any point on γ will be denoted

$$\eta=e^{i\theta} \tag{3.12}$$

so that $\eta=\zeta|_{r=1}$.

The boundary condition in the mapping plane can be obtained substituting (3.7), (A.2) and (3.12) into (3.6):

$$\varphi(\eta)+\frac{\omega(\eta)}{\overline{\omega'(\eta)}}\overline{\varphi'(\eta)}+\overline{\psi(\eta)}=0 \tag{3.13}$$

3.4 Fourier series representation

The analytical functions can be represented as infinite Fourier series

$$\varphi(\zeta)=\sum_{k=-\infty}^{+\infty}a_k\zeta^k;\quad \varphi'(\zeta)=\sum_{k=-\infty}^{+\infty}ka_k\zeta^{k-1};\quad \varphi''(\zeta)=\sum_{k=-\infty}^{+\infty}k(k-1)a_k\zeta^{k-2}; \tag{3.14}$$

$$\psi(\zeta)=\sum_{k=-\infty}^{+\infty}b_k\zeta^k;\quad \psi'(\zeta)=\sum_{k=-\infty}^{+\infty}kb_k\zeta^{k-1}; \tag{3.15}$$

The term $\omega(\eta)/\overline{\omega'(\eta)}$ may also be expanded in Fourier series

$$\frac{\omega(\eta)}{\overline{\omega'(\eta)}}=\sum_{l=-\infty}^{+\infty}c_l\eta^l \tag{3.16}$$

where a_k, b_k and c_l are complex coefficients.

Let us introduce the variable

$$\Omega(\eta) = \frac{\omega(\eta)}{\omega'(\eta)} \tag{3.17}$$

By expanding all the terms in the boundary condition (3.13) and the displacements equation (3.10), splitting the complex variables into real and imaginary parts and truncating the limits of the Fourier expansions, the displacements equation can be rewritten as the following system of equations:

$$\sum_{k=-N}^{N} C_k^j \alpha_k + \sum_{k=-N}^{N} D_k^j \beta_k = 2\mu u^j \tag{3.18}$$

$$\sum_{k=-N}^{N} E_k^j \alpha_k + \sum_{k=-N}^{N} F_k^j \beta_k = 2\mu v^j \tag{3.19}$$

where $j = 1, 2, \ldots p$, u^j and v^j are the displacements at point j, and C_k^j, D_k^j, E_k^j and F_k^j are coefficients dependent of one point j, which are defined in Appendix B. α_k and β_k are the unknowns, also defined in Appendix B. In addition, Appendix B includes the full derivation to obtain (3.18)-(3.19). Note that expressions (3.18)-(3.19) are extended to p displacement data points, rather than one single point, as it was shown in the initial expressions.

The system can be written in matrix form as follows

$$Ax = b \tag{3.20}$$

where $A_{2(2N+1)\times 2p}$ is the matrix of coefficients C_k^j, D_k^j, E_k^j and F_k^j; $x_{2(2N+1)\times 1}$ is the vector of unknowns; and $b_{2p\times 1}$ is the vector of displacements:

$$A = \begin{pmatrix} C_{-N}^1 & \cdots & C_N^1 & D_{-N}^1 & \cdots & D_N^1 \\ C_{-N}^2 & \cdots & C_N^2 & D_{-N}^2 & \cdots & D_N^2 \\ \cdots & \cdots & \cdots & \cdots & \cdots & \cdots \\ C_{-N}^p & \cdots & C_N^p & D_{-N}^p & \cdots & D_N^p \\ & & & & & \\ E_{-N}^1 & \cdots & E_N^1 & F_{-N}^1 & \cdots & F_N^1 \\ E_{-N}^2 & \cdots & E_N^2 & F_{-N}^2 & \cdots & F_N^2 \\ \cdots & \cdots & \cdots & \cdots & \cdots & \cdots \\ E_{-N}^p & \cdots & E_N^p & F_{-N}^p & \cdots & F_N^p \end{pmatrix}, \quad x = \begin{pmatrix} \alpha_{-N} \\ \cdots \\ \alpha_N \\ \beta_{-N} \\ \cdots \\ \beta_N \end{pmatrix}, \quad b = 2\mu \begin{pmatrix} u^1 \\ \cdots \\ u^p \\ v^1 \\ \cdots \\ v^p \end{pmatrix} \tag{3.21}$$

If $p = 2N + 1$ then the number of unknowns equals the number of equations and the system will have a unique solution provided $\det A \neq 0$. The solution can be found by LU decomposition for example. If $p < 2N + 1$ then the number of unknowns is greater than the number of equations and the system is underdetermined and will have infinite number of solutions. If $p > 2N + 1$ then the number of unknowns is smaller than the number of equations and the system is overdetermined. The solution can be found in the linear least squares sense, e.g. by QR decomposition [103].

3.5 Mapping function for the elliptic hole

In order to map a unit circle, $\zeta = e^{i\theta}$, onto an elliptical contour L in the physical plane, utilization will be made of the mapping function

$$z = \omega(\zeta) = R\left(\zeta + \frac{m}{\zeta}\right) \tag{3.22}$$

where R is a scale parameter and m is a shape parameter, $0 \leq m \leq 1$. When m = 0 the ellipse L is a circle of radius R and when $m = 1$ then L is a straight slit or crack of zero thickness and length 4R. Intermediate values of m map onto an ellipse, with semi-axes

$$g = R(1+m); \qquad h = R(1-m) \tag{3.23}$$

The meaning of the conformal mapping and the coordinates used are schematized in Figure 3.1.

By truncating the series expansions of (3.16) and using the notation from (3.17), one obtains

$$\Omega(\eta) = \sum_{l=-M}^{+M} c_l \eta^l \tag{3.24}$$

where

$$c_l = \begin{cases} m & l = -1 \\ (m^2+1)m^{\frac{l-1}{2}} & l = 2n+1 \quad n = 0,\ 1,\ 2,\ \ldots \\ 0 & \text{all other } l \end{cases} \tag{3.25}$$

Appendix C shows how c_l coefficients are obtained, for the above conformal function (3.22).

The series (3.24) is convergent to (3.16) as $M \rightarrow +\infty$. The rate of convergence will be strongly affected by the value of m. The convergence will slow down as $m \rightarrow 1$. For $m = 1$ the series will diverge, see (C.4). Nevertheless the contour L in the physical plane will resemble decreasingly a crack as $m \rightarrow 0$. Hence m must be taken large enough so that L still resembles a crack, but small enough to achieve a satisfactory convergence.

The similarity between the original expression of $\Omega(\eta)$, (3.16), and the series expression (3.24) can be measured by the 2-norm (squared root of the sum of the squares of the elements of a vector) of the differences between the two expressions, q, that is

$$q = \sqrt{\sum_{i=1}^{i=Q}\left(\frac{\omega(\eta_i)}{\omega'(\eta_i)} - \sum_{l=-M}^{+M} c_l \eta_i^l\right)^2} \tag{3.26}$$

Equations (B.13)-(B.16) defining the coefficients C_k^j, D_k^j, E_k^j and F_k^j of expression (3.18)-(3.19) can now be simplified by taking (3.25) into account. It follows from (3.25) that

$$\operatorname{Im} c_l \equiv 0 \tag{3.27}$$

and

$$c_{l+k-1} = 0 \qquad \forall l + k - 1 < -1 \tag{3.28}$$

that is

$$c_{l+k-1} = 0 \qquad \forall l < -k \tag{3.29}$$

Therefore the summations in (B.13)-(B.16) should start at $l = -k$:

$$C_k = \chi \operatorname{Re}\zeta^k - k \operatorname{Re}\Omega \operatorname{Re}\zeta^{k-1} - k \operatorname{Im}\Omega \operatorname{Im}\zeta^{k-1} + \operatorname{Re}\zeta^{-k} + \\ + k \sum_{l=-k}^{M} c_{l+k-1} \operatorname{Re}\zeta^{-l} \tag{3.30}$$

$$D_k = -\chi \operatorname{Im}\zeta^k + k \operatorname{Re}\Omega \operatorname{Im}\zeta^{k-1} - k \operatorname{Im}\Omega \operatorname{Re}\zeta^{-k} + \operatorname{Im}\zeta^{-k} - \\ - k \sum_{l=-k}^{M} c_{l+k-1} \operatorname{Im}\zeta^{-l} \tag{3.31}$$

$$E_k = \chi \operatorname{Im}\zeta^k + k \operatorname{Re}\Omega \operatorname{Im}\zeta^{k-1} - k \operatorname{Im}\Omega \operatorname{Re}\zeta^{-k} - \operatorname{Im}\zeta^{-k} - \\ - k \sum_{l=-k}^{M} c_{l+k-1} \operatorname{Im}\zeta^{-l} \tag{3.32}$$

$$F_k = \chi \operatorname{Re}\zeta^k + k \operatorname{Re}\Omega \operatorname{Re}\zeta^{k-1} + k \operatorname{Im}\Omega \operatorname{Im}\zeta^{k-1} + \operatorname{Re}\zeta^{-k} - \\ - k\sum_{l=-k}^{M} c_{l+k-1} \operatorname{Re}\zeta^{-l} \tag{3.33}$$

3.6 Stability of the system of equations

The stability of the system of equations (3.20) will be explored with the help of the singular value decomposition (SVD).

A real $m \times n$ matrix A, which has at least as many rows as columns ($m \geq n$), can be written as the following product of matrices [104]:

$$A = U\Sigma V^T \tag{3.34}$$

where U is an $m \times m$ orthogonal matrix, V is an $n \times n$ orthogonal matrix, and $\sum$ is and $m \times n$ diagonal matrix with $s_{ij} = 0$ if $i \neq j$ and $s_{ii} = s_i \geq 0$.

A matrix M is said to be orthogonal if $MM^T = I$, the identity matrix. The superscript T is used to denote the transpose of a matrix. Furthermore, it can be shown [104] that there exist matrices U and V such that

$$s_1 \geq s_2 \geq \ldots \geq s_n \geq 0 \tag{3.35}$$

The quantities s_i are called the singular values of A, and the columns of U and V are called the left and right singular vectors, respectively.

The condition number of A is defined as the following ratio

$$cond(A) = \frac{s_{max}}{s_{min}} \tag{3.36}$$

By taking (3.35) into account, the condition number becomes

$$cond(A) = \frac{s_1}{s_n} \tag{3.37}$$

The condition number of a matrix A measures the stability of the system $Ax=b$, by quantifying the independence of the columns of A. The condition number quantifies the sensitivity of the system with respect perturbations in the displacement vector, b.

Note that, by definition, $cond(A) \geq 1$. If $cond(A)$ is close to 1, then the columns of A are very independent and the stability of the system, to errors in the vector b, is as good as it can be. That is, a relative error existing in b is not amplified. If the condition number is too large, the columns of A are nearly dependent, and the

relative error in b can be amplified $cond(A)$ times. Too large a condition number means that its reciprocal approaches the machine's floating point precision (10^{-6} for single precision, and 10^{-12} for double precision) [103]. In that case the matrix A is ill-conditioned, and the noise in the displacement vector b can be vastly magnified. Furthermore, the system will be only solved with some specific numerical methods, which, compared with more traditional methods, are more expensive in terms of computational effort.

It follows from above paragraph that, in order to make our method as stable as possible and as fast as possible, the condition number should be kept as small as possible.

The condition number of A was calculated numerically using equations (3.30)-(3.33) where Ω is defined by (3.17) and (C.5). The shape parameter, m, was take as m = 0.995 to simulate a very elongated, crack-like ellipse. To ensure satisfactory convergence of the series (3.24), the series limit, M, was taken as M = 500. Section 3.8 provides justification of these values.

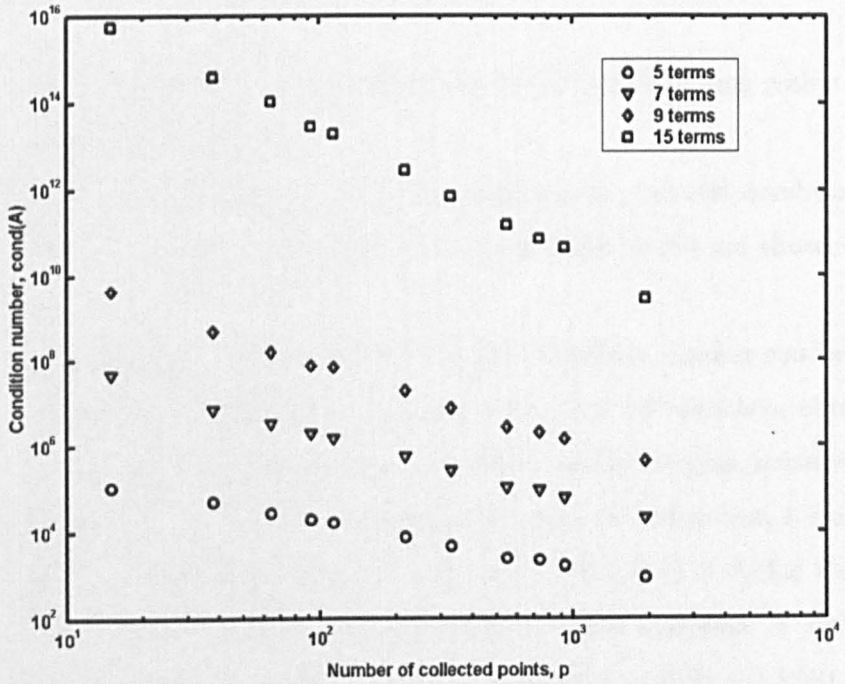

Figure 3.2: Evolution of the condition number of the matrix A from (3.20) versus the number of collected points, p. Note the logarithmic scale in both axes.

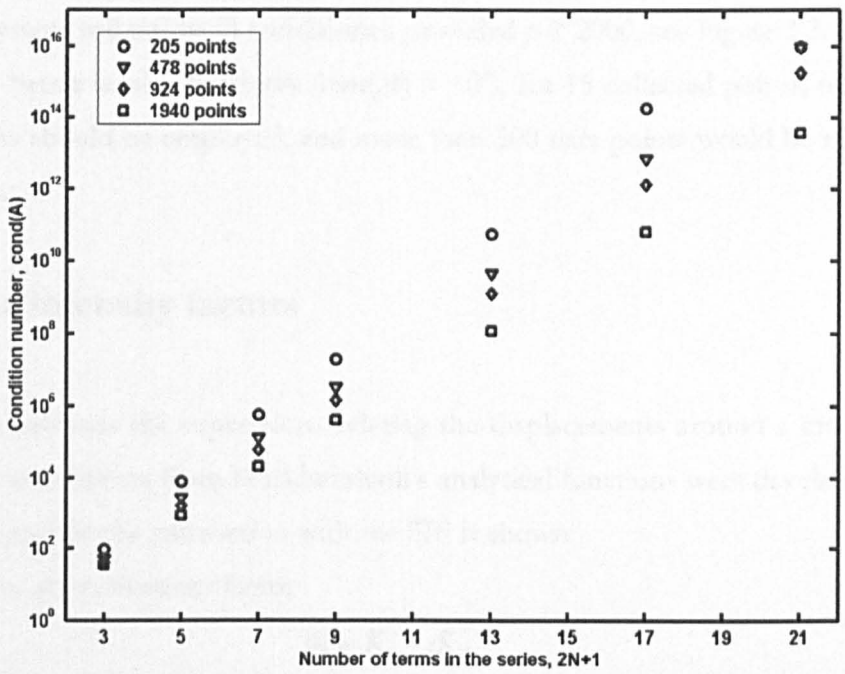

Figure 3.3: Evolution of the condition number of the matrix A from (3.20) versus the number of terms in the series, $2N+1$. Note the logarithmic scale in vertical axis.

The data points for this analysis were located on a grating within a rectangular array centred on the crack tip.

The condition number of A was calculated for several combinations of the series limit, N, and the number of points, p, and the results are shown in Figures 3.2 and 3.3.

It is clear from Figures 3.2-3.3 that the condition number can be reduced by taking more points and/or fewer terms in the series. Nevertheless, comparing Figures 3.2 and 3.3 it can be seen than the condition number is more sensitive to the number of terms, $2N + 1$, than to the number of collected data points, p. For example if $N = 6$ and $p = 205$ then $cond(A) = 10^{11}$. However, if $N = 8$, for the same number of collected data points, the condition number increases 3 orders of magnitude approximately. For achieving the same order of $cond(A)$, $p = 1940$ is needed.

To avoid the matrix A becoming ill-conditioned, $cond(A)$ should be kept smaller than 10^{12}. Even by using as little as 15 data points, matrix A will not be ill-conditioned for

up to 11 terms in the series expansion, see Figure 3.2. On the other hand, if $2N + 1 = 17$, the system will not be ill-conditioned provided $p \geq 2000$, see Figure 3.3.
To achieve better levels of stability ($cond(A) \approx 10^5$), for 15 collected points, no more than 5 terms should be employed, and more than 500 data points would be required for 7 terms.

3.7 Stress intensity factors

In previous sections the expressions relating the displacements around a crack and the Fourier coefficients from Muskhelishvili's analytical functions were developed. In the present section the connection with the SIF is shown.
The complex stress intensity factor

$$K = K_I - iK_{II} \tag{3.38}$$

is related to the analytical functions and the mapping function through [105]

$$K = 2\sqrt{2\pi}\lim_{\zeta\to\infty}\varphi'(\zeta)\frac{\sqrt{\omega(\zeta)-\omega(1)}}{\omega'(\zeta)} \tag{3.39}$$

where the factor $\sqrt{\pi}$ was not yet included in the SIF expression [105].
The limiting value of (3.39) can be found with $m = 1$ in (3.22) and (3.14)

$$K = 2\sqrt{\frac{\pi}{a}}\sum_{k=-N}^{+N} k a_k \tag{3.40}$$

where $z = a$ in the physical plane corresponds to $\zeta = 1$ in the mapping plane.

3.8 Verification

To verify the expressions previously developed, artificial displacement fields were generated. The simulated displacements were based on the analytical expressions for a centre crack in an infinite plane subjected to uniform load applied at infinity, i.e. Westergaard's equations [4]:

$$u = \frac{K_I}{\mu}\sqrt{\frac{r}{2\pi}}\cos\frac{\theta}{2}\left(1-2\delta+\sin^2\frac{\theta}{2}\right)+\frac{K_{II}}{\mu}\sqrt{\frac{r}{2\pi}}\sin\frac{\theta}{2}\left(2-2\delta+\cos^2\frac{\theta}{2}\right) \tag{3.41}$$

$$v = \frac{K_I}{\mu}\sqrt{\frac{r}{2\pi}}\sin\frac{\theta}{2}\left(1-2\delta+\sin^2\frac{\theta}{2}\right)+\frac{K_{II}}{\mu}\sqrt{\frac{r}{2\pi}}\cos\frac{\theta}{2}\left(2\delta-1+\sin^2\frac{\theta}{2}\right) \tag{3.42}$$

where

$$\delta = \begin{cases} \upsilon & \text{for plane strain} \\ \dfrac{\upsilon}{1+\upsilon} & \text{for plane stress} \end{cases} \tag{3.43}$$

The displacement fields were generated for the case of mixed mode $K_I = K_{II} = 50$ MPa$\sqrt{\text{m}}$ in a number of points located on a regular grid within a rectangular array centred on the crack tip. The plane stress case was chosen, as the proposed method is intended for use with a surface measurement technique, as image correlation. Subsequently the system (3.20) was solved, and the SIFs were found using (3.40).

Table 3.1 shows the results for different shape parameters, m, of the mapping function (3.22). It can be observed from Table 3.1 that the SIFs are very sensitive to the shape parameter. For $m \leq 0.7$ the errors are large, particularly for the sliding mode SIF. This is because to solve the limit from expression (3.39) m was assumed to be 1. As m becomes closer to 1 the errors decrease, and for $m \geq 0.99$, the errors are below 0.1 %, which is probably accurate enough for most engineering applications of the technique. Nevertheless even better results can be achieved by making m closer to 1. These small errors are probably due to the accumulation of rounding errors in the sums involving many terms [106], like those in equations (3.30) to (3.33).

The data were simulated in ideal conditions, and hence did not include any random noise in the measured displacements. For that reason it was possible to use a much smaller ratio p/N than in recommendations from section 3.6.

In order to analyze the effect of the limit of the series (3.24) on the final SIF, the case of $m = 0.995$ was chosen, as very accurate results were obtained in Table 3.1 for this value of the shape parameter.

It can be observed from Table 3.2 that the difference between the original expressions of $\Omega(\eta)$, (3.16) and the series expression (3.24), q, decreases as the limit M is increased, as expected. Furthermore, the decrease is more prominent for $M \geq 500$. This indicates that the series representation of (3.16) converges to the analytical

expression (3.16) only when M is sufficiently large. However, for smaller M, e.g. $M \leq 100$, q is large.

m	K_I, MPa$\sqrt{m}$	K_{II}, MPa$\sqrt{m}$	K_I error, %	K_{II} error, %
0.5	52.82	65.24	5.63	30.48
0.7	50.76	56.83	1.53	13.65
0.9	50.07	51.04	0.13	2.08
0.99	50.00	50.04	1.36×10^{-3}	7.99×10^{-3}
0.995	50.00	50.02	4.43×10^{-3}	3.64×10^{-3}
0.999	50.00	50.00	1.53×10^{-3}	6.93×10^{-3}

Table 3.1: Calculated SIFs and the corresponding errors for several values of the shape parameter, m, of the mapping function. The nominal applied $K_I = K_{II} = 50$ MPa$\sqrt{m}$. $p = 338$ displacement data points were used. The series limit in (3.18)-(3.19) was taken $N = 20$. The series limit in (3.24) was $M = 600$.

As $\omega(\eta)/\overline{\omega'(\eta)}$ is related to the near field boundary condition (3.13), a large q means that the boundary condition is not perfectly satisfied. Nevertheless, in the simulated data, the boundary condition is satisfied exactly, as the crack is defined as a traction free surface.

The effect of the error in the boundary condition representation increases as the data points are taken closer to the boundary. In the extreme case, when the data points are taken from the boundary, the error in the SIF will be a maximum because the error in the boundary condition representation will also be a maximum. In other words, if the errors in a_k increase, the errors in K will also increase since equations (3.18)-(3.19) will not hold true, as they are derived from (3.13).

Table 3.2 shows that the errors in the SIF are small even for $M = 100$, where q is large. Moreover, it can be observed from Table 3.2 that there is a threshold ($M = 100$) above which, the limit M does not effect the SIF. This is because the data points were not collected on the boundary.

As a consequence, if the displacement data are collected from locations sufficiently remote from the crack, then a satisfactory solution can be obtained with small series

limit M. On the other hand, if it is necessary to collect the data from the boundary or very close to the boundary, the value of M needs to be increased.

It is also noticed from Table 3.2, that there is an increment in computation cost associated with larger M values.

M	q, *eqn (3.26)*	K_I error, %	K_{II} error, %	time, s
10	1.2×10^{3}	1.78	6.94	2.9
100	7.6×10^{2}	4.43×10^{-4}	3.64×10^{-2}	3.6
500	1.0×10^{2}	4.43×10^{-4}	3.64×10^{-2}	6.7
1000	8.3	4.43×10^{-4}	3.64×10^{-2}	11.0
2000	5.6×10^{-2}	4.43×10^{-4}	3.64×10^{-2}	19.3

Table 3.2: Errors in the calculated SIFs for different values of the series limit in (3.24), M. The 2-norm residual, q, calculated according to (3.26), and the computational time. 338 displacement data points were collected (p = 338). The series limit in (3.18)-(3.19) was chosen N = 20. The shape parameter of the mapping function was m = 0.995.

3.9 Conclusions

In this chapter the theory for calculating the two Muskhelishvili's analytical functions to describe the displacement fields have been developed. The Fourier coefficients of the series representations of the analytical functions can be used to reconstruct the full elastic solution or the SIFs.

The sensitivity of the system to noise in the experimentally collected data has been studied. The stability of the method increases with more data points and fewer terms in the Fourier series. Moreover the stability is more sensitive to the number of terms in the series. Based on the SVD analysis, some thresholds for avoiding the failure of the numerical method are as follows: use no more than 11 terms in the series for 15 experimental data points, and no more than 17 terms for 1000 expererimental data points. If these limits are exceeded, then a small amount of noise in the experimental data can swamp the solution.

In order to assure a good stability, the recommendations are stricter. For 15 displacement points, up to 5 terms in the series should be employed, and more than 500 data points would be required for 7 terms.

The analytical expressions were verified numerically for the case of a centre crack in an infinite panel subjected to uniform load applied at infinity. It has been shown that the combination of $m = 0.995$ and $M = 100$ provides SIF errors better than 0.05%.

Chapter 4

Apparatus and methods

4.1 Specimens employed

The geometries employed in this work can be classified into two groups: pure mode I geometries and mixed mode I + II geometries.

For pure mode I testing, the wedge opening loaded (also known as WOL specimen) sample was employed. The wedge opening loaded geometry is similar to the common CT geometries employed in fracture toughness testing. The difference between both geometries is the ligament, which, in case of the wedge opening loaded specimen is slightly longer, allowing more growth of the crack before complete fracture. The specimens were 10 mm thick, 90 mm wide and 67 mm long. The specimen follows the geometry specified by Murakami [107]. All the details about the specimen's geometry are summarized in Figure 4.1.

As regards the mixed mode I + II geometries, two geometries were employed. The first of them was a centre-cracked plate, which in conjunction with the loading grips proposed by Otsuka et al. [108] allowed seven different mixity of modes, ranging from pure mode I to pure mode II conditions. The sample was a 100 × 120 mm plate that can be loaded in tension so that the loading axis makes an angle θ with the crack plane. The gauge section was 2 mm thick. The grip design allows loading from $\theta = 0°$, pure mode II, to $\theta = 90°$, pure mode I, in 15° increments. The whole configuration of the grips and the centre-cracked panel geometry are illustrated in Figure 4.2.

A cut was machined in the centre of the plate, by means of wire-cut EDM (electrical discharge machining), so that a fatigue crack could be grown in the sample (see

section 4.3 Pre-crack process). A hole was first drilled in the geometrical centre of the plate, with the smallest diameter required to allow the EDM wire to be put through. Then, the EDM wire was moved horizontally (according to Figure 4.2.a) to create a cut of length $2a$. Finally, the resulting thickness of the cut was measured with a feeler gauge, giving a reading of 0.32 mm.

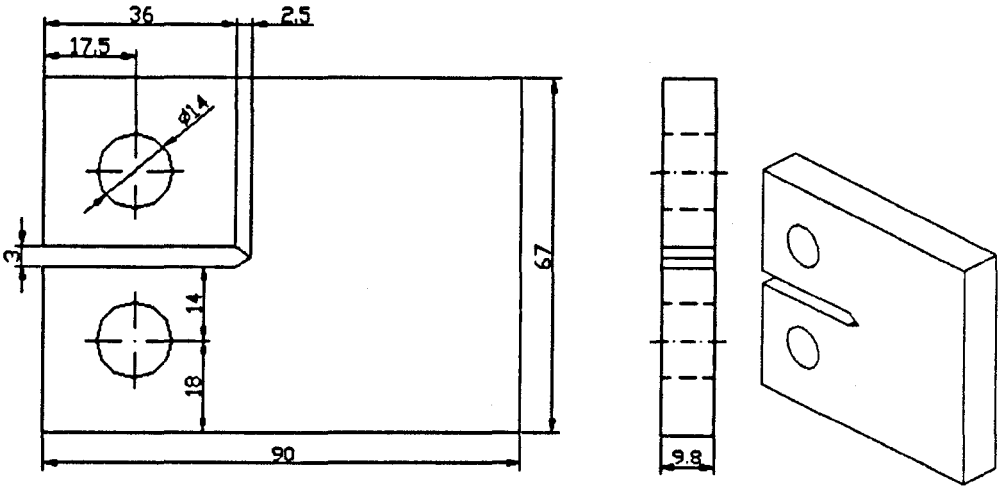

Figure 4.1: Left and centre: Geometry details of the 2024 aluminium alloy WOL specimen, utilized for mode I analysis. Dimensions are in millimetres. Right: Three dimensional view of the specimen.

The second geometry for mixed mode conditions was a plate with a crack emanating from a centred hole. It aimed to investigate the problem of a free-hole in a tensile plate. The sample was 160 mm width, 240 mm length and 5 mm thick. The diameter of the central hole was 50 mm. A schematic illustration of this geometry is shown in Figure 4.3. In addition, the hole-in-a-plate geometry was loaded with the same grips as the centre-cracked panel, to allow different levels of load mixity, as described in Figure 4.4. Due to the differences in dimensions between the hole-in-a-plate specimen and the centre-cracked panel, the grips allowed loading of the hole geometries from $\theta = 23.5°$, to $\theta = 90°$, pure mode I, in 11.1° increments.

The wedge opening loaded specimen was chosen because it had been heavily studied previously, so that there is data readily available for comparison purposes. The centre-cracked panel is a relatively simple geometry, that allows the study of a whole range of mixed mode I + II possibilities. The theoretical solutions for SIF of all these geometries have been presented in a reference edited by Murakami [107].

The hole-in-a-plate sample, although less studied than the other geometries, has more industrial relevance, as it is a type of geometry from which cracks often propagate industrially. In addition, the geometry was tested previously [109] with photoelasticity.

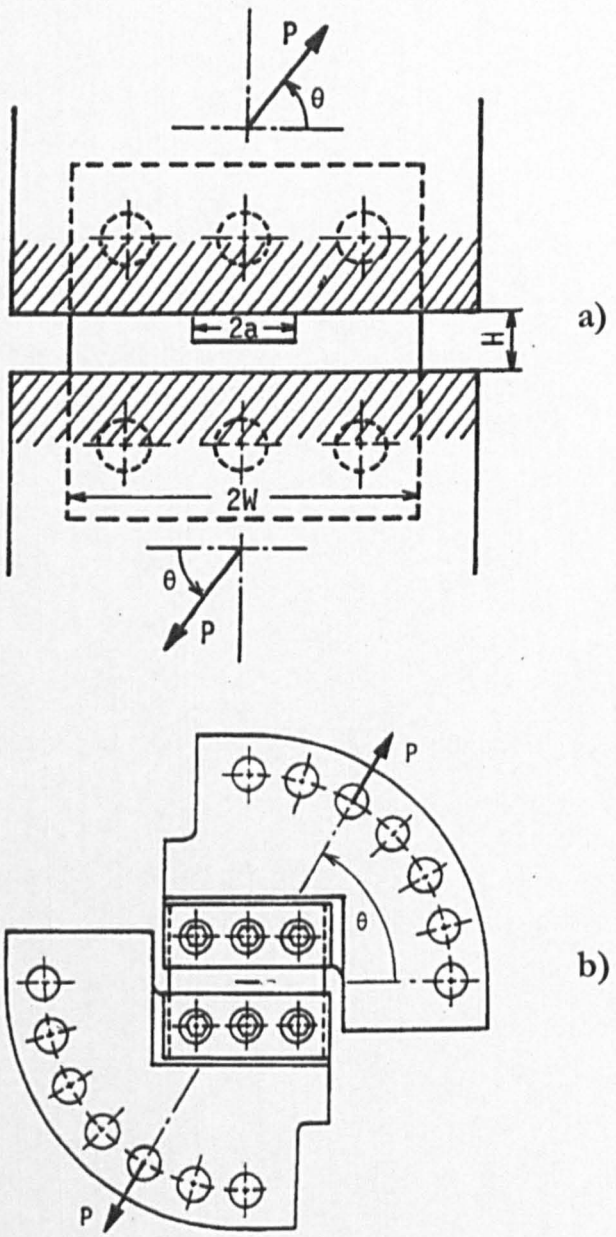

Figure 4.2: Schematic of the centre cracked plate, showing the direction, θ, of the applied load, P. (a) The geometrical details are $2a$ = 40 mm, H = 20 mm, and $2W$ = 120 mm. (b) Centre cracked plate specimen mounted on the special grips allowing seven different mixed-mode loadings. (After Murakami 1987).

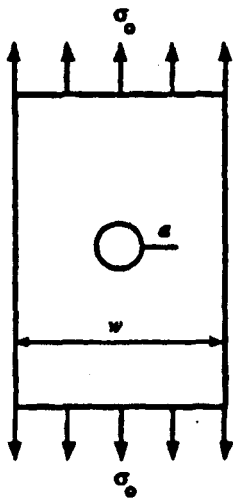

Figure 4.3: Illustration of the geometry for the free-hole in a rectangular plate. The load shown is for pure mode I conditions ($\theta = 90°$). (After Nurse et al. 1994).

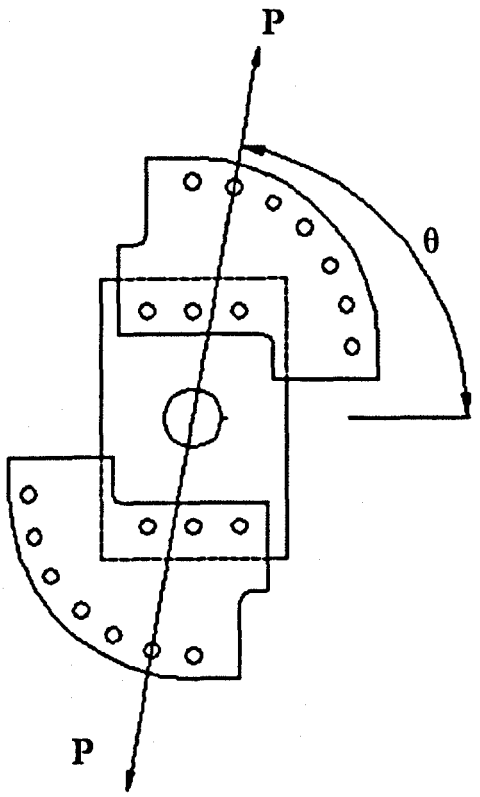

Figure 4.4: Schematic of the resulting configuration of using the grips proposed by Otsuka et al. [108] with the rectangular plate with a crack emanating from a centred hole.

4.2 Material employed

The materials employed during the course of this work were provided by Airbus UK. The wedge opening loaded specimens were made of aluminium alloy 2024 T351. The centre-cracked and hole-in-a-plate specimens were machined from a 10 mm thick 7010 T7651 aluminium alloy plate.

Both alloys are extensively used in the aircraft industry, principally in wing structures. 7010 alloys are predominantly used on spars, ribs and top skins, depending on the aircraft. 2024 aluminium alloy is a bottom skin material.

4.3 Pre-crack process

The use of real fatigue cracks, instead of notches, is essential for studying the problem as it appears in reality. Notches, although much easier to introduce, bear little resemblance to real fatigue cracks, because they have a blunt radius, and over-simplify the study eliminating all effects such as contact or local mixed mode. For this reason all the specimens were fatigue pre-cracked. The pre-cracking was implemented by subjecting the specimens to a number of cycles, under pure mode I conditions. The pre-cracking was conducted by applying ΔK of 10 MPa$\sqrt{m}$ and load ratio of 0.1 at a frequency of 10 Hz. In the case of the hole-in-a-plate geometry, to help the pre-cracking process, a small notch was first introduced, so that the pre-cracking could be done with a reasonable number of cycles (one million cycles). A sharp notch was cut at the position of maximum stress on one side of the hole, using a circular saw blade of 0.15 mm width. The length of the notch was less that 1 mm.

Following the above described procedure, real fatigue cracks were introduced in the specimens. Some examples are shown in Figure 4.5.

To measure the crack length during the pre-crack process, a travelling microscope or Vernier microscope (The Precision Tool & Instrument Co. Ltd. – type 2158) was located in front of the specimens and at a distance from the surface of the specimen of approximately 10 mm. The microscope was equipped with a 1 inch 5X lens (Cooke 21853) and had a resolution of 0.01 mm. Given the close-up working distance of the travelling microscope, a 100 Watt lamp was employed to illuminate

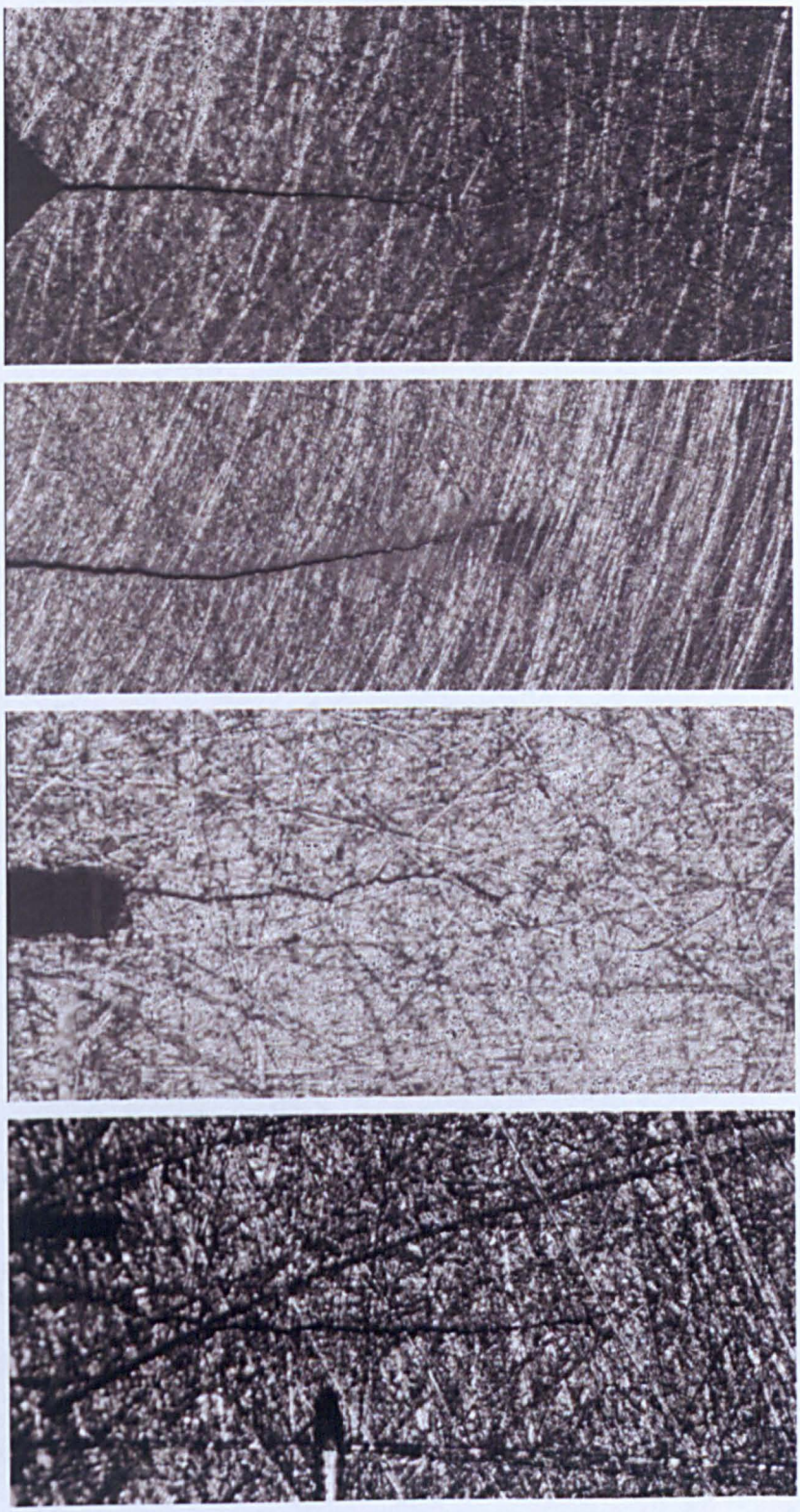

Figure 4.5: Photographs of the fatigue cracks grown in (a) and (b) wedge opening loaded samples, (c) centred crack plate and (d) crack emanating from a hole sample, subjected to tensile load. Note the random patterns of scratches applied to the surfaces.

the sample, as is shown in Figure 4.6. The sample was then subjected to the same load applied for pre-cracking the specimen, but at 0.05 Hz. In that way, while the maximum load is being applied, it is possible to distinguish the crack.

4.4 Equipment for fatigue testing

The equipment used for loading the specimens consisted of a hydraulic system, type MAND 100, with range from 0 to 100 kN calibrated according to BS EN ISO 7500-1:2004. The system is controlled with a visual display unit K7500 Servocontroller, manufactured by Kesley Instruments Ltd.

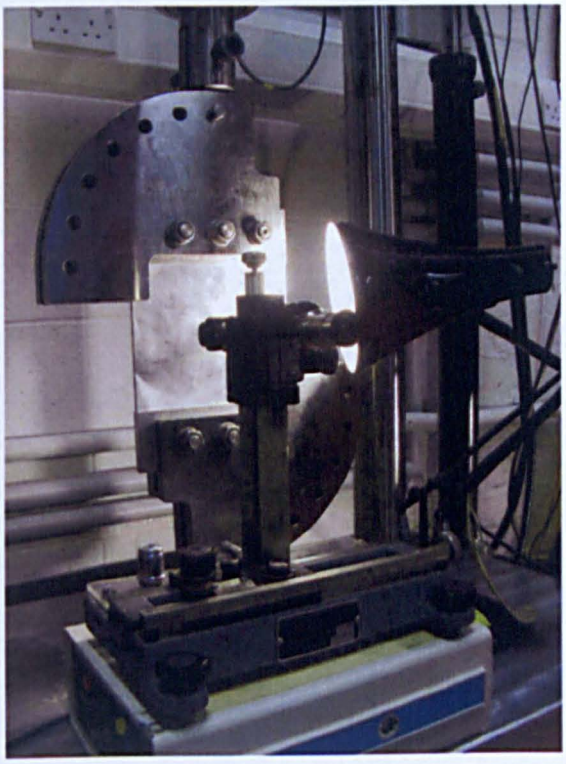

Figure 4.6: Setup employed for measuring the crack length, with travelling microscope and lamp.

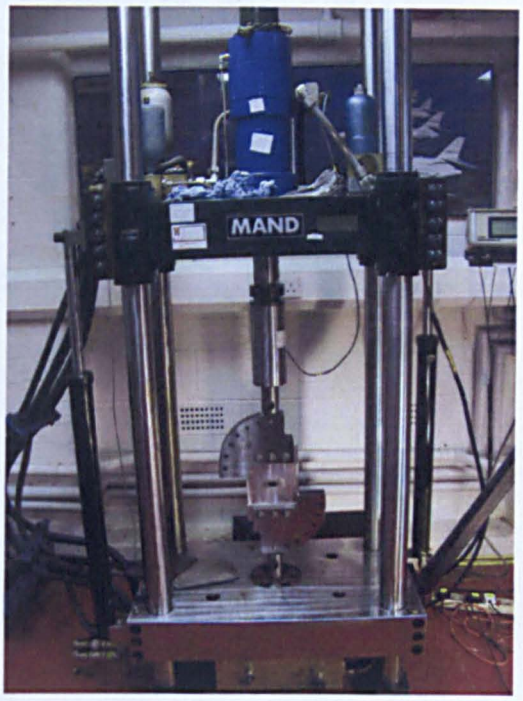

Figure 4.7: Fatigue testing machine employed for applying the load to the specimens. In this picture, a rectangular plate with a centred hole and a crack emanating from the hole is subjected to pure mode I loading, $\theta = 90°$.

The specimens were loaded in the hydraulic machine using the grips previously described in section 4.1. All the tests were conducted under load mode. The load signal provided by the load cell had a voltage range of $\pm$ 10 V, and was captured by an analogical to digital converter. A voltage value was collected at the same time as every camera frame was recorded, so that each single camera frame has associated a voltage value directly related with the load applied by the testing rig. The testing machine is shown in Figure 4.7.

4.5 Image correlation equipment

In this work, the software employed for performing the correlation between successive images was DaVis. The algorithm is based on a hierarchical Fourier method [101]. The displacement vectors can be obtained with or without iterations. If the algorithm does not perform any iteration, the vector calculation is carried out in one single pass. Nevertheless the computation can be done with a number of

iterations (typically from 2 to 5) in the same image. In this case the computed vector field information obtained in one iteration is used as the reference vector field for the next pass. Using the information from the previous pass, the position of the interrogation windows in the new pass is shifted, so that the number of matching features between the undeformed frame and the deformed frames is increased. This improves the signal to noise ratio, providing higher precision results. A schematic of this iterative approach is shown in Figure 4.8.

In addition, the size of the interrogation window can be decreased throughout the different passes, thus producing higher density of displacement vectors. This is done by evaluating in a first pass the initial interrogation window size, and calculating a reference vector field. In the next pass the window size is reduced and the vector calculated in the first pass is used as a best-choice window shift. In this manner the window shift is adaptively improved to compute the vectors in the following steps more reliably. This ensures the same features are correlated with each other, even if a small interrogation window is employed, where less features enter into the window compared with a larger one. This iterative procedure with decreasing window size allows using a smaller final interrogation window size than it would be possible without adaptive window shifting. As a consequence the spatial resolution is improved and less erroneous vectors are produced.

However, the processing time increases approximately as many times as number of iterations is carried out. For this reason, in this work, three iterations were performed, an initial one with a larger interrogation window (128 × 128 pixel), and two subsequent iterations with a smaller size (32 × 32 pixel).

The dynamic range or depth of colour of the camera is the number of quantization levels in the digitization process used to convert the light intensity into a digital value. If the dynamic range is 8 bits then the whole range of intensities will be converted into a number from 1 to 2^8. The number of bits in the camera affects critically the accuracy of the surface deformations obtained by image correlation [88]. Comparing two cameras with different depths of colour, a small difference in light intensities may be detected by the camera with higher depth of colour, and the same intensity difference can appear to be zero in the camera with lower depth. In practical terms, by using a higher dynamic range charge-coupled device (CCD), the effect of noise is

minimized. For images with poor contrast, by increasing the depth of colour, the recorded object can be described better, and consequently, the image correlation algorithm can perform more successfully. Moreover, the sensitivity of the CCD with higher number of bits is increased. A 14 bit CCD camera was employed in the experiments.

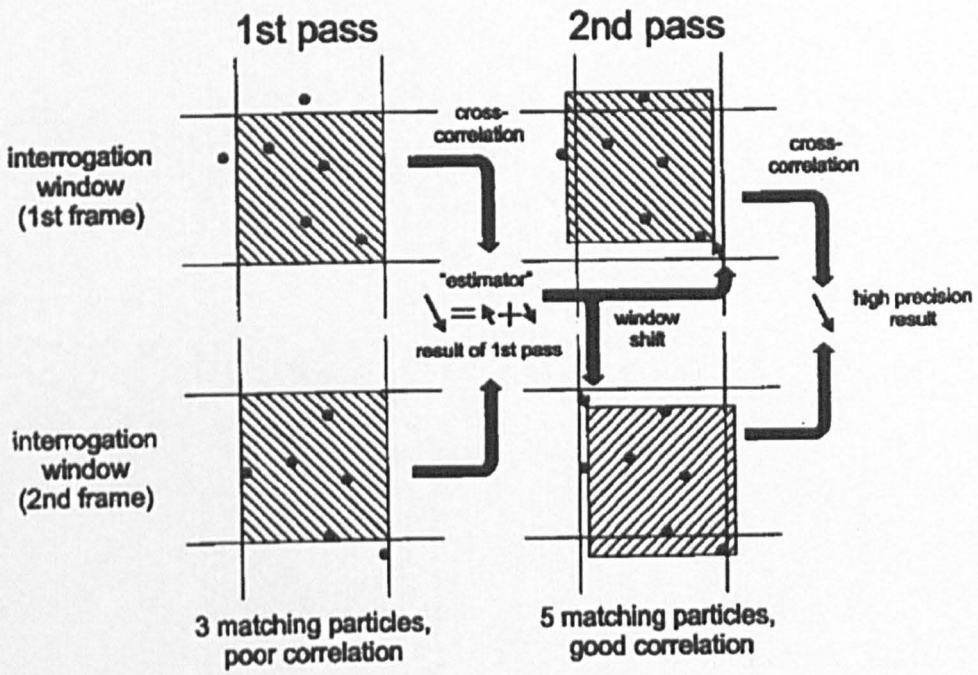

Figure 4.8: Adaptive iterative process with two passes, followed by the image correlation algorithm. (From [101]).

The spacing between displacement vectors depends on the size of the CCD sensor, as, if a 32 × 32 pixel interrogation window is utilized, the spacing between displacement vectors is typically 1/32 of the number of pixels in the CCD. The camera employed has 1600 × 1200 pixel CCD, yielding, for an interrogation window size of 32 × 32, a map of 50 × 37 displacement vectors.

In order to visualize this concept, let us consider the sketch from Fig. 2.7. For the shake of clarity, let us also assume that the CCD employed in Fig. 2.7 is 1500 × 1250 pixel. For an interrogation window size of 250 × 250, the displacement field will be an array of 6 (=1500/250) by 5 (=1250/250) pixel (see Fig. 2.7).

In order to produce denser displacement map, the algorithm allows a degree of overlap of each interrogation window with neighbouring windows. This means that, for an overlap of 50% during the correlation process, half of the interrogation window is part of the next interrogation window in both the horizontal and vertical directions. A schematic of the window overlap concept is shown in Figure 4.9. By using an overlap of 50%, an interrogation window size of 32 × 32 pixel and a CCD of 1600 × 1200 pixels, a resulting map of 100 × 75 displacement vectors was achieved.

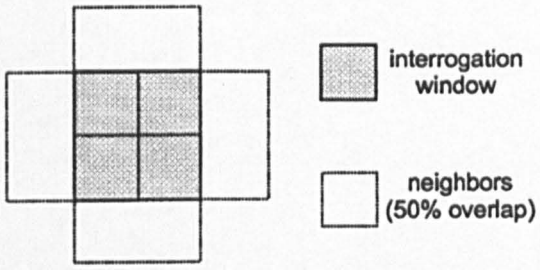

Figure 4.9: Illustration of interrogation window overlap. Example for 50% interrogation window overlap. (From [101]).

The features needed for best performance of the image correlation algorithm were introduced in the form of a network of scratches of varying orientation, width and depth. This was created by scratching the region of the sample surface to be studied with SiC grit paper, grade 120.

No speckle pattern was applied to the surface, which is a traditional image correlation surface preparation method [52 and 89] (see Figure 4.10). By scratching the surface it was possible to achieve a smaller size of feature, allowing the use of a smaller interrogation window, and therefore having a denser map of displacements. Examples of surface finish used for optical correlation purposes are shown in Figure 4.5. It can be appreciated that the image contrast achieved by scratching the surface instead of applying a speckle pattern to the surface is poorer. Nevertheless this fact can be compensated by employing a larger dynamic range. Good results were obtained in the present work by simply scratching the surface and employing a 14 bit digital camera.

Two optical setups were employed, generating two different resolutions. The lower resolution was achieved with a 55 mm *Canon* macro lens attached to the digital camera. The lens was located at approximately 200 mm from the sample and was illuminated by a 100 W lamp.

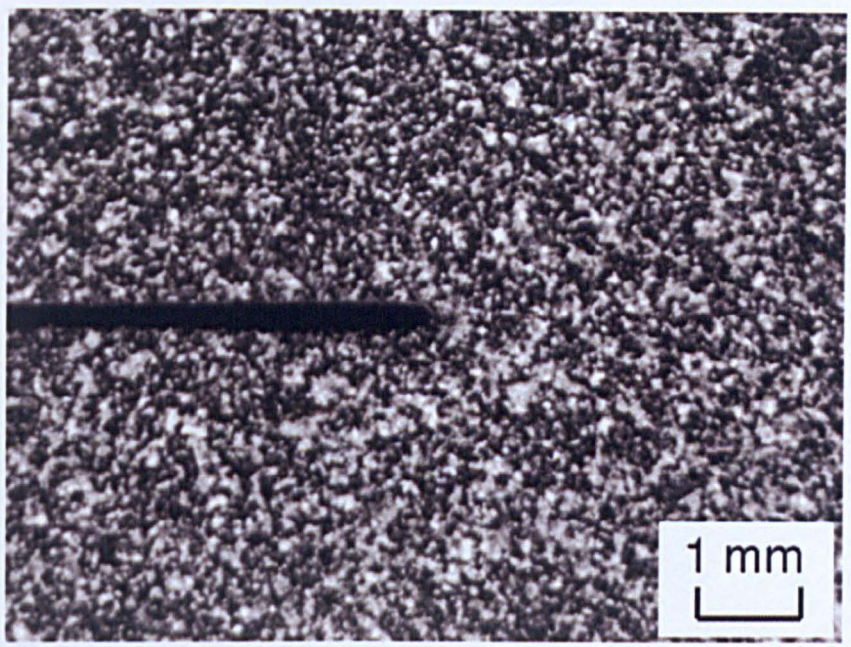

Figure 4.10: Random speckle pattern employed usually in image correlation techniques. (After Yoneyama et al. 2006).

The higher resolution was reached by using a close-up *Precise Eye* lens, manufactured by *Navitar*. The working distance required for this lens was approximately 20 mm. In order to achieve a uniform illumination of the surface of the specimen, a coaxial fibre optic illuminator was employed, attached directly to the lens, as shown in Figure 4.11. This consisted of a halogen light source with a variable light intensity control. In this way the intensity can be adjusted so that no saturations appear in the image.

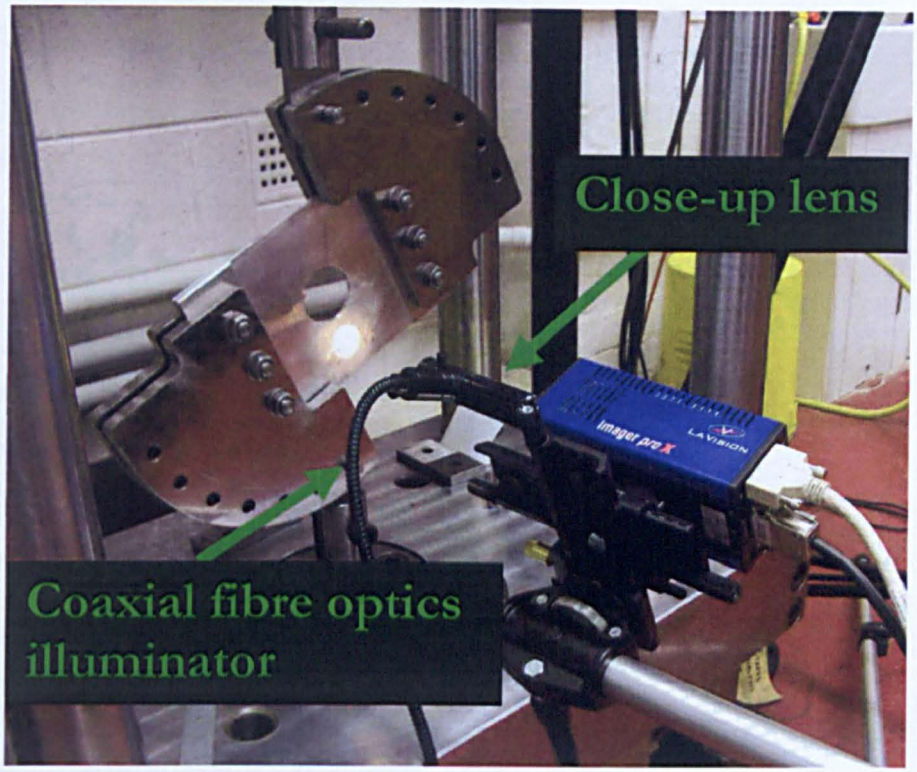

Figure 4.11: Optical setup consisting of a lens with a coaxial fibre optics illuminator. A hole in a plate sample is mounted on the rig, subjected to mixed mode loading conditions. The sample is loaded at an angle θ = 23.5°. In order to be consistent with the system of coordinates defined in Figure 3.1, the camera was rotated the same angle.

4.5.1 Calibration of the equipment

The general procedure for the calibration of the image correlation system comprises the determination of the aspect ratio (displayed width of the sensor in the camera, divided by its height), the measurement of the magnification factor for one direction in pixels/mm, the estimation of the location of the lens center and the evaluation of the distortion coefficient for the lens. If high quality lenses are employed in the acquisition of the images, as is the case of the lenses used in the course of this work, the effects of image distortion can be neglected, and the calibration requires the measurement of the aspect ratio and the magnification factor [110].

The aspect ratio is constant for a specific camera-digitizing board interface. The aspect ratio was 4:3 with the setup employed.

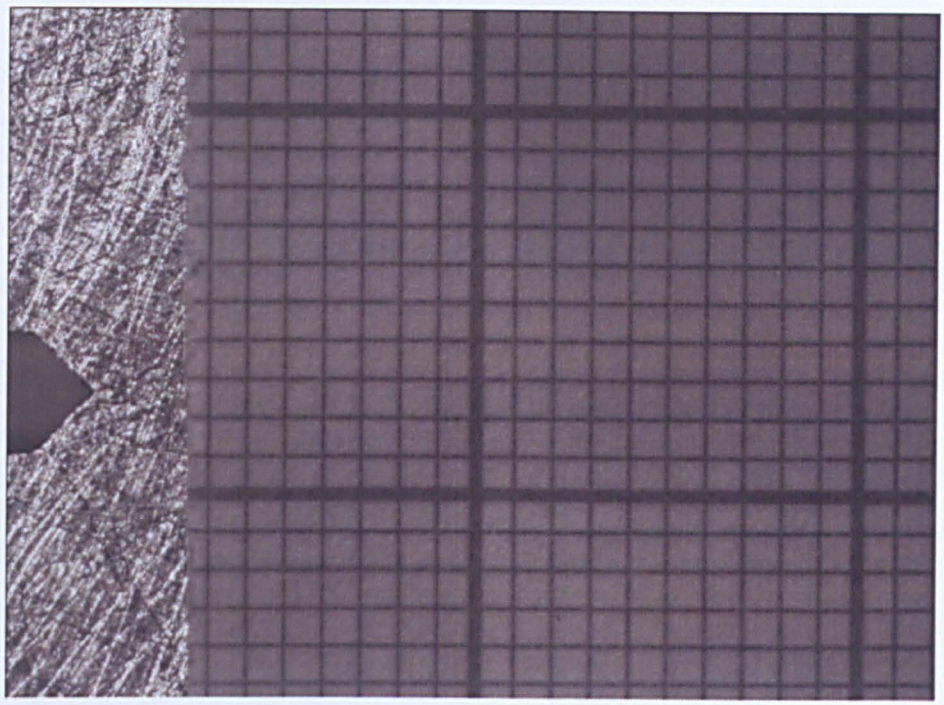

Figure 4.12: Millimetre graph paper attached to a sample for evaluating the magnification factor.

The magnification factor relates the size of the region being imaged to the number of pixels of the sensor. The magnification factor was determined by two methods. Initially, millimetre graph paper was attached to the surface of the object, as shown in Figure 4.12, and its image was captured prior to the testing. Subsequently a distance was selected on the paper, and the number of pixels contained in the distance was counted, so that the pixels per millimeter could be computed. However, this approach presented a minor inconvenience as, unless the milimetric paper was affixed to the object over its entire surface, it becomes not fully attached in some points. Accordingly, in these points, the distance between the camera and the calibration paper and the distance between the camera and the surface of the sample is not exactly the same. To overcome this issue, a second method was devised to evaluate the magnification factor.

The alternative method consisted on engraving some marks (crosses) at known distances in the region surrounding the crack tip. These marks were carved in the surface, with the help of a height gauge equipped with a carbide tipped scriber (see Figure 4.13). By determining in this way the magnification factor, two benefits are

obtained. On the one hand the accuracy of the method is slightly improved, as the marks are engraved on the surface to be analyzed. On the other hand, the need to capture images specifically for the calibration is eliminated, and the images acquired while the test is conducted are valid for the calibration. One example of the engraved marks in the surface of a wedge opening loaded specimen is shown in Figure 4.14.

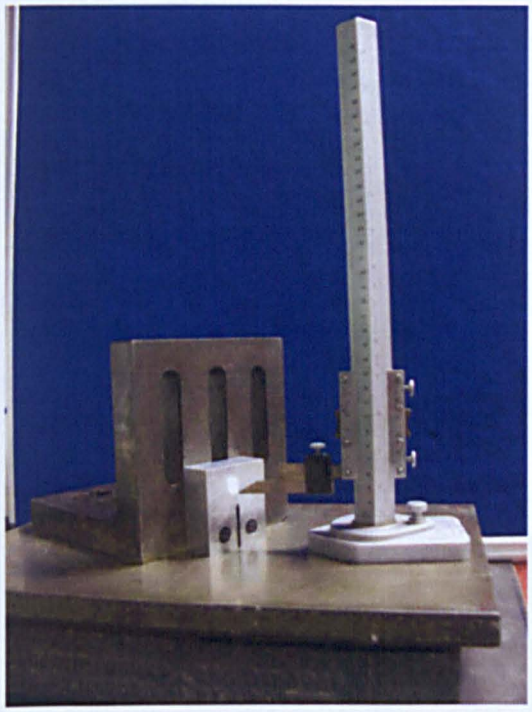

Figure 4.13: Height gauge fitted with a carbide tipper scriber, employed for engraving marks in the surface of the samples for the calibration of the image correlation equipment.

The magnification factor attained with the 55 mm macro lens was around 40 pixels per mm, or 25 μm per pixel. Typical magnification factors for the *Precise Eye* optical setup were in the order of 250 pixels per mm (or 4 μm per pixel).

4.5.2 Presenting the displacement fields

The raw information provided by image correlation consists of maps of displacement vectors, describing the deformations in the vicinity of a crack. If both horizontal, u, and vertical, v, components of the displacement are presented in the same image, then a map of vectors is necessary. Figures 4.15 and 4.16 show different

displacement fields around a crack, acquired at different levels of mixity. The load applied in all the cases (see Figure 4.2) was approximately 15 KN.

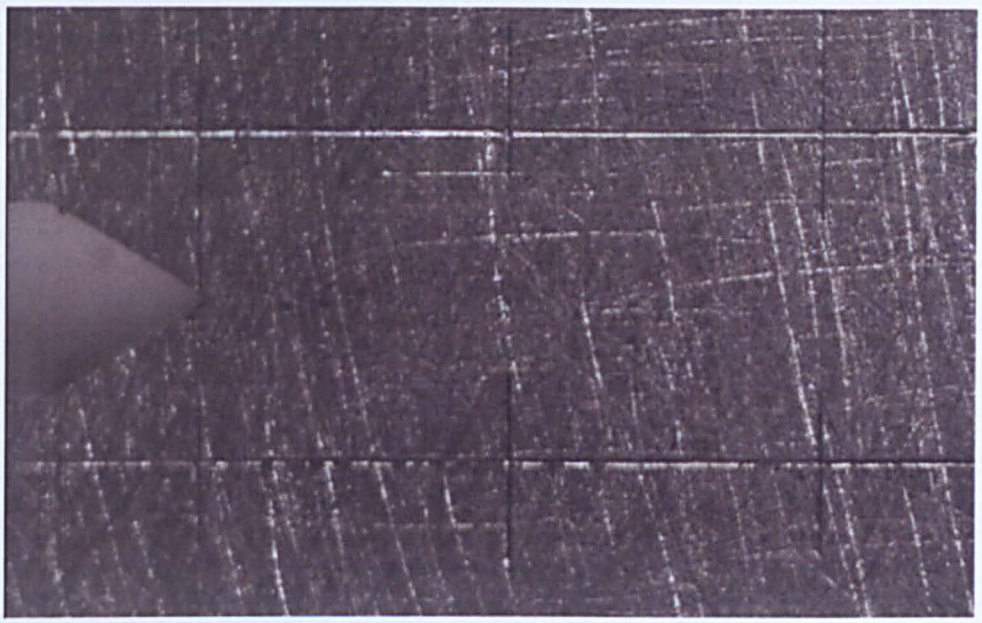

Figure 4.14: Array of cross marks engraved in the surface of the specimen around the crack. The horizontal and vertical distances between two consecutive crosses are 4 mm. These marks were employed for determining the magnification factor of the images.

In addition the vectors can be resolved in their horizontal and vertical components, and the information split in two different images. Examples of such images, again for different cases of mixed mode, are illustrated in Figures 4.17 to 4.20. In both ways of representing the displacement fields around a crack, a discontinuity appears along the crack. It can be also noted that the vertical displacements are approximately one order of magnitude higher than horizontal displacements for pure mode I conditions. On the contrary, for pure mode II conditions, the horizontal displacements are one order of magnitude larger than the vertical displacements, as the main deformation occurs following the sliding mode.

4.6 Conclusions

In the present chapter a justification was given of the specimen geometries and materials employed during the course of this work. The fatigue tests were also presented, including the pre-cracking process and the equipment for fatigue testing. Finally the image correlation equipment utilized in this work was described. This included explanations of the different features of the algorithm, the surface preparation of the specimens, the calibration of the image correlation technique and a presentation of the displacement data obtained from image correlation. The equipment, materials and methods herein described will be used in chapters 5, 6 and 7.

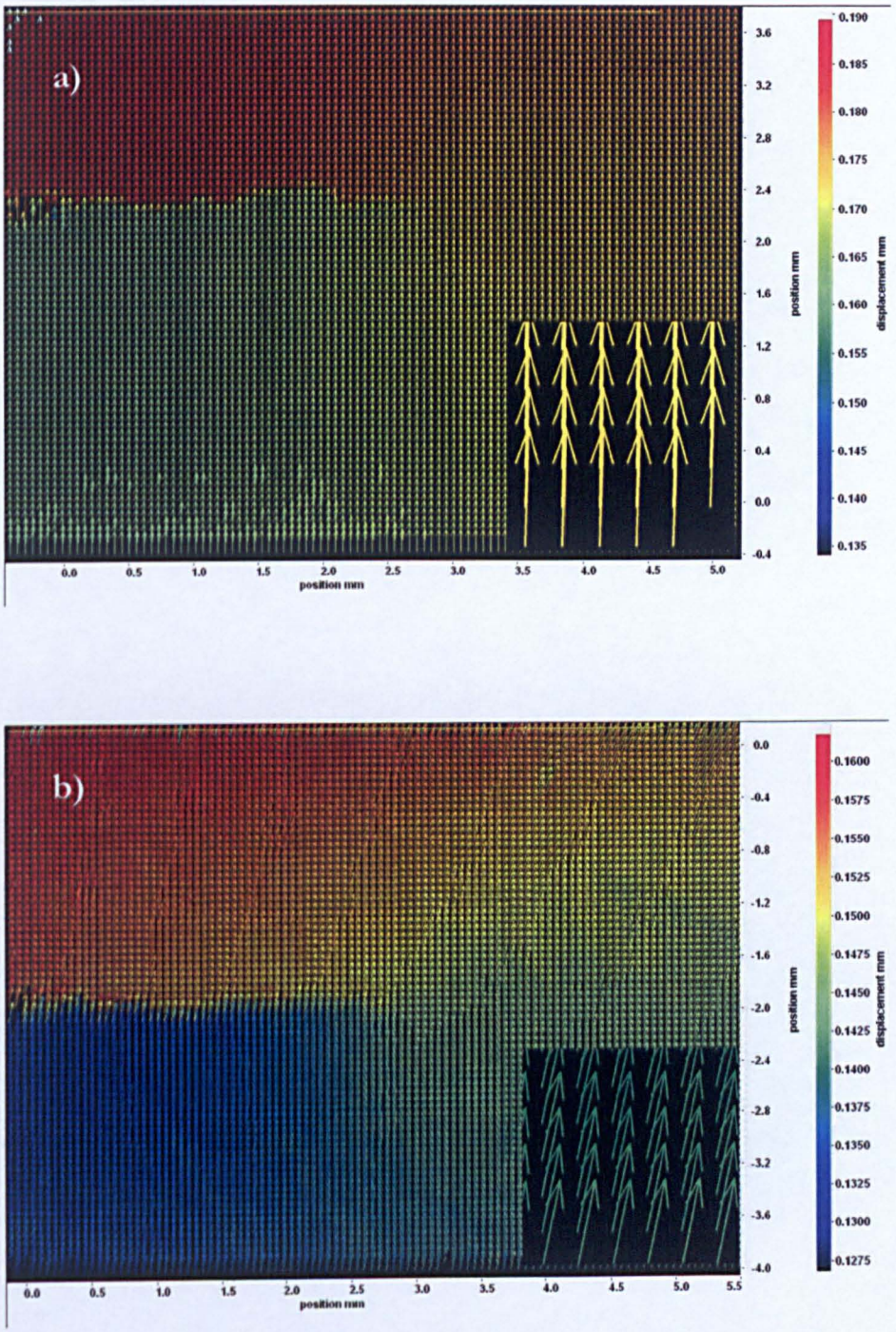

Figure 4.15: Displacement field images where both horizontal and vertical information is contained. The vectors at the bottom right corner are magnified. The crack is positioned to the left of the crack tip. (a) Displacements for pure mode I loading, $\theta = 90°$. The crack tip is approximately at (2.8, 2.2). (b) Displacements for mixed mode loading, $\theta = 60°$. The crack tip is approximately at (2.6, -2.1).

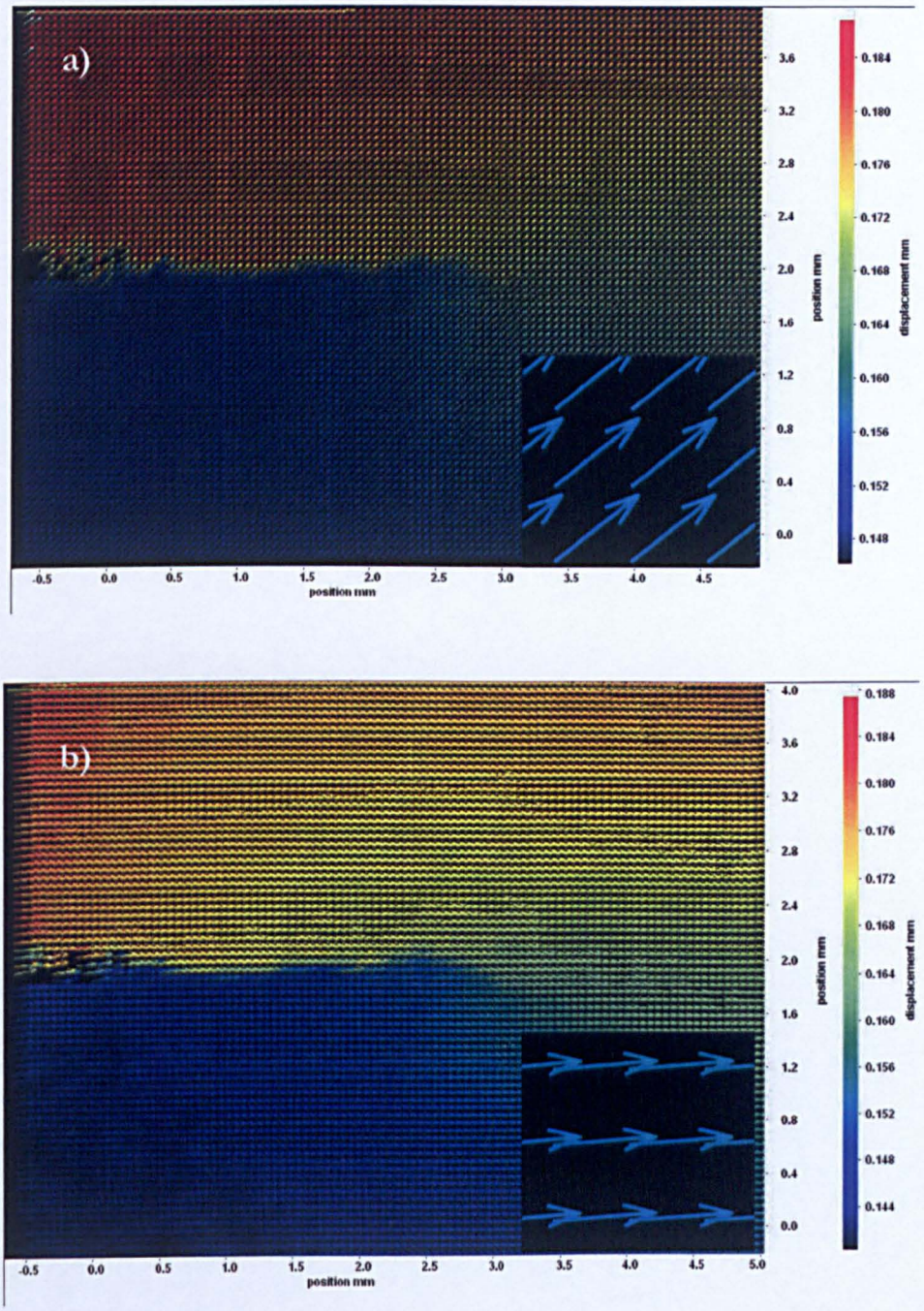

Figure 4.16 Displacement field images where both horizontal and vertical information is contained. The vectors at the bottom right corner are magnified. The crack is approximately at (3.0, 1.9) and the crack is positioned to the left. (a) Displacements for mixed mode loading, $\theta = 30°$. (b) Displacements for pure mode II loading, $\theta = 0°$.

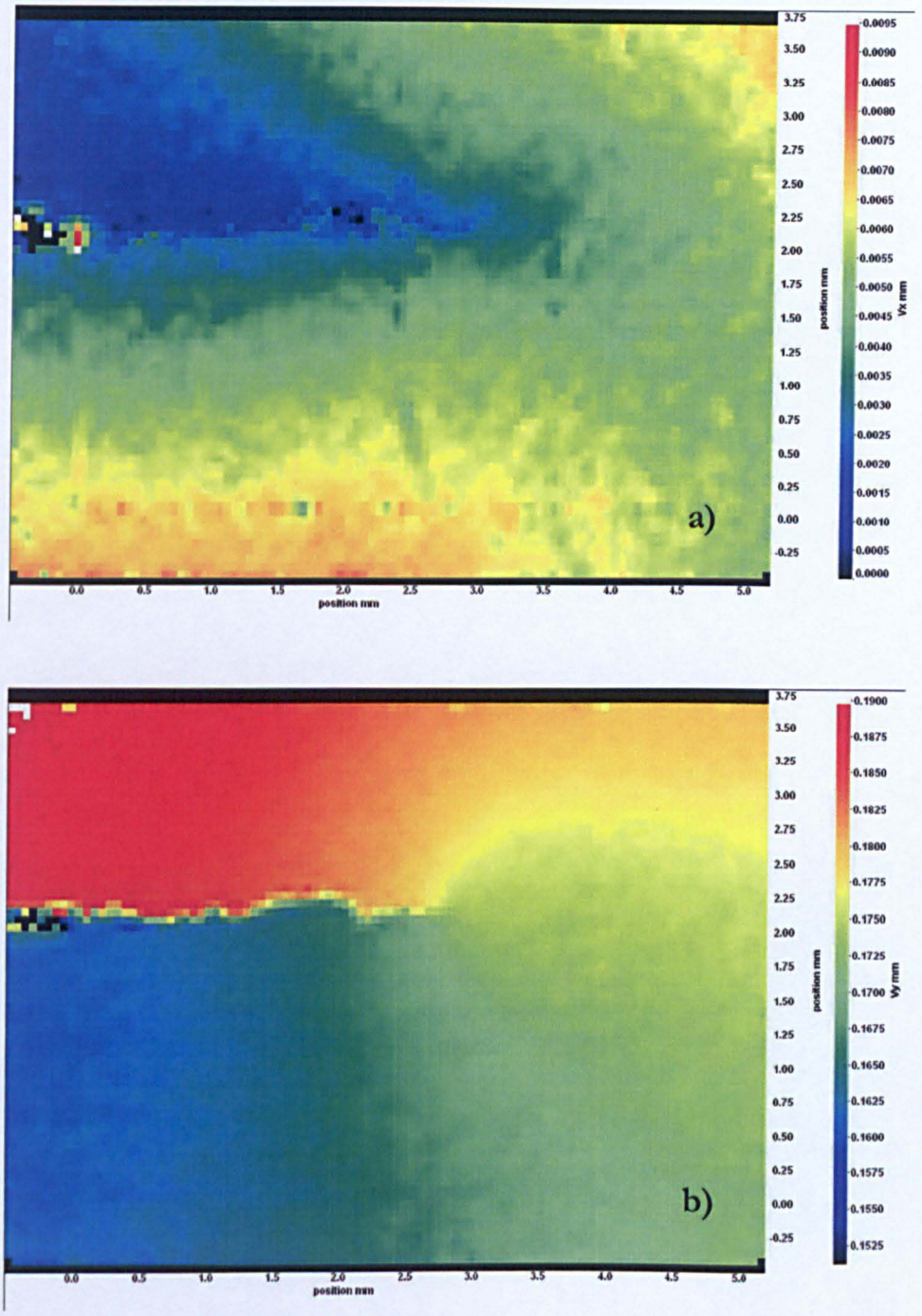

Figure 4.17: Displacement fields with the information split in horizontal and vertical components for pure mode I loading, $\theta = 90°$. The crack tip is approximately at (2.8, 2.2) and the crack is positioned to the left. (a) Horizontal displacements, *u*. (b) Vertical displacements, *v*.

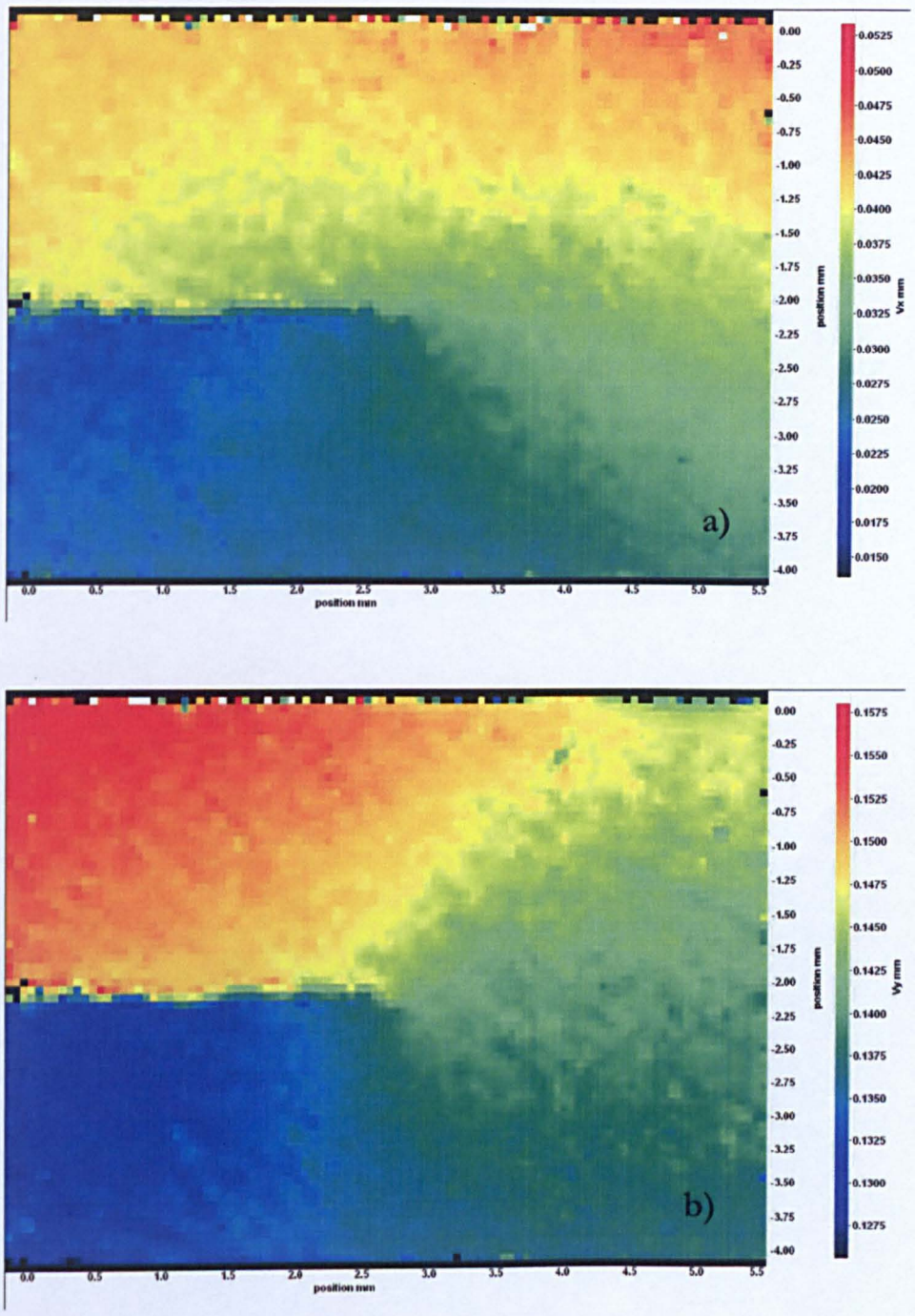

Figure 4.18: Displacement fields with the information split in horizontal and vertical components for pure mixed mode loading, $\theta = 60°$. The crack tip is approximately at (2.6, -2.1) and the crack is positioned to the left. (a) Horizontal displacements, *u*. (b) Vertical displacements, *v*.

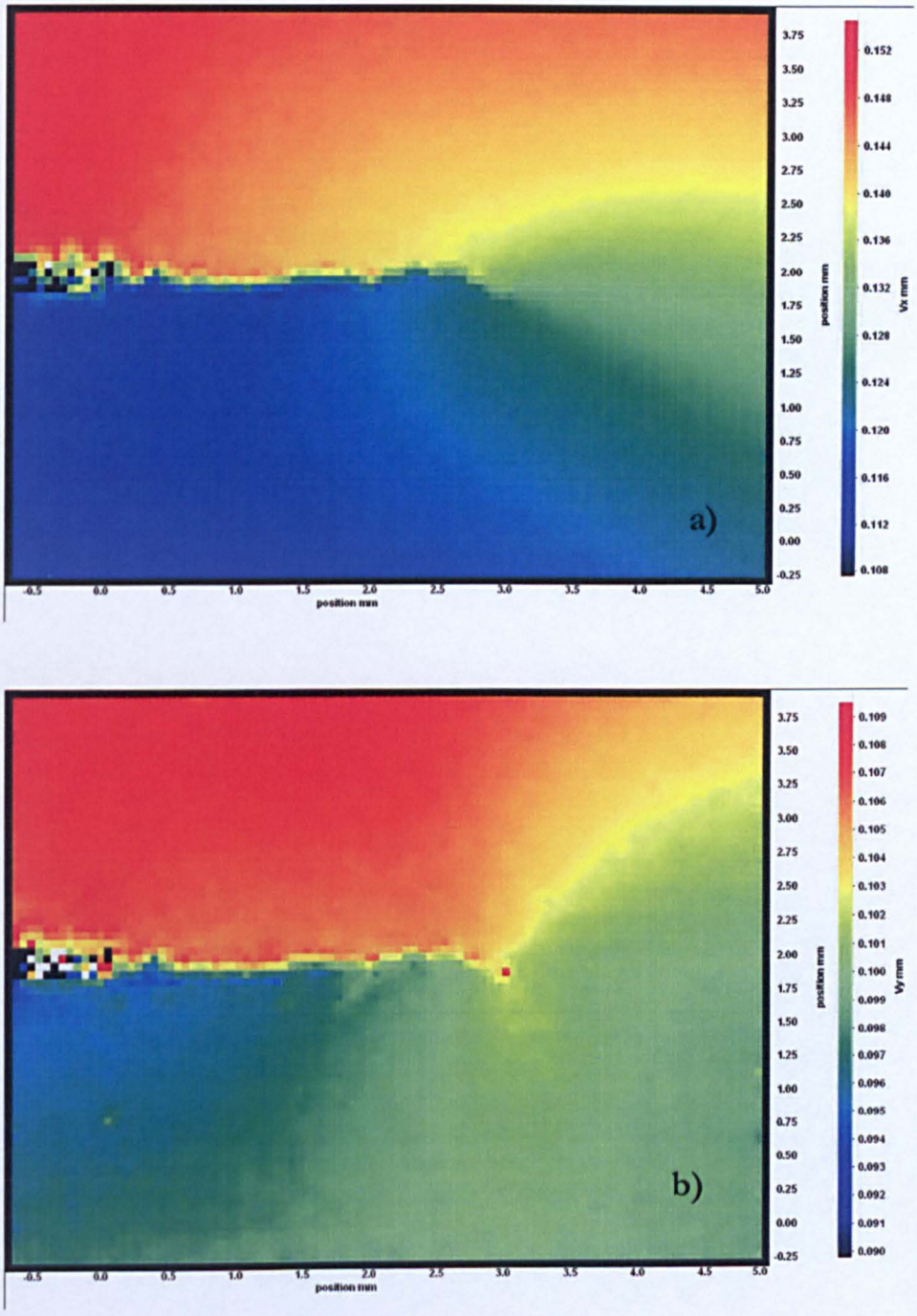

Figure 4.19: Displacement fields with the information split in horizontal and vertical components for mixed mode I loading, $\theta = 30°$. The crack tip is approximately at (3.0, 1.9) and the crack is positioned to the left. (a) Horizontal displacements, *u*. (b) Vertical displacements, *v*.

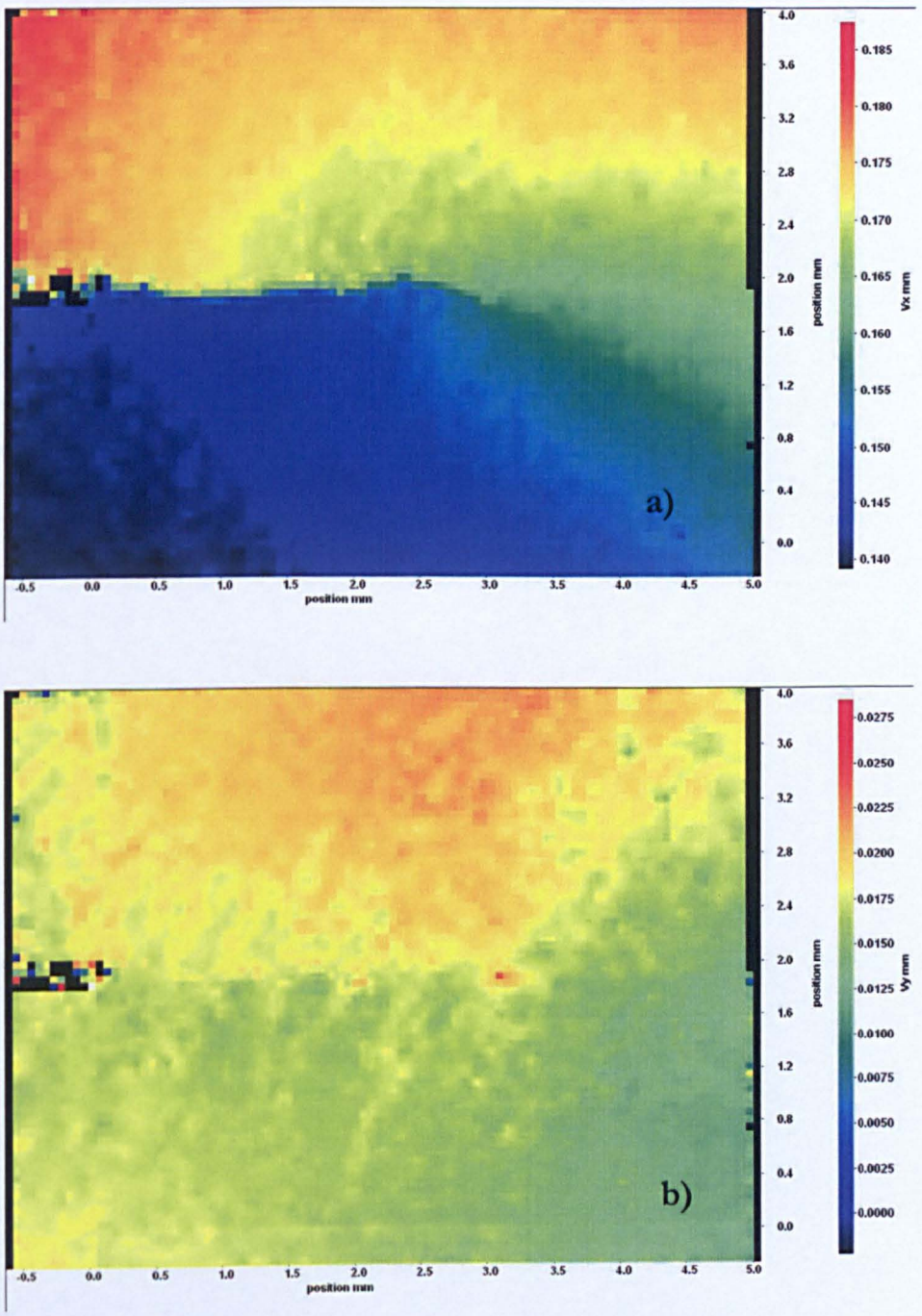

Figure 4.20: Displacement fields with the information split in horizontal and vertical components for pure mode II loading, $\theta = 0°$. The crack tip is approximately at (3.0, 1.9) and the crack is positioned to the left. (a) Horizontal displacements, u. (b) Vertical displacements, v.

Chapter 5

Crack tip positioning

5.1 Introduction

This chapter deals with the location of the coordinates of the crack tip. The crack tip which we will often refer to in the present chapter, represents the region at which fracture mechanisms such as inhomogeneous slip, void growth and coalescence, and bond breaking on the atomic scale take place. This is often regarded as the process zone.

The optical resolution of the digital image correlation systems in current use is insufficient to allow one to resolve the physical damage processes occurring around the crack tip. Since the aim of the work is to characterize the crack tip displacement field by Linear Elastic Fracture Mechanics parameters, the problem reduces to one of identifying a point, representative of the crack tip and the process zone, so that its coordinates can be used to calculate the SIF according to the methodology described in Chapter 3.

5.2 Inclusion of the crack tip coordinates as unknowns in the system of equations

The system of equations (3.18-3.19) presents the Fourier coefficients, α_k and β_k, as unknowns. The rest of the coefficients appearing in the left hand side of the system of the equations, i.e. C_k^j, D_k^j, E_k^j and F_k^j, depend upon the crack tip coordinates, as shown in equations (3.30-3.33). If the crack tip coordinates are not known, the system (3.18-3.19) becomes non-linear and can be solved only by means of iterative

methods. The solving of the system is done by optimising (minimising) an objective function, or error function, defined for the system of equations.
In many cases derivative methods have been employed, with the Newton-Raphson being the most commonly employed method for extracting stress intensity factors, from different experimental techniques [111, 28, 56]. However, in our case, the partial derivatives resulting from equations (3.18-3.19) are very complicated due to the presence of functions of the complex variable. Moreover, Newton-Raphson based methods are very sensitive to initial estimates, thus increasing the chances of finding a local minimum rather than the global minimum. In terms of the SIF solution, a local minimum means that the solution obtained is not satisfactory and does not provide any information about the SIF.
For these reasons, non-derivative methods have been considered for solving the non-linear system. In these methods the derivatives do not need to be computed, and the methods rely only on function evaluations.

5.2.1 Iterative methods

Recently, an optimization process was developed for extracting the SIFs, from thermoelastic [43] and photoelastic data [29]. Similar to the present case, the equations were based on Muskhelishvili's description of the crack tip field, but unlike the current system, the system was derived from stresses, rather than displacements. The iterative method employed in the optimization process included a combination of genetic algorithms and a local search technique, and for that system, it proved to be fast and robust for solving for the SIFs. Given the similarities between both problems, an attempt was made to extend the methodology to our case.
The approach consisted of initially finding the area where the global minimum is, by means of genetic algorithms, followed by a second stage where a local search technique was employed to speed up the convergence to the global minimum.

5.2.2 Genetic algorithms

A genetic algorithm is an iterative procedure inspired by biological evolution. It works by breeding a population of new possible solutions, from old solutions, with a methodology based on survival of the fittest. During the iteration process, the initial population of solutions will improve, and it will converge to an optimal solution [112].

The flow chart from Figure 5.1 shows the steps followed by the algorithm.

For the evaluation of the population an error function (called fitness function in evolutionary algorithms) was developed. The error function was built in a least-squares sense, so that the difference between the left hand-side and right hand-side of equations (3.50-3.51) is minimised. Accordingly, the error function was constructed as a square root of the sum of the squares of the residuals of the system, that is:

$$F = \left\{ \sum_{j=1}^{p} \left(\left[\sum_{k=-N}^{N} \left(C_k^j \alpha_k + D_k^j \beta_k \right) - 2\mu u^j \right]^2 + \right. \right.$$

$$\left. \left. + \left[\sum_{k=-N}^{N} \left(E_k^j \alpha_k + F_k^j \beta_k \right) - 2\mu v^j \right]^2 \right) \right\}^{1/2} \tag{5.1}$$

Each computation of (5.1) takes about 15 seconds. In order to guarantee the convergence to the global optimum, the error function needs to be evaluated of the order of 10^5 times. Therefore, for this case, the approach is impractical due to the high computational cost.

The solving of the system can be simplified considerably by splitting the problem into two stages. A first stage, where the crack tip coordinates are determined directly from the displacement data, followed by a second stage where the system of equations (3.50-3.51) is solved. The problem is enormously simplified, as the system of equations becomes linear. Consequently, it can be solved in a linear least-squares sense, as shown in Chapter 3.

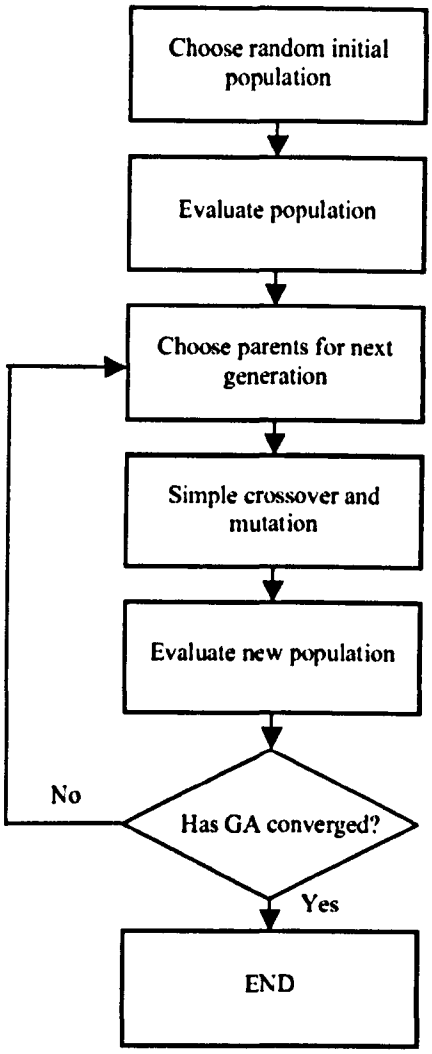

Figure 5.1: Flow chart illustrating the steps followed by a simple genetic algorithm. (After Pacey et al. 2005).

5.3 Crack tip positioning from displacements

The presence of a crack in a body implies a discontinuity in the body. However, this discontinuity may be obscure and sometimes invisible when the surface of the body is observed. An inappropriate resolution, poor illumination, a high level of mode II loading or small CTOD range, may result in making the tip of the crack unclear. The properties of the material may also make difficult the task of finding the crack. Nevertheless, a discontinuity in the displacement fields will always occur, by

definition of the crack. This fact is exploited in order to extract information about the crack tip position.

When an elastic body with a crack is submitted to any loading conditions, a delimitation is observed along the crack path in the displacement field. This delimitation can be detected with an edge-finding routine.

5.3.1 Edge-finding techniques

Edge-finding techniques are those employed for identifying the pixels that belong to the borders of an object in an image. In this work the Sobel edge-finding routine from the Image Processing Toolbox in Matlab was used [113].

A digital image is a two dimensional array of intensity values, $I(x,y)$. The edge-finding routines work by weighting, for each pixel of the image, the contribution of all the pixels in its neighbourhood, with different coefficients. According to the Sobel operator [114], each pixel $I(i,j)$ of the image is substituted by the following expression:

$$S(i,j)=\sqrt{H(i,j)^2+V(i,j)^2} \tag{5.2}$$

where each of the addends is obtained as:

$$\begin{aligned} H(i,j)=&-I(i-1,j+1)-2I(i-1,j)-I(i-1,j-1)+\\ &I(i+1,j+1)+2I(i+1,j)+I(i+1,j-1) \end{aligned} \tag{5.3}$$

and

$$\begin{aligned} V(i,j)=&I(i-1,j+1)-I(i-1,j-1)+2I(i,j+1)-\\ &-2I(i,j-1)+I(i+1,j+1)-I(i+1,j-1) \end{aligned} \tag{5.4}$$

Equation (5.2) is the magnitude of the gradient. The routine detects the edges at those points where the gradient of $I(x,y)$ is maximum.

To identify the tip of the crack, the edge-finding routine was applied to the displacement field image measured by image correlation. The tip was then located at the end of the detected edge.

In order to test the performance of the technique for positioning the crack tip coordinates, the technique was applied to different loading cases and the results were compared with those obtained locating the crack tip with a travelling microscope, described in Chapter 4. A series of cross marks was engraved in the surface in order

to introduce a common origin of coordinates between both techniques, for comparison purposes (see Figure 4.14).

A load of approximately 15KN was applied to a centre crack plate while images were being recorded. Utilization was made of the grips allowing seven different mixed mode loads. Accordingly seven loading cases were studied, ranging from pure mode I loading to pure mode II loading. Soon after the images were recorded the travelling microscope was positioned in front of the surface to measure the Cartesian coordinates of the tip. The spacing between displacement vectors was approximately 60 μm per pixel.

For each loading case, the edge-finding routine was applied separately to both horizontal and vertical displacements. Depending on the degree of mixed mode, the crack tip is better identified in the horizontal or in the vertical displacement. If the mode I component is predominant over the mode II component, the crack will appear clearer in the vertical displacement. Conversely, when the mode II component is predominant, the crack can be recognized better in the horizontal displacement. In practice, once the edge-finding routine is applied to both horizontal and vertical displacement fields, the crack tip is extracted from the field which shows larger crack length. This is explained in Figure 5.2.

The results obtained for both horizontal, x, and vertical, y, coordinates, for different mixed modes in a centre crack panel are shown in Figures 5.3 and 5.4. These results were obtained for the different images captured between 4 and 15 KN. It was observed that below 4 KN (or 3 MPa$\sqrt{m}$), due to very poor signal to noise ratio, the results become inconsistent. The fact that the specimen was subjected to a number of cycles in between each loading case implied a certain crack growth in between each loading case. Consequently different crack tip locations were observed in the different loading cases.

In both x and y coordinates, all the results were within one spacing of the displacement vectors, ranging the errors in x from 35% of one vector spacing to 98%. In the case of the vertical coordinates the errors ranged between 11% and 85% of one spacing between displacement vectors. Therefore, it is believed that the resolution for measuring the crack tip coordinates with this approach is limited by the resolution of the displacement images.

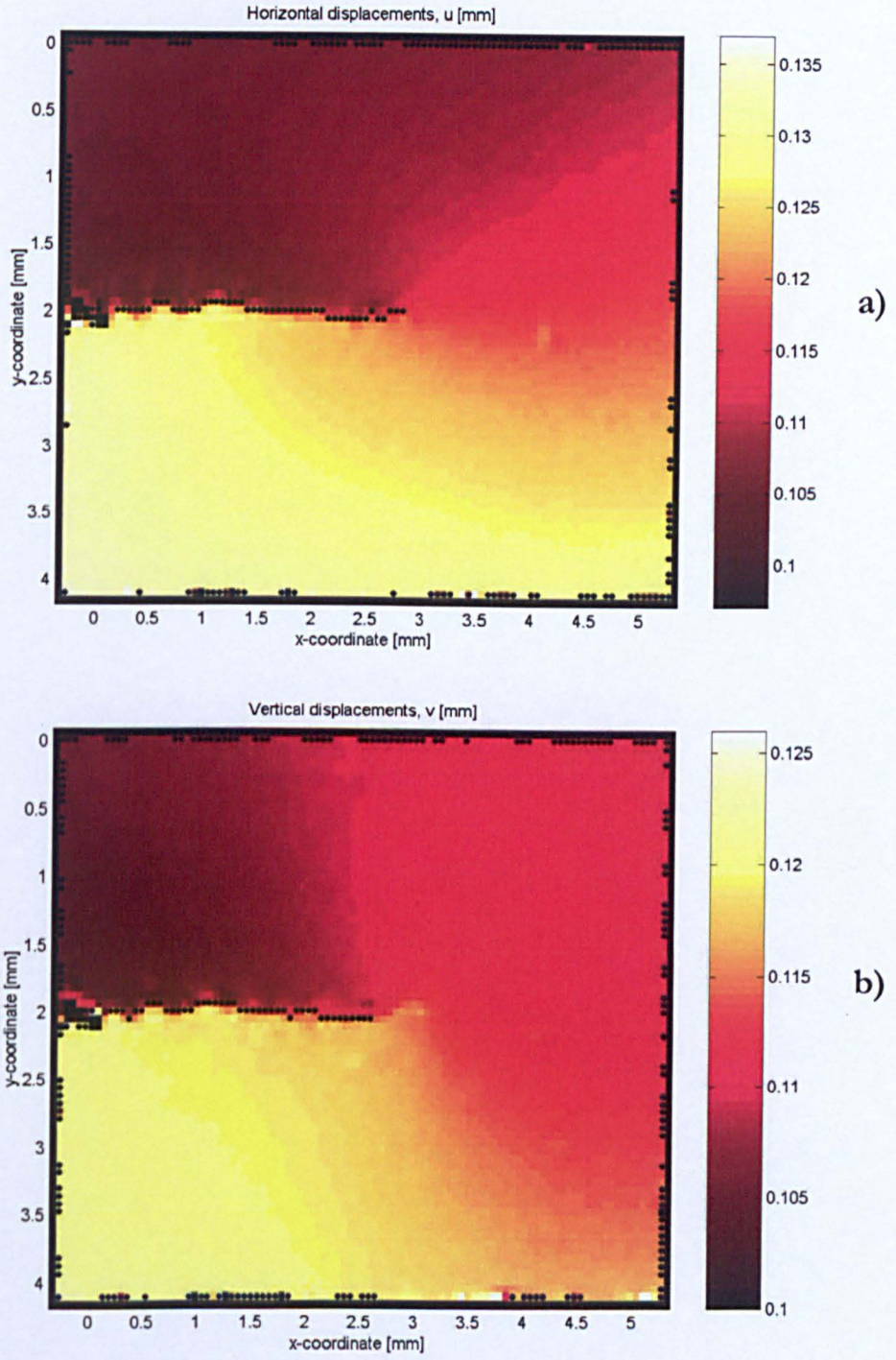

Figure 5.2: Results of applying the edge-finding routine on the (a) horizontal and (b) vertical displacements. The crack is positioned horizontally, and the growing direction is from left to right. The displacements were obtained from a centred crack panel loaded at $\theta = 45°$. The coordinates of the tip according to (a) are (2.81, 1.99) and according to (b) (2.59, 2.04). Consequently, the displacement that predicts a larger crack length is taken as valid, that is (2.81, 1.99) from horizontal displacement.

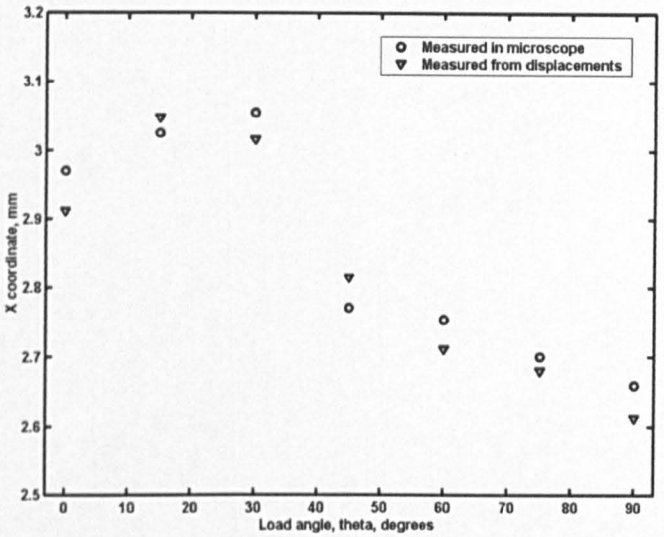

Figure 5.3: Horizontal coordinate measured with travelling microscope and obtained from edge-finding routine, for seven loading cases, from pure mode II ($\theta = 0°$) to pure mode I ($\theta = 90°$).

Possibly, the fact that the error in all of the cases was smaller than the pixel resolution is caused by a completely arbitrary factor, namely: how far the actual crack tip in the image is from the boundaries of the pixel which contains the crack tip. If it happens that the actual tip falls exactly in the centre of the pixel which identifies the tip, then the error associated with the crack tip positioning will be zero. In the rest of the cases, the further the real tip is from the centre of the pixel, the higher will be the related error.

Barker *et al.* [47] pointed out that the effect of not correctly locating the crack tip introduces a certain error in the final SIF values. In order to assess the severity of the errors introduced by identifying the crack tip with the above technique, an error analysis needs to be done.

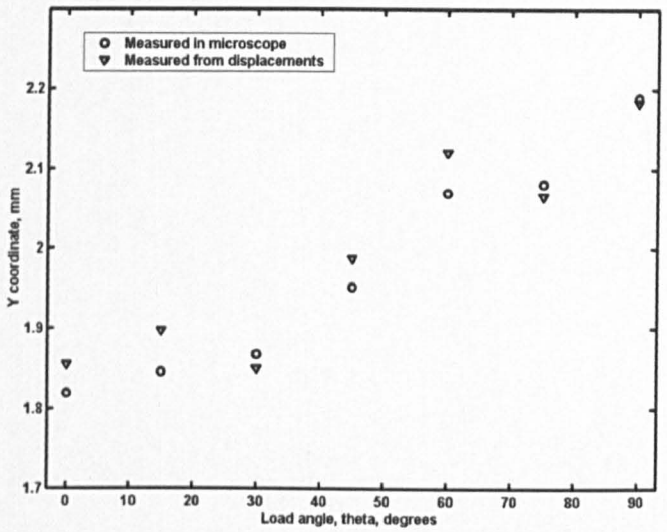

Figure 5.4: Vertical coordinate measured with travelling microscope and obtained from edge-finding routine, for seven loading cases, from pure mode II (θ = 0°) to pure mode I (θ = 90°).

5.4 Sensitivity analysis

In the sensitivity analysis, an attempt is made to find how much the error inherent to locating the crack tip with an edge-finding routine affects the calculated SIF. In order to cover the entire spectrum of mixed mode (I + II) loading, a centre crack plate, which allows loads from pure opening mode to pure sliding mode, and five loading cases in between (see Figure 4.2) was employed.

The error originated from the position of the crack tip is a systematic error in the data-points collected. The analysis was performed by shifting the crack tip coordinates a certain distance. Both x and y coordinates were independently shifted. Four distances related to the displacement resolution were chosen to simulate the errors introduced by locating the crack tip with the edge-finding routine. These were 0.2, 0.5, 1 and 2 times the resolution.

Figures 5.5 and 5.6 show the information related to moving the horizontal coordinate, and how it affects to the K_I values. Figures 5.7 and 5.8 present the results of shifting the x and y coordinates respectively, in the K_{II} values.

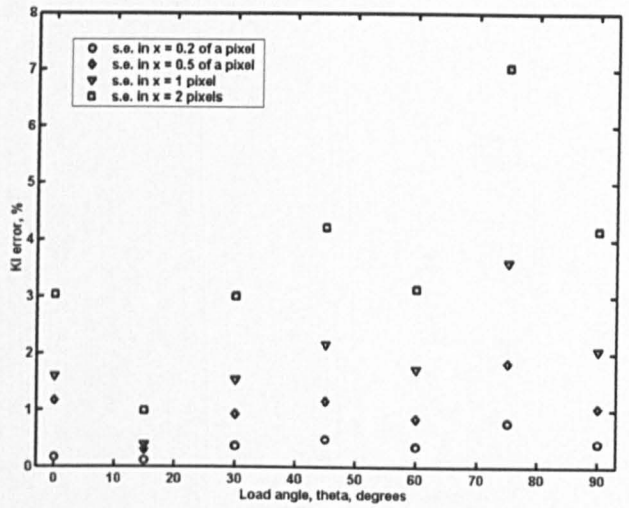

Figure 5.5: Effect of systematic error (s.e.) in x coordinate on K_I values, for seven loading cases, from pure mode II ($\theta = 0°$) to pure mode I ($\theta = 90°$).

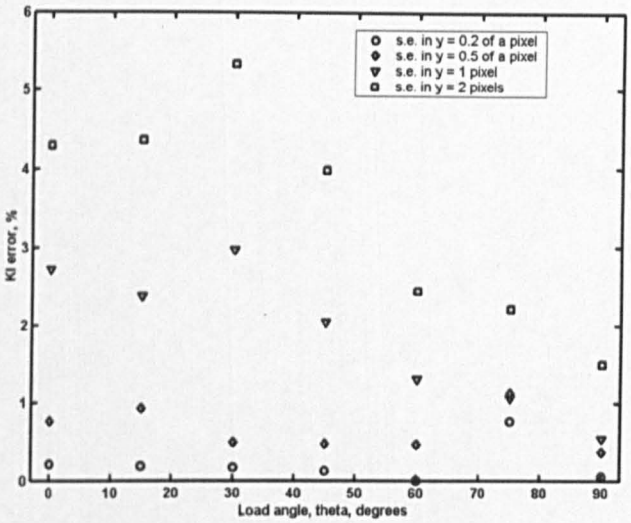

Figure 5.6: Effect of systematic error (s.e.) in y coordinate on K_I values, for seven loading cases, from pure mode II ($\theta = 0°$) to pure mode I ($\theta = 90°$).

As illustrated in the previous section, the resolution of location of the crack tip is smaller than one pixel. This fact is represented in Figures 5.5 to 5.8 by all of the points located below the triangular marks. For all the loading cases but one, an error smaller than 3.6% was observed in both K_I and K_{II}, when a systematic error of 1 pixel was introduced. The only exception occurred for the K_{II} values, in the case of θ

= 90°, i.e. pure mode I loading, where most of the points fall out of the vertical axis scale, with errors up to 70%.

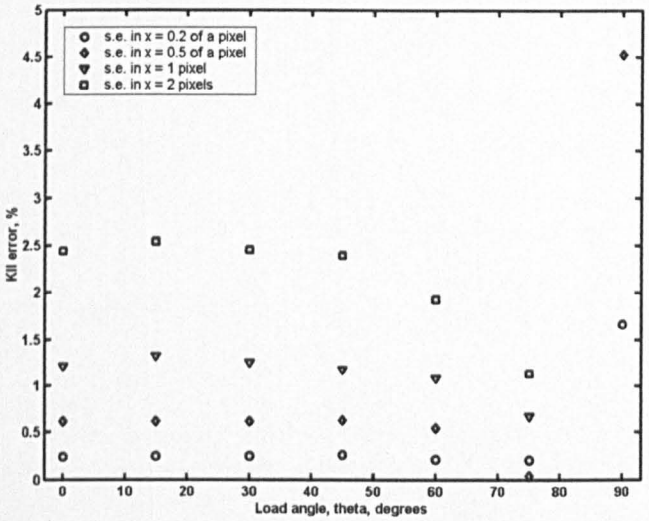

Figure 5.7: Effect of systematic error (s.e.) in x coordinate on K_{II} values, for seven loading cases, from pure mode II ($\theta = 0°$) to pure mode I ($\theta = 90°$).

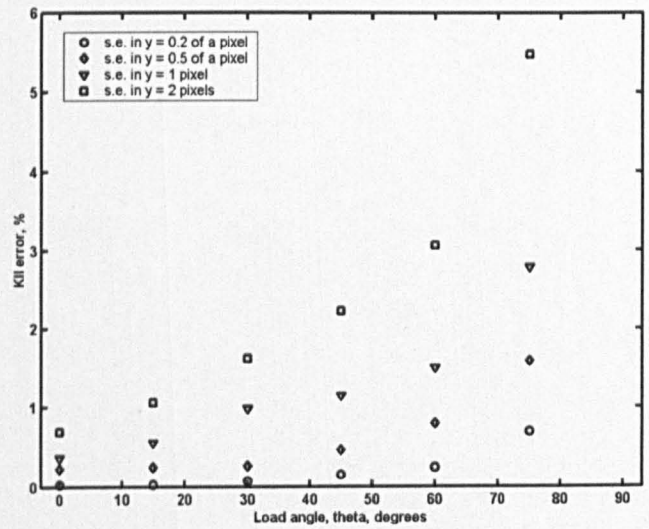

Figure 5.8: Effect of systematic error (s.e.) in y coordinate on K_{II} values, for seven loading cases, from pure mode II ($\theta = 0°$) to pure mode I ($\theta = 90°$).

For being opening mode, the K_{II} values are very close to zero. The same difference that generated an error of 1% for K_{II} values of 10 MPa$\sqrt{m}$, will result in a value of 50% for K_{II} values of around 0.2 MPa$\sqrt{m}$. Nevertheless, the differences existing in K_{II} for the 90° case, were of the same order as the rest of differences. For this reason,

the errors in K_{II} for mode I loading were not considered to draw conclusions about the effect of the crack tip location on the SIF.

Similar behaviour was expected for the errors in K_I for the case of the sliding mode. However, the K_I values were not so close to zero, possibly due to local mixed-mode loading and wedge opening of the crack [115]. As a result the K_I errors for $\theta = 0°$ are not so high as the K_{II} errors for $\theta = 90°$.

For the systematic error of 1 pixel, on average, the maximum error in K_I is 1.9% for the horizontal coordinate and 1.8% for the vertical coordinate. As regard the sliding mode SIF, again for a systematic noise of 1 pixel, the maximum average error for the x coordinate is 1.1%, and for the y coordinate 1.2%.

Based on the above values, it can be said that the edge-finding technique is an acceptable approach for identifying the tip of the crack when determining the SIF. The technique is limited by the resolution of the camera, which is directly related to the resolution achieved in displacements. For the resolution employed here, the edge-finding technique yields satisfactory results. It is expected that with the advent of better devices in digital photography, these results can be easily improved.

5.5 Conclusions

For evaluating the SIF the crack tip coordinates need to be known. An attempt was made to include the coordinates of the crack tip as unknowns in the system of equations for calculating the SIF. Nevertheless no method was found to solve satisfactorily, in terms of accuracy and time required, the resulting non-linear system of equations.

Adequate results were achieved by finding the coordinates prior to the solving of the system. The location of the crack tip was found by applying an edge-finding routine to the displacement fields measured around the crack.

The influence of the crack tip error on the SIF was also investigated. It was found that by locating the crack tip with the described method, an average error of less than 1.9 % and less than 1.2 % was introduced in K_I and K_{II} respectively. Consequently, this last approach proved to be the fastest and most robust among the different

methodologies studied. Therefore, in the next chapter the procedure will be applied to extract the SIFs in different geometries.

Chapter 6

Experimental determination of the stress intensity factor

6.1 Introduction

This chapter presents the results of applying the methodology for estimating mixed-mode SIF described in previous chapters to three different geometries. The chapter begins with an explanation of the parameters utilized in the methodology and a description of the variable employed for measuring the quality of the fitting between the elastic model and the experimental data. Then the results for pure mode I SIF determination are presented. Subsequently, based on these results, the uncertainty of the technique is estimated. In the following sections the results of applying the methodology to find mixed mode (I + II) SIF and monitoring of the SIF are presented. Finally discussion of all the information presented in the chapter is reported and conclusions are drawn in the last section.

6.2 Selection of the data points and number of terms

As explained in previous chapters, a system of equations for calculating the SIF needs to be solved (equation 3.20). In the system of equations, the right hand side term, b, depends upon the experimentally measured data points. The methodology was first developed for photoelasticity. Initially a single point was utilized for determining the opening mode SIF. The method was based on selecting a point with a certain location on a fringe loop from the isochromatic pattern. The methodology

was only applicable for problems where the shearing mode SIF is zero [20]. Subsequently, two carefully selected points were employed for determining both the opening and sliding mode SIF [21]. By collecting three points the necessity of collecting points from specific locations was avoided, and the information could be acquired from three arbitrary positions [21]. The resulting system of equations was deterministic.

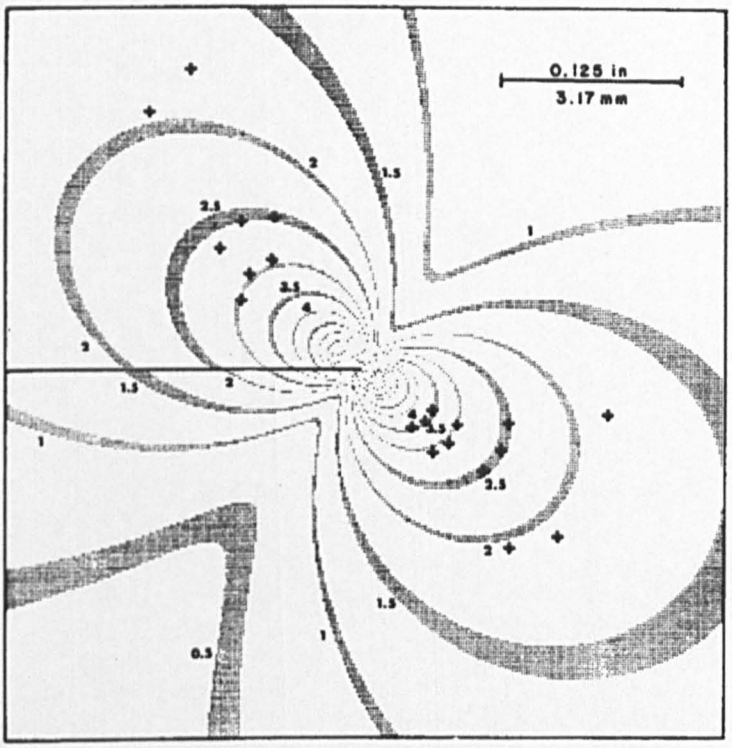

Figure 6.1: Collected data points from isochromatic fringe field for determination of the SIF from photoelastic data. The 20 experimental data points are shown as crosses. (After Sanford and Dally 1979).

Based on previous approaches, the multiple-points over-deterministic method was developed [21], allowing the use of the full-field data. In this case the experimental information was collected from 10 or 20 points (see Figure 6.1). No specific location was required for these 10 or 20 points. The advantages of over-determining the system of equations by a factor of ten was investigated by Barker et al. [47]. It was discovered that the effect of random noise in the experimental data was reduced by increasing the number of collected points. In the next two decades, the approach was employed and improved in photoelasticity [26-29] and thermoelasticity [42-43]. New

developments in the field of computer science allowed an increasing number of data points to be collected. In the case of thermoelasticity, the best accuracy was obtained using a circular array for collecting the data. The boundaries of the array were approximately coincident with the boundaries of the K-dominated region (see Figure 6.2). The most precise results were obtained from around 400 data points [43].

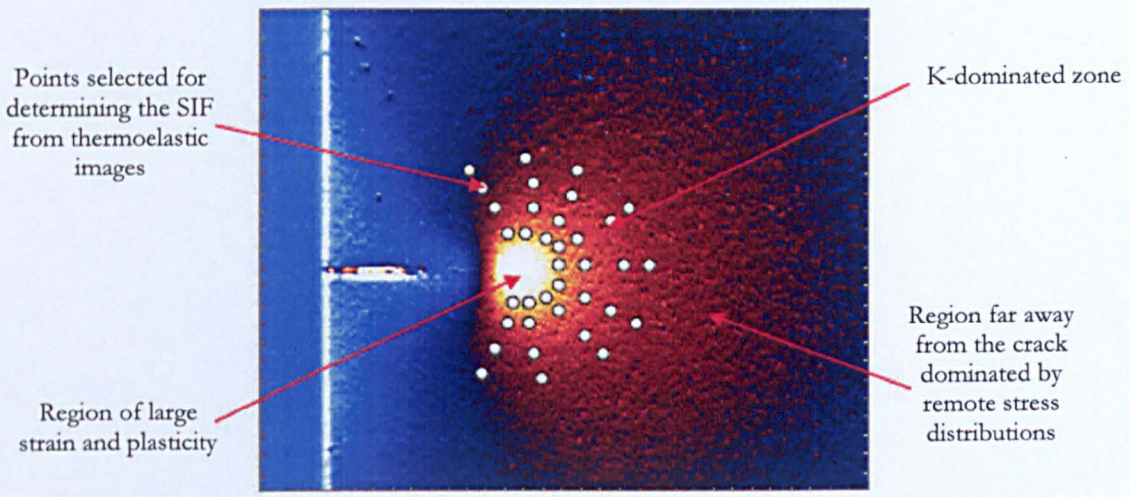

Figure 6.2: Typical stress field in the neighbouring of a crack subjected to pure mode I loading, acquired by thermoelastic stress analysis. The origin of the crack is located at the left side of the image. A schematic of the selected data points for SIF determination is also shown. (After Díaz et al. 2004).

Important differences between the stress fields provided by thermoelasticity and the displacement fields measured by image correlation can be observed (see Figures 6.3 and 6.4). In the case of thermoelastic data, a strong signal gradient in the immediate surroundings of the crack tip exists. However, displacement fields are much smoother and, with the exception of the crack flanks, no strong gradient can be found across the image. Moreover, in the case of stress fields, once outside the K-dominant zone, the signal is weaker as the distance from the crack tip increases. By contrast, in the case of displacement fields, the trend is very different. When proceeding from the crack tip towards the crack mouth, the signal to noise ratio is improved as the opening displacement increases (see Figure 6.4).

Analytically, the different fields of stress and displacement can be seen by examining Westergaard's solutions.

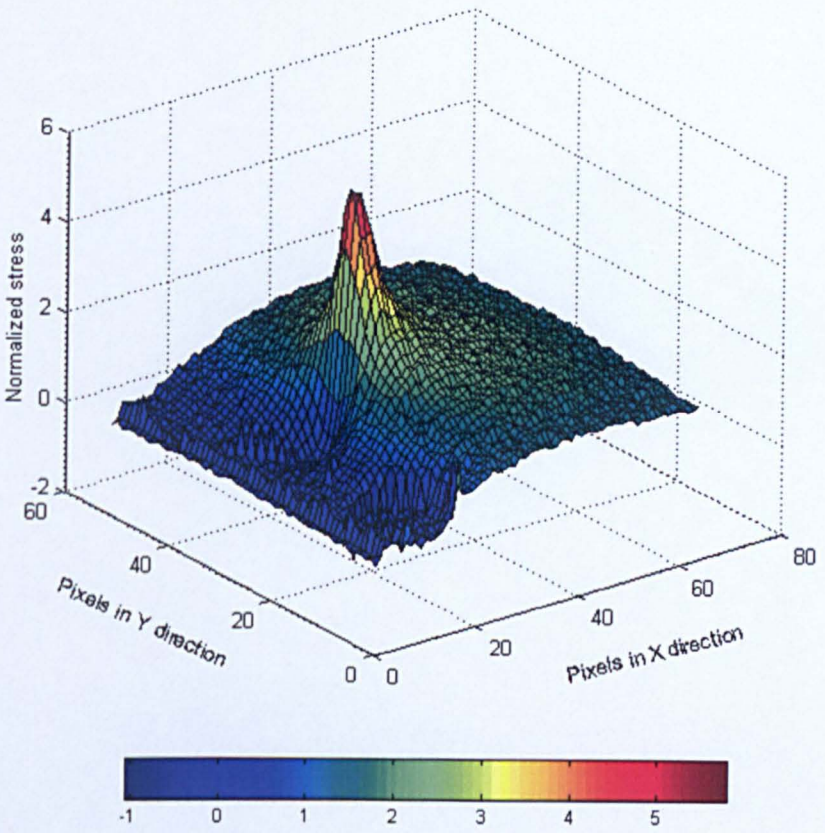

Figure 6.3: Example of a 3D representation of a stress field around a crack subjected to pure mode I loading, acquired by thermoelastic stress analysis. (After Díaz et al. 2004).

The expressions of stresses and displacements, at any point with polar coordinates, (r, θ) are:

$$displacement = \frac{K_I}{\mu}\sqrt{\frac{r}{2\pi}}f(\theta,\upsilon)+\frac{K_{II}}{\mu}\sqrt{\frac{r}{2\pi}}g(\theta,\upsilon) \tag{6.1}$$

$$stress = \frac{K_I}{\sqrt{2\pi r}}h(\theta,\upsilon)+\frac{K_{II}}{\sqrt{2\pi r}}k(\theta,\upsilon) \tag{6.2}$$

where μ is the shear modulus and υ is the Poisson's ratio. The functions f, g, h and k are certain functions of the angular coordinate and the Poisson's ratio, whose exact form can be found in any Fracture Mechanics text book (see e.g. [4]).

As appears in above equations (6.1) and (6.2), an asymptote exists in the case of the stress equation. Therefore, in the origin of coordinates, where $r = 0$, the expression tends to infinity. However no singularity is observed in the displacement equation (6.1), as they vary with $r^{1/2}$.

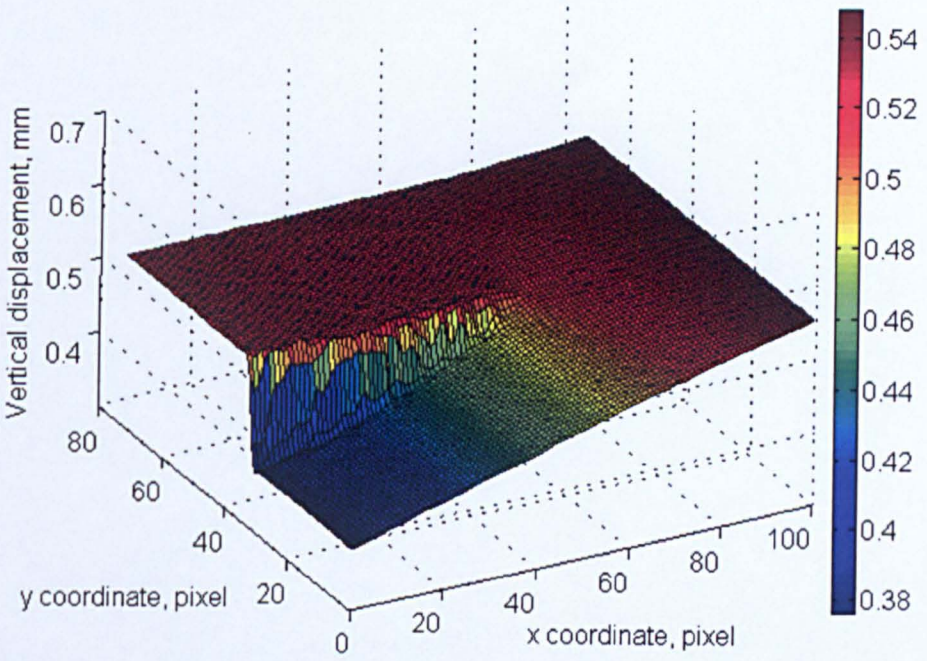

Figure 6.4: Example of a 3D representation of a vertical displacement field surrounding a crack of a sample subjected to pure mode I loading. The data was measured with image correlation.

Consequently, the areas around the crack for collecting stress and strain data and the areas for collecting displacement data are quite different. Displacement data in the crack wake, remote from the crack tip but still dominated by the crack deformation will provide results with a higher signal to noise ratio than data collected ahead of the crack tip.

In addition, in the case of the system of equations derived for image correlation data, the best stability can be achieved by collecting as many points as possible, as explained in Chapter 3.

Hence, to give combination of a better signal to noise ratio in locations removed from the crack tip and better stability and minimization of the noise with increasing number of points, a rectangular shaped array was employed for collecting the data points. The array spanned approximately the whole image, with the exception of the region very close to the crack tip, where the elastic model employed is not valid, and the data near the crack flank and near the boundaries of the image, which have a high degree of noise due to the correlation algorithm. Accordingly, the minimum distance

from the crack tip was larger than the plastic zone size, r_p, which can be estimated to a first approximation, as follows [59]:

$$r_p = \frac{1}{\pi}\left(\frac{K_I}{\sigma_y}\right)^2 \tag{6.3}$$

where σ_y is the yield stress of the material.

Examples of rectangular arrays employed for calculating the SIF are shown in Figures 6.6, 6.12 and 6.15.

Following the suggestions from Chapter 3, in order to reach a balance between accuracy and stability, 7 terms in the series ($2N + 1 = 7$) were employed.

6.3 Measuring the quality of the fitting

The quality of the least-squares fitting performed to solve the system of equations, and hence to extract the SIF, was evaluated using the residual of this fitting. The relative residual, ρ, of the system of equations (3.20) can be expressed as [116]:

$$\rho = \frac{\|b - Ax^*\|}{\|b\|} \tag{6.4}$$

where the symbol $\|\ \|$ represents the 2-norm of a vector, and x^* is the vector with the calculated values from solving the system of equations. The denominator makes the quantity scale-independent.

Mathematically, the residual estimates the differences between the calculated left-hand side of equation (3.20) and the right-hand side term. The physical meaning of the residual is the discrepancy between the constructed displacement field and the actual displacement field measured with image correlation. In other words, the parameter evaluates how much the model is able to adapt itself to the experimental data. High values of ρ will be indicative of poor quality of the fitting.

6.4 Pure mode I SIF determination

Five different wedge opening loaded specimens were fatigue pre-cracked as explained in section 4.3. In order to assess a wide range of possibilities within the same

geometry, five different crack lengths, *a*, were achieved, ranging from 24 to 54 mm. One single crack length was studied in each specimen. For this geometry, the crack length is defined as the horizontal distance from the point where the load is applied to the crack tip (see Figure 4.1). Three different loads were applied to each specimen. The loads applied in all the cases are summarized in Appendix D. The displacement field associated with each loading case was obtained with image correlation. The 55 mm macro lens setup was employed for this experiment. Accordingly, the image had a relation of 15 μm per pixel.

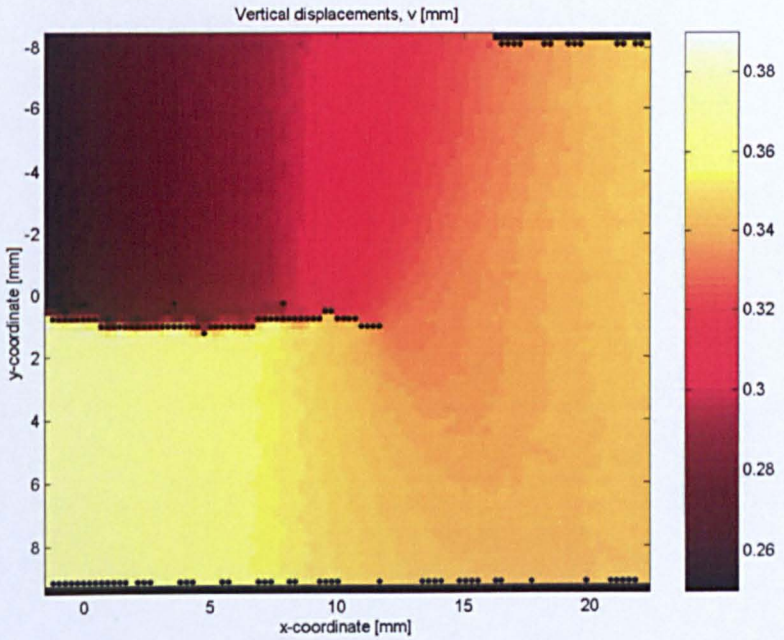

Figure 6.5: Results of applying the edge finding routine on vertical displacements measured on a wedge opening loaded sample. Accordingly the crack tip is located at (11.71, 0.99).

A 32 × 32 pixel final interrogation window, combined with a 50% overlap produced a spacing between displacement vectors of 240 μm. The data looked qualitatively similar to those shown in Figure 4.15.a.

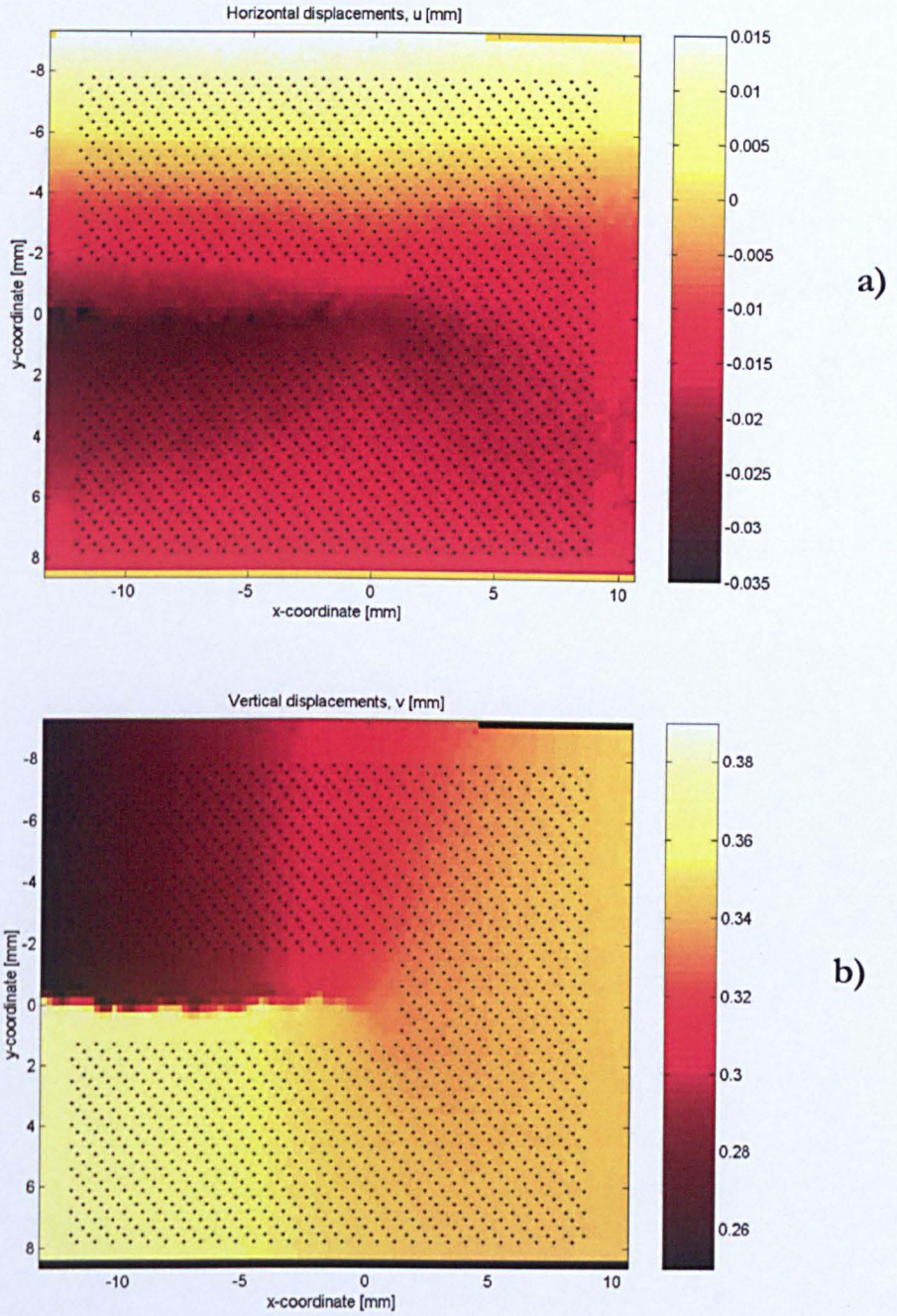

Figure 6.6: Array with selected displacement points considered for the SIF calculation in (a) horizontal displacements and (b) vertical displacements. Note that the origin of coordinates is shifted with respect Figure 6.5. In the current figure the origin is located at the crack tip.

For each wedge opening loaded sample, the coordinates of the crack tip were found by applying the procedure explained in Chapter 5 to the images captured when the

maximum load was applied to the sample. An example of the results generated by the edge finding routine for a wedge opening loaded sample is presented in Figure 6.5. Subsequently, as an intermediate step before adopting the system of coordinates of Figure 3.1, the origin was positioned at the crack tip (see Figure 6.6). An array of around 1700 points was sampled from the image correlation data. A typical example of an array for collecting the data points in the wedge opening specimen is shown in Figure 6.6.

Finally a system of equations was built, according to expression (3.20) and solved. The SIF was obtained from the solution of the system, according to section 3.7.

The results for the pure mode I SIF are shown in Table 6.1. The nominal K_I was calculated according to [107]. The last column of the table shows the relative residual generated in each SIF computation.

Good correlation is observed between theory and experiments. In most of the cases the error is smaller than 5%. This can also be seen in Figure 6.7, where the error is plotted against the nominal SIF. The only two cases where the error was greater than 5% occurred when K_I was very small. The absolute differences between theory and experiment in these two cases were similar to all the other data. Moreover, the nominal SIFs for these two cases were the smallest ones mainly as a consequence of very small loads. This fact is illustrated in Figure 6.8, where the errors are plotted against the applied load.

Figure 6.9 presents the normalized mode I SIF against the crack length. No influence is observed of the crack length on the accuracy of the results.

The very small values of the relative residual indicate a very good least-squares fitting. That is, the number of terms in the series employed provides more than enough flexibility of the elastic model to adapt itself to the experimental field, and consequently the degree of conformity between both mathematical descriptor and experimental data is high. Accordingly, no substantial improvement would be obtained by increasing the number of terms. Yet the stability of the system would be reduced considerably, as explained in Chapter 3.

The calculated mode II SIF, K_{II}, ranged from 6×10^{-3} to 1.3 MPa$\sqrt{m}$. Nevertheless, given the CT-like configuration of the specimen, the nominal K_{II} is zero in all the cases. The small mode II component measured in some of the cases is probably due

to local mixed-mode originated at the tip of the crack as a consequence of saw tooth shape of the crack flanks. This fact can be appreciated more clearly in Figure 6.10. It shows an example of the tortuosity of the crack path in a wedge opening loaded specimen.

a, mm	$K_{I\,nom}$, MPa$\sqrt{m}$	$K_{I\,exp}$, MPa$\sqrt{m}$	$K_{I\,error}$, %	$K_{II\,exp}$, MPa$\sqrt{m}$	Residual, ϱ
24	24.05	23.70	1.4	5.8×10^{-3}	1.8×10^{-5}
24	13.92	13.49	3.1	0.67	1.0×10^{-5}
24	3.16	3.85	21.8	0.16	7.5×10^{-6}
31	19.43	19.24	1.0	0.29	2.2×10^{-5}
31	16.66	16.37	1.7	4.8×10^{-2}	1.8×10^{-5}
31	14.58	14.05	3.6	0.16	2.1×10^{-5}
34	20.83	21.39	2.7	0.91	5.7×10^{-6}
34	14.41	14.61	1.4	0.14	5.8×10^{-6}
34	9.48	9.54	0.6	0.18	4.5×10^{-6}
49	15.41	15.94	3.4	1.31	1.6×10^{-6}
49	13.39	13.24	1.1	1.07	2.0×10^{-6}
49	11.73	11.51	1.9	0.84	1.4×10^{-6}
54	17.82	17.63	1.1	1.01	1.0×10^{-5}
54	10.31	9.89	4.1	0.78	1.1×10^{-5}
54	2.34	2.07	11.5	8.9×10^{-2}	4.2×10^{-6}

Table 6.1: Mixed mode K values for wedge opening loaded specimens, under pure mode I loading, with different crack lengths, a. The K_I errors of the calculated SIFs are shown in the fourth column. The relative residual when solving the system of equations is also shown.

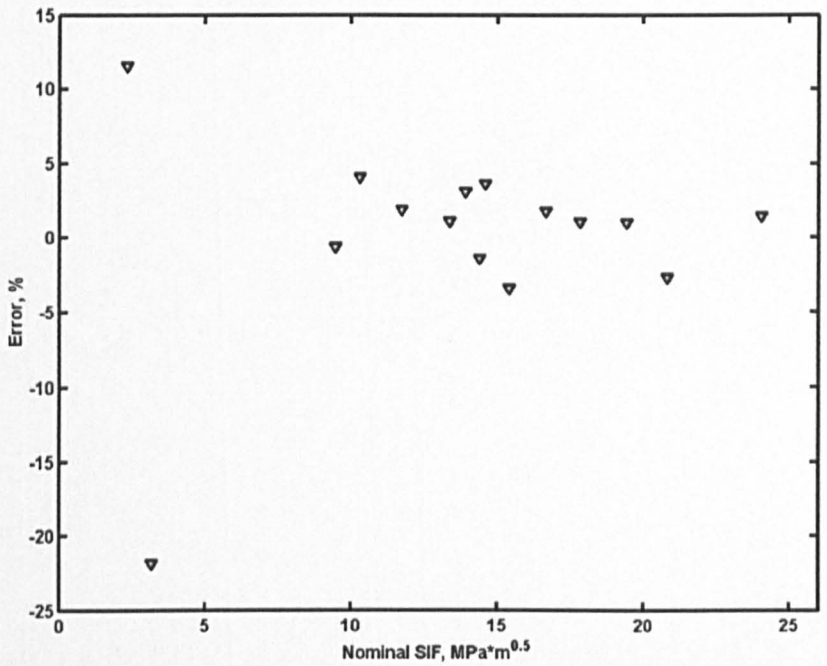

Figure 6.7: Measured errors plotted against applied SIF. The errors were obtained comparing experimental values with nominally applied, in wedge opening loaded specimens.

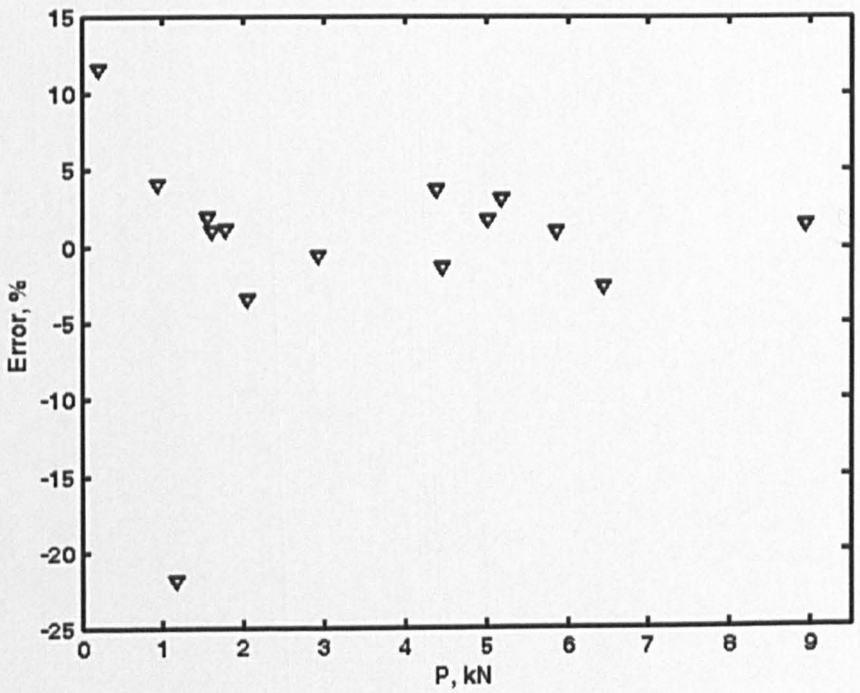

Figure 6.8: Measured errors plotted against applied load. The errors were obtained comparing experimental values with nominally applied, in wedge opening loaded specimens.

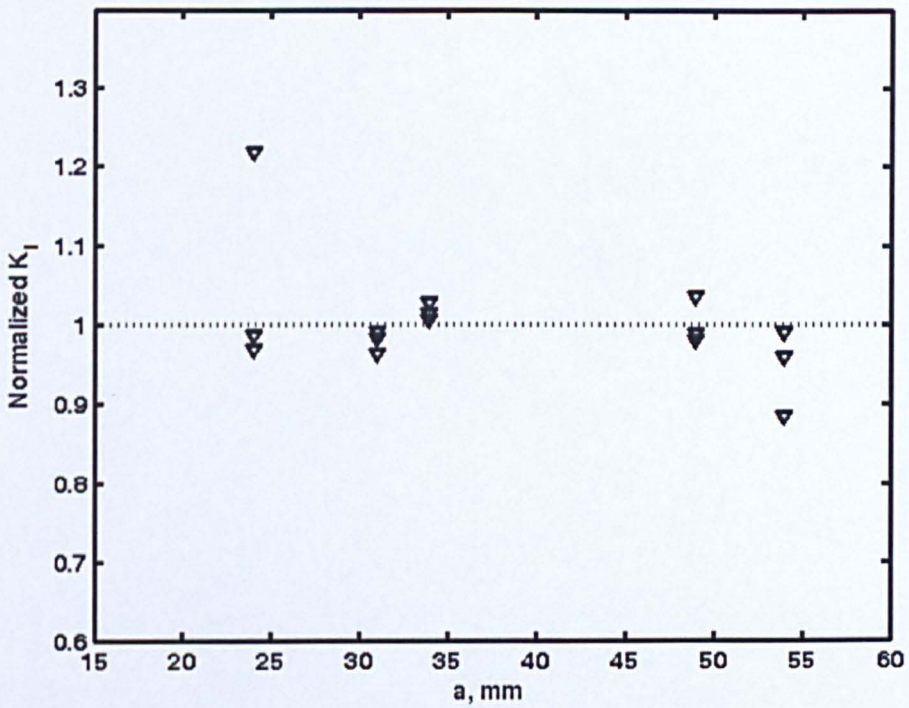

Figure 6.9: Normalized K_I for five different crack lengths, a, in wedge opening specimens.

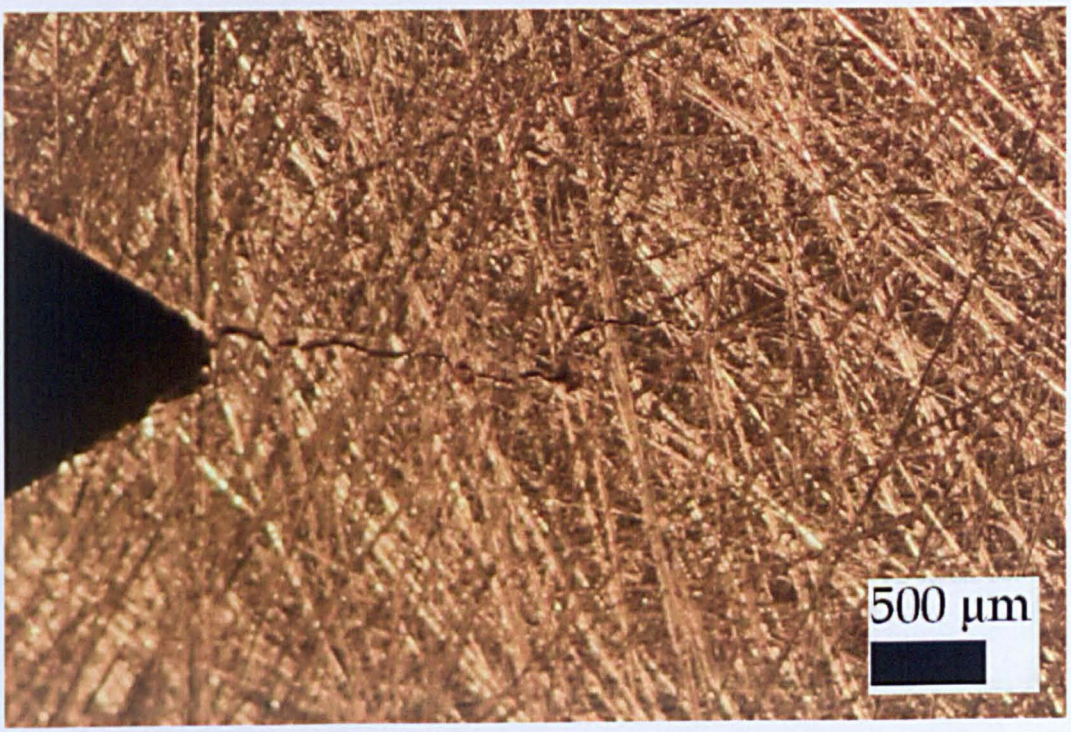

Figure 6.10: Photography of a typical fatigue crack grown in a wedge opening loaded specimen.

6.5 Quantifying the uncertainty

The technique for calculating the SIF presented herein, has a certain degree of uncertainty. The uncertainty is consequence of all the errors produced in the process of calculating the SIF, from the manufacture of the specimen to the last computation performed that yields the experimental SIF. Different sources of uncertainty include the error caused by misalignment of the loading, error of the applied load signal, random error generated by the heating of the CCD chip in the camera, error introduced when calculating the displacement field from the raw data, error arising from the location of the crack tip, error associated with the truncation of the series expansions developed in Chapter 3 and round-off error resulting from the numerical precision of the computer.

In order to evaluate the uncertainty, a series of experiments would be required for each geometry. Nevertheless, given the materials and time constraints of this work, only the experiment of the wedge opening loaded sample was repeated. In this section the uncertainty will be estimated for the wedge opening loaded geometry, and the conclusions will be extrapolated to the rest of geometries.

The error generated when finding the coordinates of the crack tip was evaluated in Chapter 5, and was found to be less than 1.9 % in K_I and less than 1.2 % in K_{II}.

It is difficult to quantify the uncertainty of the rest of the factors above mentioned. Nevertheless, the standard deviation of the results should provide a global measure of all the uncertainties influencing the methodology. In order to include the error in locating the crack tip, the standard deviation was calculated for five different crack lengths. In addition, the calculation was repeated three times corresponding to the maximum, intermediate and minimum loads shown in Table 6.1. Bessel's correction was used to account for the small size of the sample (five data). The resulting standard deviations for the three different loads are 0.023, 0.021 and 0.125 respectively. That is, the standard deviation is around 2%, with the exception of when a small load is applied to the specimen, for which the standard deviation increases up to around 12%. This trend can be also observed in Figures 6.7 and 6.8. The large standard deviation measured for the lowest applied load is clearly a consequence of the small magnitude of some nominal SIFs. For the samples with 24

and 54 mm crack length, when the minimum load was applied, although the errors are up to around four times bigger than the rest of the cases, the differences between nominal and experimental are of the same order. The fact that these two values raised the standard deviation to around 12% can be seen by calculating the standard deviation for the minimum load, but without these two data, i.e. considering only 31, 34 and 49 mm crack length. The standard deviation is then 0.021, which clearly falls in the same order as the calculated with higher loads. As a consequence, the data obtained for the minimum load will not be considered as they are not representative of the results, and the average between the other two standard deviations will be considered to quantify the scatter of the results, i.e. 0.022 or 2.2%.

By comparing this value of the standard deviation with the estimated error generated when locating the crack tip, it can be seen that the main contribution to the scatter is the error introduced when finding the crack tip coordinates. 86% and 54% of the error in K_I and K_{II} respectively, can be attributed to the location of the crack tip coordinates. This agrees well with previous works [21, 43, 47, 56] where the location of the crack tip is pointed as the major source of uncertainty when calculating SIF from experimental data.

Assuming a normal distribution of the results, the error bounds can be estimated as ± 2.2% with 68% confidence, or ± 4.4% with 95% confidence. It is also assumed that these error bars are load-independent. Consequently, in order to express them in terms of SIF, the percentages are applied to the average of the data utilized for estimating them. Accordingly the error bars are ± 0.36 MPa$\sqrt{m}$ and ± 0.73 MPa$\sqrt{m}$ with 68% and 95% confidence respectively.

Although the error analysis was done on one type of geometry, these error bars will be generalized to the rest of geometries, because the procedure followed in all the cases was the same.

6.6 Mixed mode (I + II) SIF determination: centre crack panel

A centre crack panel, as schematized in Figure 4.2, was tested in the loading machine shown in Figure 4.7. The sample was fatigue pre-cracked so that the total crack length, $2a$, was 64 mm. As explained in section 4.1, the 40-mm-central part of the

crack was machined by EDM. Accordingly, the fragment grown under fatigue was 12 mm long.

Only one crack length was studied with this geometry. On the other hand, seven different loading mixities were explored, ranging from pure mode I to pure mode II. The loads applied in the seven cases are shown in Appendix D.

In order to be consistent with the system of coordinates defined in Figure 3.1, for each mixed mode loading case the camera was rotated by the appropriate angle, so that the crack was positioned horizontally on the image. The marks engraved in the surface for the calibration (see Figure 4.14) were utilized to aid to this positioning.

The SIFs were obtained following exactly the same procedure as for the wedge opening loaded samples (see section 6.4). Examples of the edge finding routine result for locating the tip of the crack, and the array employed for collecting the points in a centre crack plate are presented in Figures 6.11 and 6.12.

The results of calculating the mixed mode SIF are shown in Figure 6.13. The nominal applied values were calculated according to [107]. The theoretical values for $\theta = 75°$ were obtained by interpolation, as this angle is not reported in [107].

The residuals from the least squares fitting were of the same order as in the wedge opening loaded specimen, thus indicating enough adaptability of the elastic mathematical model to the experimental data.

Overall there is a good agreement between the inferred SIFs and the nominal applied values in Figure 6.13. The accuracy in calculating both opening mode and sliding mode SIFs is approximately the same.

In the mathematical model developed, the crack was assumed to be a traction-free contour (equation 3.6). This assumption implies that the crack flanks do not touch each other. However, in the experiments herein presented and in many engineering fracture problems, the shape of the crack will be irregular and contact points occur along the wake, as the crack flanks touch each other and apply forces on each other. Moreover these phenomena may be augmented with the existence of a mode II component of the load. Accordingly, the assumption adopted in Chapter 3 may not be entirely correct, and a certain error can be introduced in the SIF for this reason.

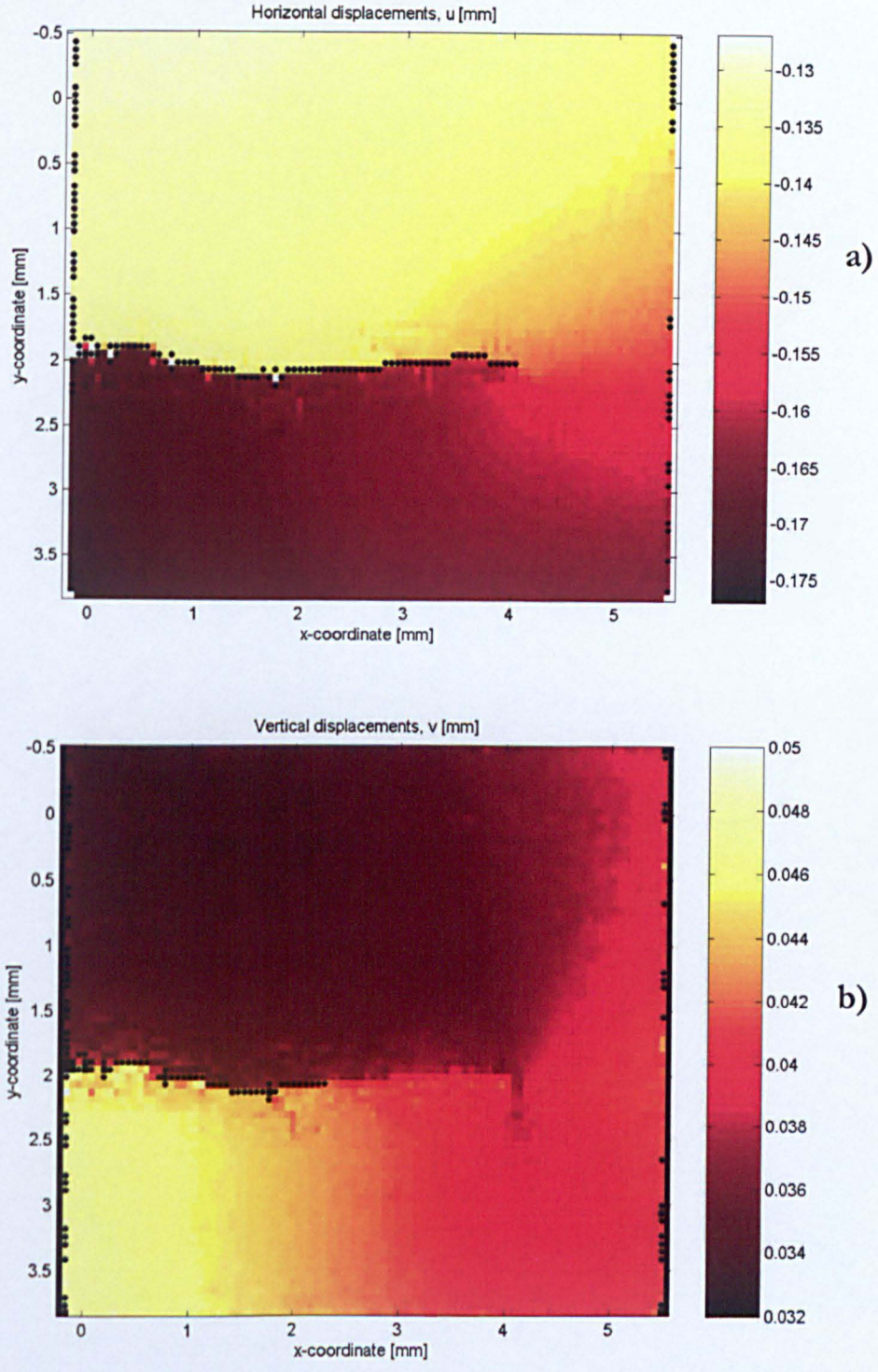

Figure 6.11: Results of applying the edge finding routine on (a) horizontal displacements and (b) vertical displacements, measured on a centre crack plate loaded at $\theta = 30°$. The crack tip coordinates, (4.04, 2.01), were extracted from the horizontal displacement.

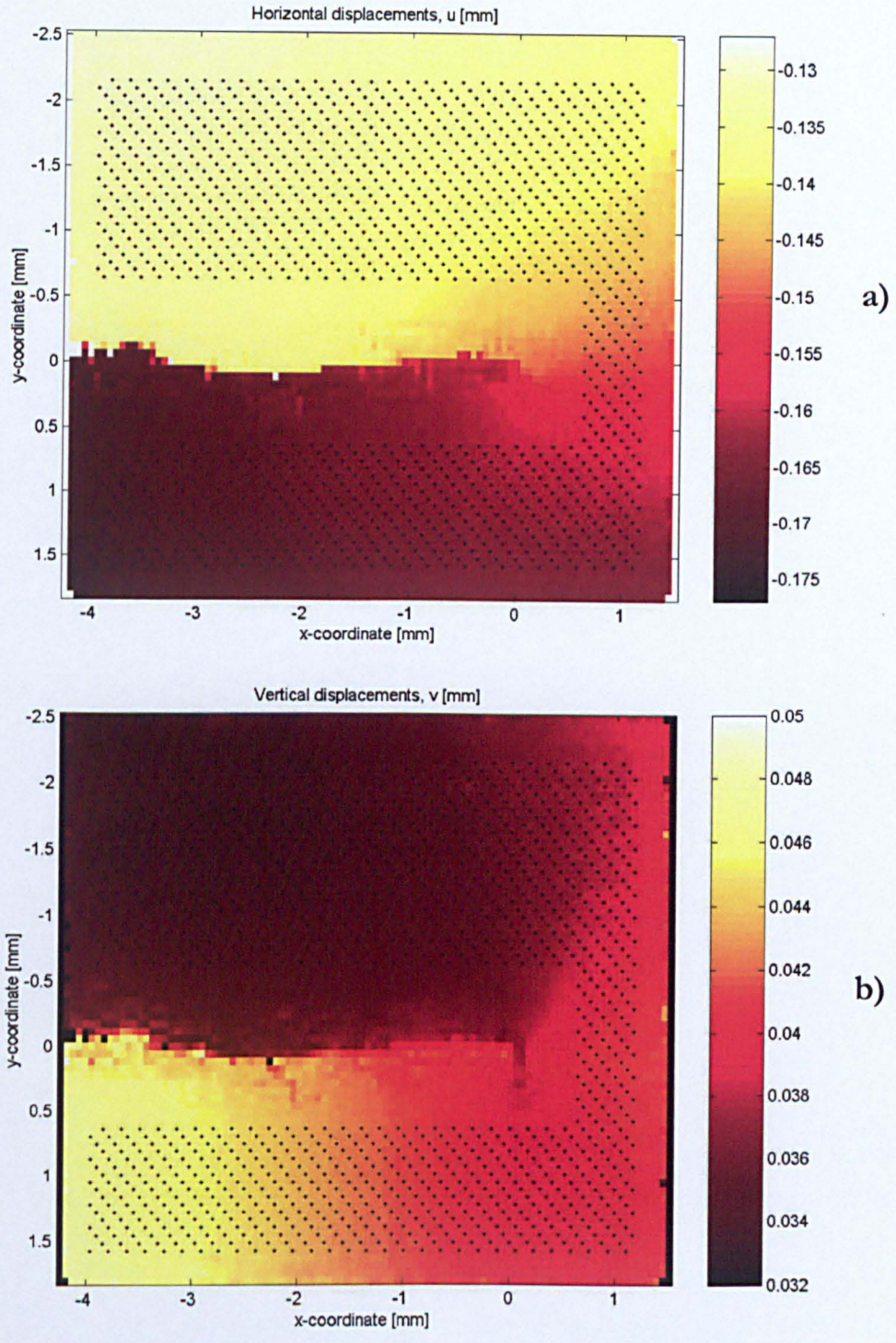

Figure 6.12: Array with approximately 1400 selected displacement points considered for the SIF calculation in (a) horizontal displacements and (b) vertical displacements of a centre crack sample loaded at $\theta = 30°$. Note that the origin of coordinates is shifted with respect Figure 6.11. In the current figure the origin is located at the crack tip.

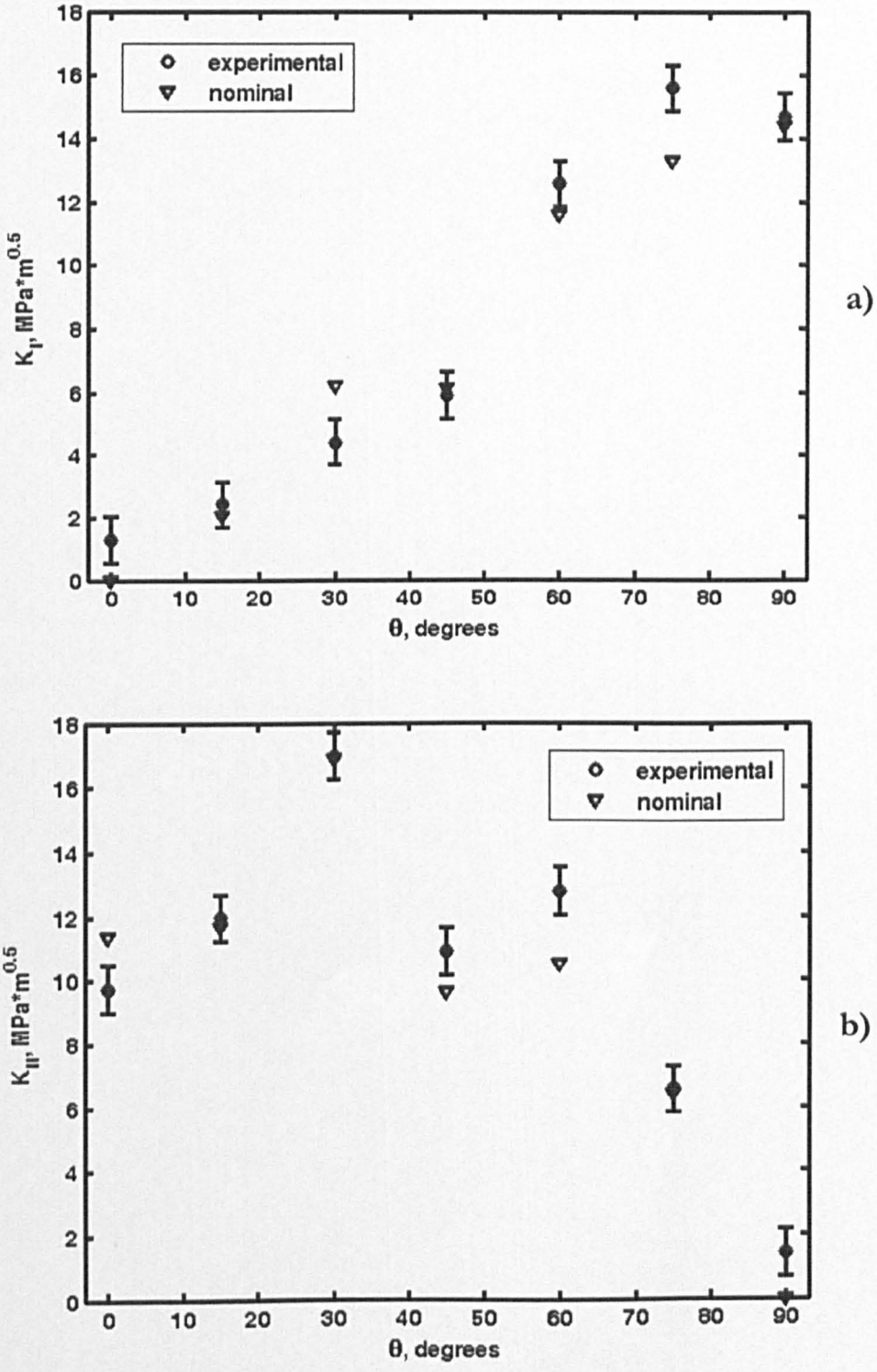

Figure 6.13: Experimental and nominal applied stress intensity factors obtained for the centred crack plate. Several loading cases are presented, with different mode mixity ranging from pure mode II, $\theta = 0°$, to pure mode I, $\theta = 90°$, with 15° increments showing (a) K_I and (b) K_{II}. The error bars in the experimental results are also plotted.

Another source of discrepancy between the nominal and the measured SIF arises from the fact that the fatigue crack was grown under pure mode I conditions, and the same crack was used for all the mixed mode analysis.

6.7 Mixed mode (I + II) SIF determination: free hole-in-a-plate geometry

The free hole-in-a-plate geometry described in section 4.1 was tested to determine mixed-mode (I + II). Following the procedure described in section 4.3, a fatigue crack was grown from the position of maximum stress on one side of the hole. The specimen was pre-cracked under a mode I cyclic load, with load ratio, R = 0.1 and stress intensity factor range, ΔK, of 10 MPa$\sqrt{m}$. 380,000 cycles were applied at a frequency of 10 Hz. Subsequently the crack length on either face of the sample was measured with a travelling microscope to be 5.25 and 4.70 mm long. The fatigue crack is shown in Figure 4.5.d. A certain curvature in the initial part of the crack can be noticed. This may be caused by not making the initial notch exactly at the equator of the hole in the position of maximum stress.

As in the case of the centre crack panel, one single crack length was subjected to seven mixed mode loadings (I + II). The loads applied are shown in Appendix D. The images were acquired in all the cases from the side where the crack length was 5.25 mm. Nevertheless, for computing the nominal applied SIF, the average of the crack lengths in both sides of the sample was used.

Following the same procedure as the case of the centre crack plate, the camera was tilted to make the crack horizontal. An example of the camera rotated 23.5° for the case of loading with $\theta = 23.5°$ is shown in Figure 4.11.

The procedure for estimating experimentally the SIFs was the same as in previous sections. The nominal SIFs for the pure mode I case were calculated from the solution for a radial crack at the edge of a circular hole given in [107]. For the rest of the cases, where mixed-mode loads were applied, the theoretical values were computed from the solution for an inclined crack emanating from an elliptical hole under tension, provided in [107].

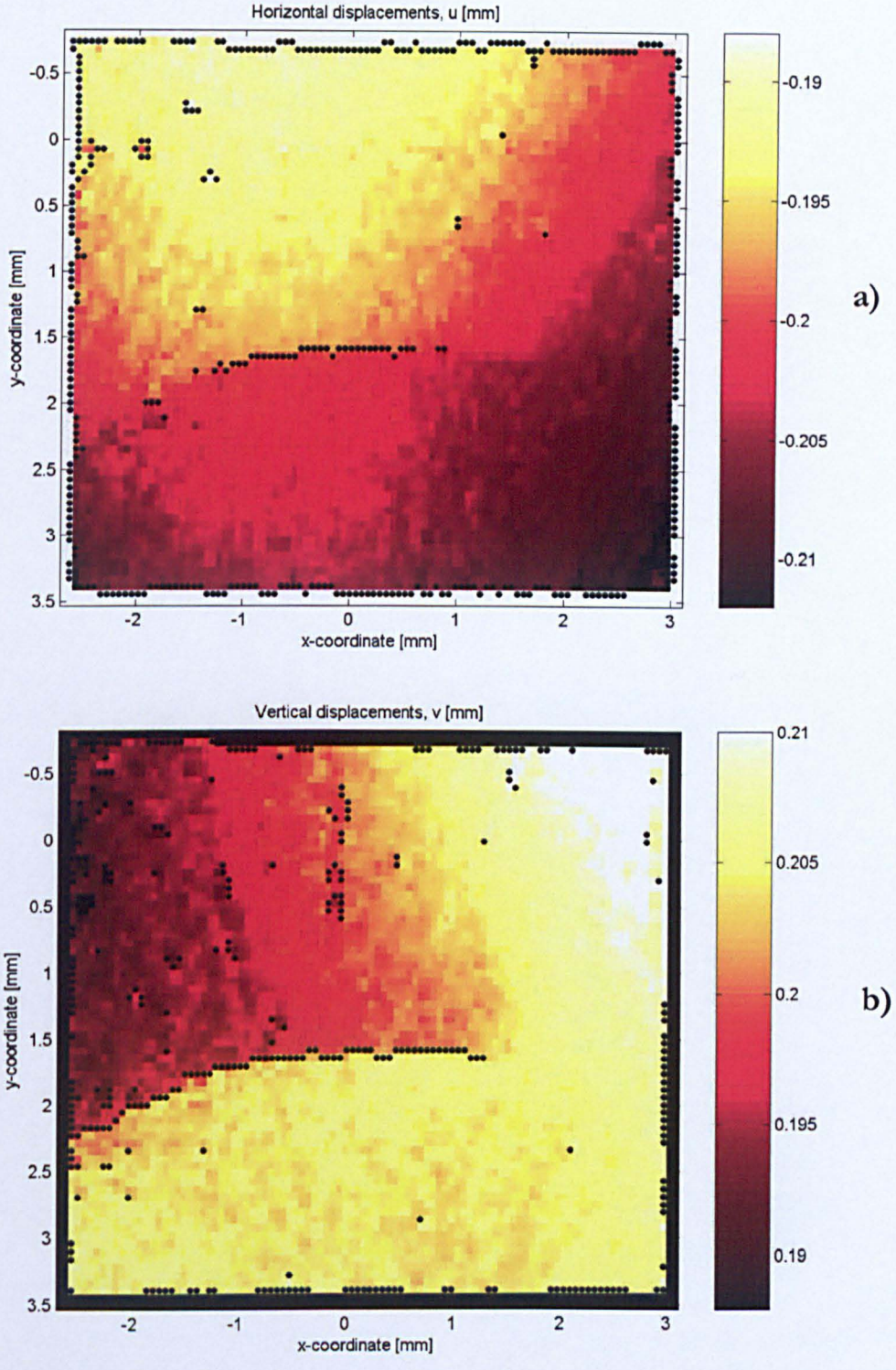

Figure 6.14: Results of applying the edge finding routine on (a) horizontal displacements and (b) vertical displacements, measured on the crack emanating from a hole geometry loaded at θ = 34.6°. The crack tip coordinates, (1.28, 1.64), were extracted from the vertical displacement.

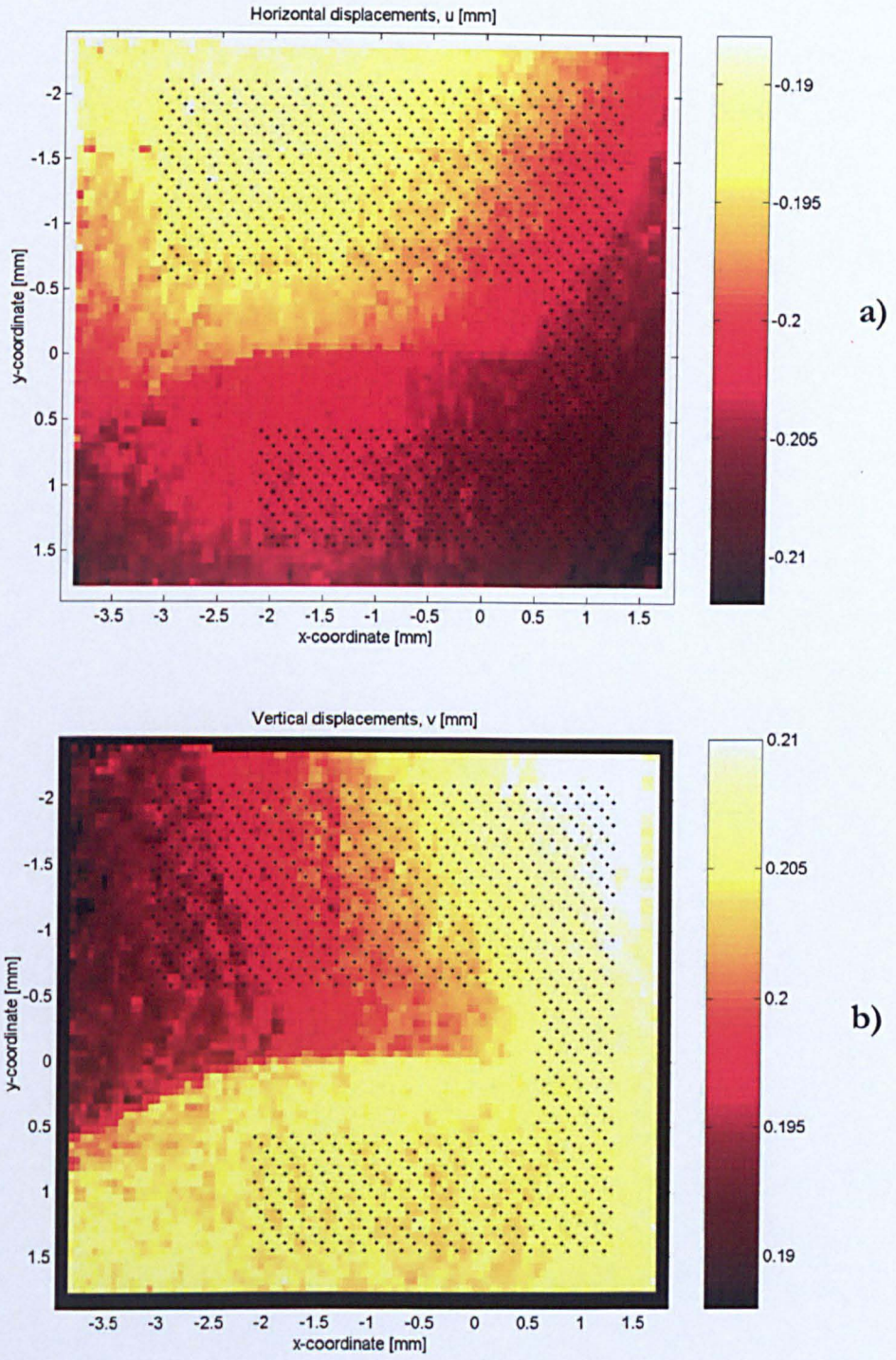

Figure 6.15: Array with approximately 1100 selected displacement points considered for the SIF calculation in (a) horizontal displacements and (b) vertical displacements of a hole-in-a-plate specimen loaded at $\theta = 34.6°$. Note that the origin of coordinates is shifted with respect Figure 6.14, and in the current figure the origin is located at the crack tip. In order not to collect points on the crack, the array was made non-symmetric with respect the axis $y = 0$.

Figure 6.14 illustrates one example of the results of finding the crack by the edge-finding routine on the crack emanating from a hole geometry, for the case of θ = 34.6°. The displacement data points collected for that case are shown in Figure 6.15. The inferred and nominal applied SIFs are presented in Figure 6.16. Errors of the same order are observed in the K_I and K_{II}.

The results obtained for the three different geometries are summarized in one single figure. Figure 6.17 shows the differences between nominal and experimental values, in a normalized scale, against the crack length, a, in the case of the wedge opening loaded specimen, and against the loading angle, θ, in the case of the centre crack panel and the geometry with a crack emanating from a hole. Note the logarithmic scale in the vertical axis.

The stress field investigated in the current section is more complicated than the one in the centre crack plate. In the present case the resulting field is a combination of the crack tip field and the field caused by the stress concentration. By comparing the data of the centre crack panel (CCP) and the crack emanating from a hole (CFH), it can be appreciated that the differences are of the same order in both cases. Therefore the model is able to characterize with approximately the same accuracy simpler stress fields such as that of the centre crack panel, and more complex fields, such as that of the crack emanating from a hole.

Smaller differences appear for the wedge opening loaded data, which, unlike the other two geometries, was uniquely subjected to pure mode I loading. The larger differences in the centre crack panel and crack emanating from a hole could be originated by contact phenomena arising along the wake, as a consequence of mixed-mode loading. Effects such as interlocking of the fracture surface asperities and plastic deformation of the asperities were previously found to alter substantially the crack driving force, when contact and rubbing along the crack wake are important [117, 118]. In addition, residual stresses ahead of the crack tip are likely to be present as no special care was taken while pre-cracking the specimens to minimize its presence [119]. The effect of the aforementioned factors was previously quantified, and involves the obtainment of parameters such as the friction coefficient between the crack flanks, the extent of wear debris or the real displacements along the crack

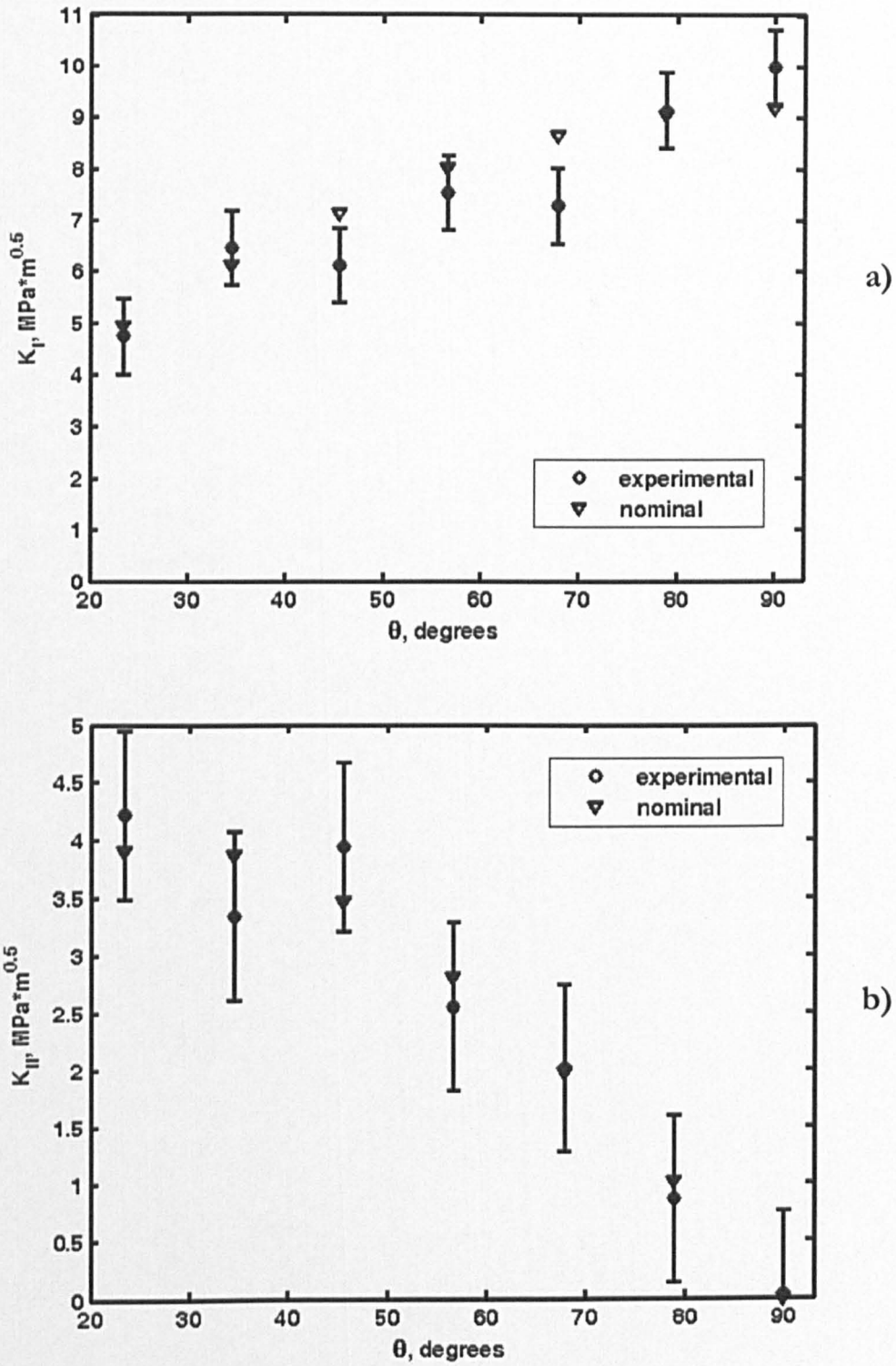

Figure 6.16: Experimental and nominal applied stress intensity factors obtained for the crack emanating from a hole geometry. Several loading cases are presented, with different mode mixity ranging from mixed-mode, $\theta = 23.5°$, to pure mode I, $\theta = 90°$, with 11.1° increments showing (a) K_I and (b) K_{II}. The error bars in the experimental results are also plotted.

flank [115]. However, due to its complexity the evaluation lies beyond the scope of the present work.

As a consequence of the above mentioned phenomena, the nominal values would not describe perfectly the problems investigated, and to some extent the theoretical solutions over-simplify the solution.

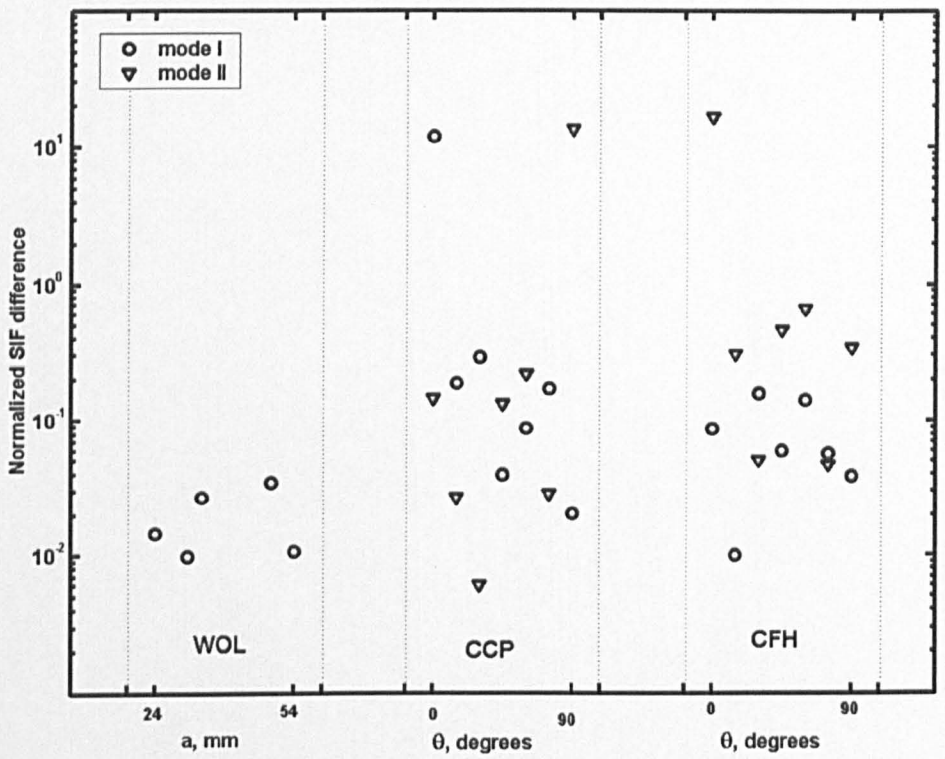

Figure 6.17: Normalized difference of the SIF for the three different geometries, namely wedge opening loaded (WOL), centre crack panel (CCP) and crack emanating from a hole (CFH). In the wedge opening loaded specimen, the normalized difference is plotted against the crack length, a, and in the other two geometries against the loading angle, θ. The length of the fatigue crack in the centre crack panel was 12 mm and in the crack from a hole specimen was 5 mm. Note the logarithmic scale of the vertical axis.

6.8 Monitoring of the SIF

A set of experiments was conducted with the aim of extending the methodology previously developed to the monitoring of the SIF while a cyclic load was applied to

a fatigue crack. A wedge opening loaded specimen with crack length, *a*, of 55 mm was selected.

82 images were captured with the camera during three loading cycles with sinusoidal shape. For each of these images, a displacement field was obtained. These resembled qualitatively the fields shown in Figure 4.15.a. The load was applied with the testing machine shown in Figure 4.7 at 1.1Hz. The camera was set to capture images at a rate of 30 frames per second. This frame rate was achieved by storing temporarily the images in the built-in memory of the camera. Accordingly, around 27 images were acquired during each loading cycle. The same optical setup from section 6.4 was employed. The resolution was also comparable to that achieved in section 6.4.

The crack tip coordinates were determined from an image obtained when the maximum load was applied. The results of the edge finding routine looked similar to those shown in Figure 6.5. Around 1700 displacement data points were collected in the neighbourhood of the crack tip, in an array similar to that presented in Figure 6.6. Both opening mode and sliding mode SIFs were determined. The results comparing the inferred and theoretical SIFs are plotted in Figure 6.18. Good correlation is observed between nominal and measured SIFs. It can be appreciated from Figure 6.18 that in around 90% of the images, the experimental values underestimate the nominally applied SIFs. The differences are of the same order as the data from Table 6.1. The discrepancy becomes more visible in the upper peaks of the plot, being its maximum value 0.64 MPa$\sqrt{m}$, that is an error of 3.2% with respect the maximum theoretical value. Given that the crack was grown under fatigue conditions, this consistent underestimation of the theoretical SIFs could be originated by some degree of closure exhibited by the material. As a consequence, the effective mode I SIF is smaller than the theoretical ΔK_I. Nevertheless, as explained in sections 5.3, 5.4 and 6.5, a substantial part of these errors is likely to be produced by the error in locating the tip of the crack.

It is also observed from Figure 6.18 that the K_{II} values were very close to zero in all the cases, as it should be, since the wedge opening loaded sample allows only pure mode I load to be nominally applied. Possibly the poor signal to noise ratio for the mode II component was the cause of the values oscillating around zero.

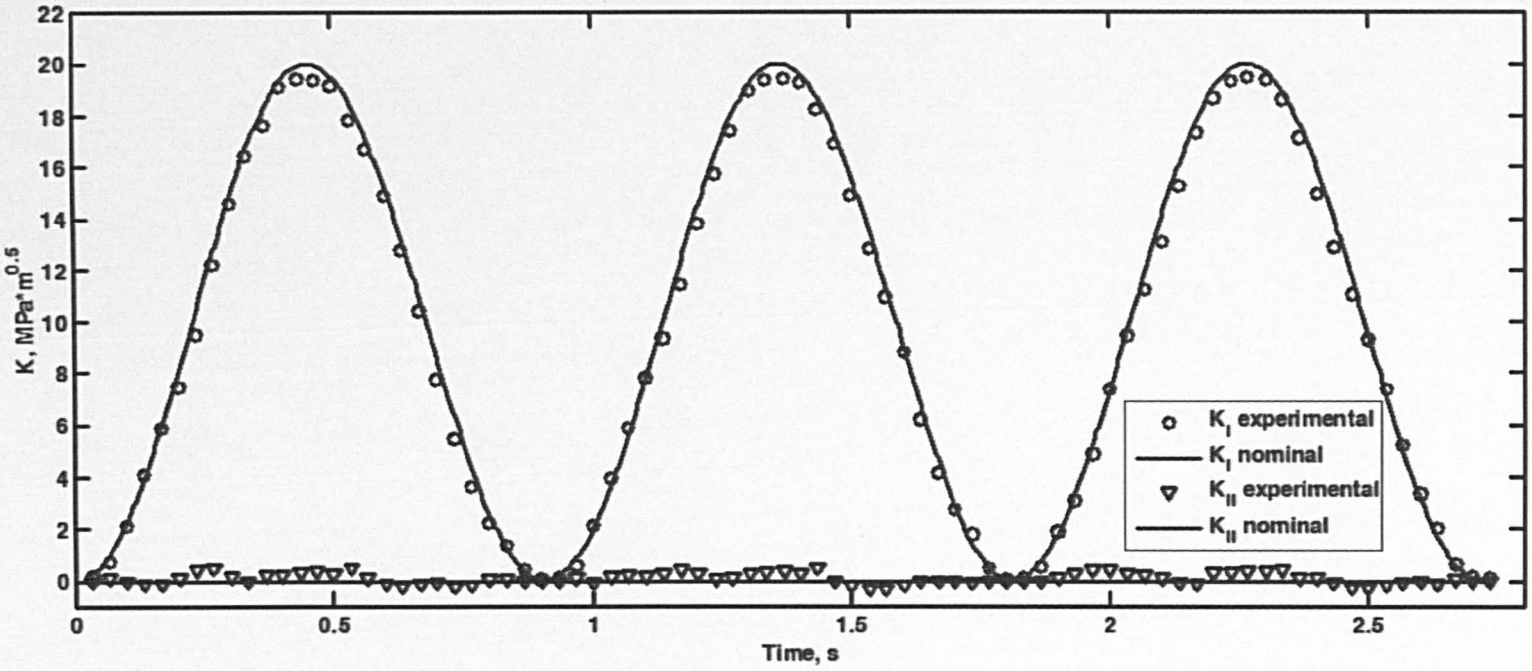

Figure 6.18: Inferred and nominal applied K_I and K_{II} monitored during 3 loading cycles in a wedge opening loaded specimen.

6.9 Conclusions

The results of applying a methodology to SIF evaluation from image correlation displacement data were presented.

The selection of the experimental data points employed is justified by comparing it with data points collected previously in other experimental techniques which inspired the development of the methodology herein presented.

The approach for inferring the SIF from displacements measured with image correlation was applied to increasingly more complicated geometries, namely wedge opening loaded sample, angled centre crack panel and plate with a centred hole and an inclined crack emanating from the hole.

Based on the results obtained for the wedge opening loaded specimens, an attempt to quantify the uncertainty of the results was done, and the error bars for the SIF determination were estimated.

The performance of the developed tool for different crack lengths was assessed for pure mode I loading. Subsequently the methodology was applied to different mixed mode (I + II) cases. The best agreement between theory and experiments was obtained for the pure mode I sample. Although not as good as for the pure opening mode case, an overall good agreement was found when mixed mode loads were involved.

It is believed that, besides the uncertainty of the technique, two main reasons are the possible source of the discrepancies between nominal and experimental values. On the one hand, the assumption made in the analytical developments of the elastic model of the crack being a traction-free would not be completely correct, as some contact points occur along the wake, due to the irregular shape characteristic of fatigue cracks. On the other hand, the nominal values do not take into account irregularities such as existence of contact along the crack wake; effects introduced by the fact that the samples were fatigue pre-cracked under pure mode I loading, and these same samples were tested under mixed mode (I + II) conditions; and the fact that the crack tip front was not precisely perpendicular to the surface studied. All these factors made the experiments deviate from the ideal conditions for which theoretical solutions [107] were obtained.

The results obtained for different crack lengths on wedge opening loaded specimens suggest that the crack length has little or no influence on the experimental SIF, for pure mode I conditions. In addition, those data indicate that the error seems to be load-independent. Consequently the relative influence of the error will be larger at low SIF ranges (in our studies below 4 MPa$\sqrt{m}$) than at higher ranges.

Finally the methodology was also applied to monitor the SIF while a cyclic load was applied to a wedge opening loaded specimen. An excellent agreement between theory and experiments is observed in both opening mode and sliding mode SIF. In addition, the fact that the inferred ΔK_I underestimates consistently the nominal applied value could be interpreted as existence of closure. A more detailed discussion on this subject will follow in the next chapter.

Chapter 7

Experimental evaluation of fatigue crack closure

7.1 Introduction

While conducting the experiments to determine pure opening mode SIFs and mixed-mode SIFs, it was noticed that in some cases the inferred SIFs were consistently smaller than the nominally applied ones. This experience and the fact and that the aluminium alloys tested are likely to exhibit closure [58, 85, 120, 121], led the author to consider the presence of closure effects which would cause the crack to remain closed in the initial loading phase, yielding as a result SIFs considerably lower than the nominally applied. The present chapter explains the experiments conducted in order to explore this effect, and the results associated with these experiments.

7.2 Closure effects observed from the opening mode SIF

The same centre crack plate described in Chapter 4 was fatigue pre-cracked for 100000 cycles at 10 Hz, under pure mode I loading, with R = 0.1 and ΔK = 10 MPa$\sqrt{m}$. In all the analyses carried out in this part of the study, the specimen was subjected to the load arising from using the grips from Figure 4.2 with θ =30°. Accordingly mixed-mode (I + II) conditions were studied, the sliding mode component of the load being predominant (K_{II}/K_I = 1.73).

The first set of experiments consisted of applying different cycles with the same nominal SIF range (ΔK = 4.34 MPa$\sqrt{m}$), but varying the load ratio, R. Seven

different ratios were applied to the same specimen, ranging from 0.09 to 0.35. For each ratio a pair of images were taken in order to apply the correlation algorithm. The first image was captured at the minimum load of the cycle and the second one at the peak of the cycle. As a result, a displacement field was obtained, containing information related to the horizontal and vertical displacement fields occurring in the neighbourhood of the crack tip. These displacement data were analyzed following the procedure described earlier. The edge-finding routine results and the array employed were very similar to these shown in Figures 6.11 and 6.12.

The results plotted in Figure 7.1 show the evolution of the opening mode SIF range with increasing R ratios. It can be seen that for the range of load ratios considered, all the experimental SIFs lie below the nominal values. For the smallest load ratio examined, the inferred SIF range was approximately one half of the expected one from theory. Nevertheless it is also noticed that the experimental ΔK_I tends to the nominal one with increasing load ratio, the minimum difference between inferred and theoretical values being 0.19 MPa$\sqrt{m}$.

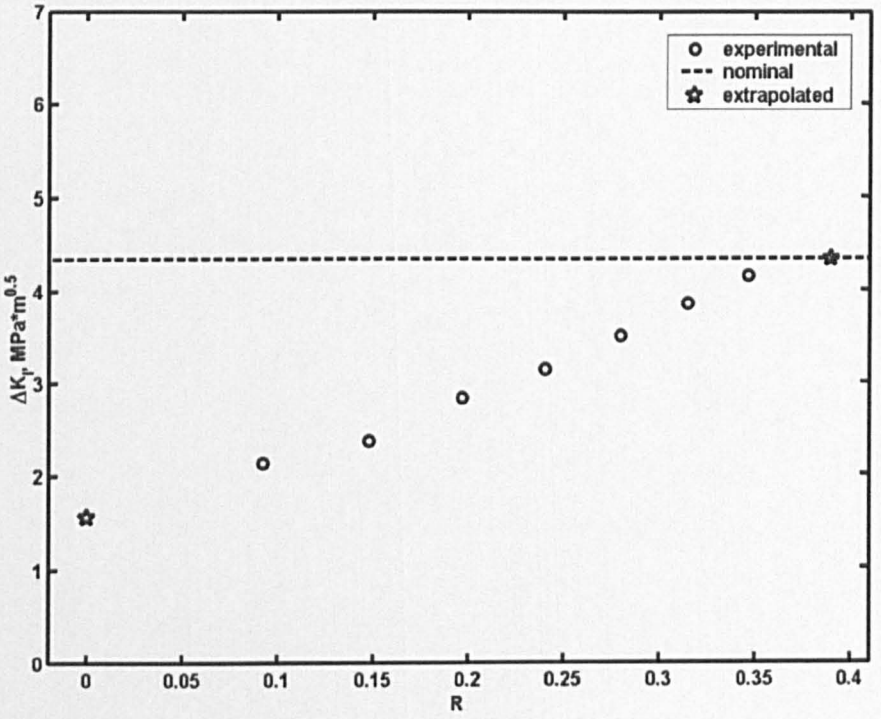

Figure 7.1: Variation of the mode I SIF range with increasing load ratios, R. The nominal SIF range is shown in a dotted line. Two extrapolated points taking into account the opening SIF range measured in Figure 7.2 are also drawn.

The fact that the closure effects can be obscured by increasing load ratios has been observed since Elber's discovery of closure [see for example 59, 43, 120 or 121]. Accordingly, the relation found herein between SIF range and the load ratio seems to agree with the literature, and it seems logical to explain this phenomenon as the consequence of crack closure. Therefore, the type of result presented in Figure 7.1 can be used to obtain some qualitative information regarding the crack closure. However, it does not allow these effects to be evaluated easily or quantitatively. In order to not only detect the phenomena but also to obtain precise measurements of closure levels, another experiment was carried out. This was performed with the same specimen subjected to the same degree of mixed-mode, with the aim of monitoring the SIF in a way similar to section 6.8.

In order to detect deviations from the nominal SIFs as clearly as possible, instead of applying the load following a sine function, as was the case in section 6.8, the shape of the load wave was triangular. Sixteen images were recorded during the loading part of the cycle, being the first of them captured at zero load. By comparing each of the rest fifteen images with the image taken at zero load and following the procedure described in previous chapters, a value of the SIF was calculated for each of those fifteen images. The results showing the opening mode evolution through the loading part of the cycle appear in Figure 7.2.

The experimental K_I data show clearly two regions. A first one, for loads up to approximately 5.5 kN where a very small increase in K_I is observed as the load is raised. The second region shows a considerable change in slope, and the SIF values clearly increase with the load. The main change in the slope occurs around the sixth experimental point in the plot. At this point the slope changes quite drastically from a very small value to a value comparable to the slope of the theoretical SIF, most likely due to crack closure. Accordingly, the experimental SIF would represent the effective SIF which is perceived by the crack.

Throughout all the applied loads, the effective SIF is substantially smaller than the nominally applied. For the maximum load applied to the sample the experimental SIF was approximately 30% lower than the maximum nominal SIF.

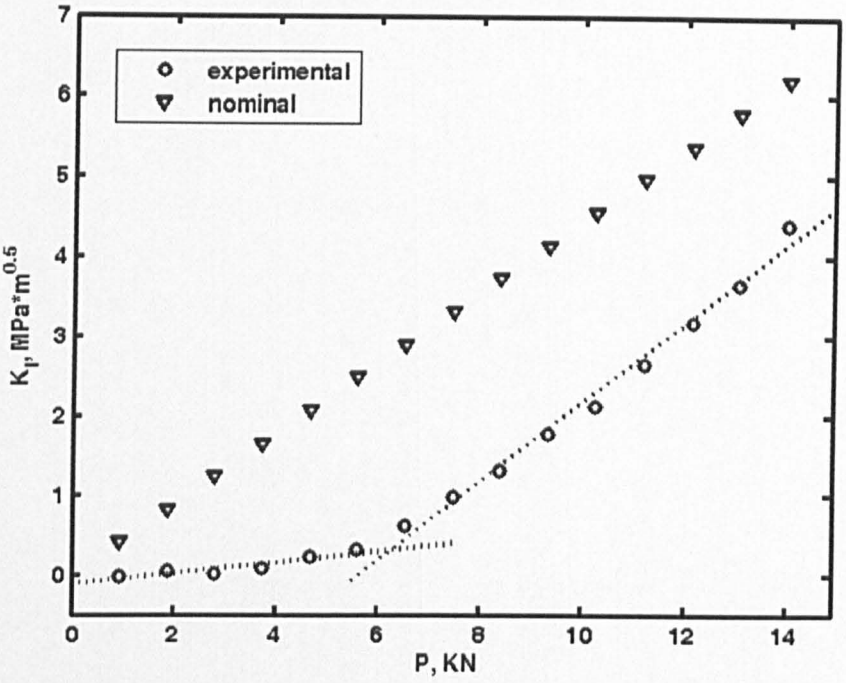

Figure 7.2: Opening mode SIF measured during the loading portion of a fatigue cycle. The nominal values were calculated assuming that no closure was present in the sample. Two best-fitted lines are also plotted. One of them fits the first six points and the other the remaining points of the experimental data.

For estimating the fatigue crack opening load, a similar method to the intersection of the two tangent lines [85] was employed. This was initially developed for load – COD plots. However, in the present work the ΔK_I data are plotted against load. In addition, both upper and lower extremes of the ΔK_I – load plot are slightly curved. As a consequence, if the tangents are drawn from the first and last points of the inferred values from Figure 7.2, the intersection point of both tangents will not be a good indication of the opening load. For this reason the approach to estimate the opening load consisted of fitting a line to the initial first few data of the plot and another line to the data in the second region aforementioned, where a clear relation is observed between load and K_I. The first 6 points were considered to lie within the first region and the last 9 points within the second region. Hence the best fit lines obtained by least-square linear regression are also shown in Figure 7.2. The intersection of these lines will indicate the moment at which opening of the crack occurs. Accordingly the measured opening load is 6.29 kN. The opening point can be

predicted also in terms of SIF by projecting vertically the intersection point to the curve of the theoretical SIF, and can be named opening SIF, K_{op}. The K_{op} found in this way is 2.78 MPa$\sqrt{m}$. That is, almost 45% of the maximum nominal SIF.

In the second region aforementioned, the experimental SIF follows a trend almost parallel to the theoretical SIF. Due to the small slope of the curve in the initial portion of the experimental data, compared to the slope of the nominal values, although the data in the second region agrees quite well with the theory, the gap observed between both trends is probably caused by the initial delay produced in the first region. In addition, it can be also noticed that the last section converges slightly towards the theoretical values. This could be interpreted as a second increase in compliance, possibly yielded by plastic deformation and crack growth. Nevertheless, as only the last point seems to follow this trend, a higher load should be applied in order to determine if this increase in compliance is actually occurring or the increase in slope is only due to experimental error.

In order to detect automatically the change in slope of the experimental data of Figure 7.1, the curve was differentiated numerically, employing two points. Different approaches were employed, namely using two successive points, two alternate points separated by a distance of 2 kN and two alternate points separated by a distance of 3 kN. Nevertheless in none of the cases the change in slope could be visualized clearly. As a consequence, this differentiation did not help to detect automatically the change in the slope of the curve.

A further verification can be done by extrapolating some data in Figure 7.1, based on the information extracted from Figure 7.2. For the case assuming that the cycle begins at zero load (i.e. R = 0), the corresponding ΔK_I, taking into account the opening SIF would be:

$$\Delta K_I = \Delta K_{max} - \Delta K_{op} = 4.34 - 2.78 = 1.56 \tag{7.1}$$

Likewise it is also possible to extrapolate the point for which the sample would show no closure. By making the minimum load of the cycle fit with the opening SIF, no closure would be expected in the experiment conducted for plotting Figure 7.1. That is, if the same SIF range from Figure 7.1 is used, and the minimum SIF equals 2.78 MPa$\sqrt{m}$, the resulting load ratio is:

$$R = \frac{\Delta K_{op}}{\Delta K_{max}} = \frac{2.78}{2.78 + 4.34} = 0.39 \qquad (7.2)$$

Both extrapolated points are shown in Figure 7.1 as stars. It is observed that the two points fit well with the trend followed by the experimental data of Figure 7.1.

When analyzing compliance traces, previous approaches for characterizing closure levels differed in some cases, depending on the position of the strain gauges [78]. In the current approach many displacement data points were collected in the neighbourhood of the crack (see Figure 6.12), and all this information was taken into account for evaluating the effective SIF. As a consequence the closure level measured in this work may be considered as a sort of average between all the displacements occurring around the crack, thus including the influence from the crack wake.

7.3 Closure effects observed from the sliding mode SIF

The sliding mode SIF was also determined in the loading portion of a cycle. The results were extracted simultaneously with the opening mode SIFs, from the same experimental images. Analogous to the case of opening mode, Figure 7.3 presents the results of the mode II component of the SIF.

It can be seen from Figure 7.3 that the inferred K_{II} values follow roughly the same trend that the K_I ones, in the sense that for lower P values the experimental SIFs are smaller than the theoretical ones, while for higher levels of load the experimental values correlate better with those predicted by elastic theory. Nevertheless, while in the first portion of the loading phase no significant increment was observed in K_I, in the case of K_{II} substantial increment is appreciated in the initial part of the plot.

A certain similitude between the calculated K_I and K_{II} plots is also detected by looking at the slope of the imaginary curve which links the experimental points. This slope evolves from a low value, smaller than those of the theoretical trend, for ΔP smaller than 4 kN, up to values comparable to the theoretical imaginary line, for ΔP of around 13 kN.

It is also noticed that the point related to the minimum load is very close to zero (-0.13 MPa$\sqrt{m}$) while the theoretical SIF is 1.12 MPa$\sqrt{m}$. The fact that the sign of this first point is negative is attributed to experimental error, as no motion is

expected in the negative shear direction. It is believed that the displacements around the crack at this point are very close to zero, and as a consequence, the very poor signal to noise ratio could yield a negative value. In any case the first point lies within the trend of the rest of the experimental points and a very small value for low loads can be interpreted as being a consequence of the closure.

In addition, other effect of the closure on the trend followed by the experimental ΔK_{II} results is probably the deviation from the theory which occurs for load ranges smaller than 10 kN.

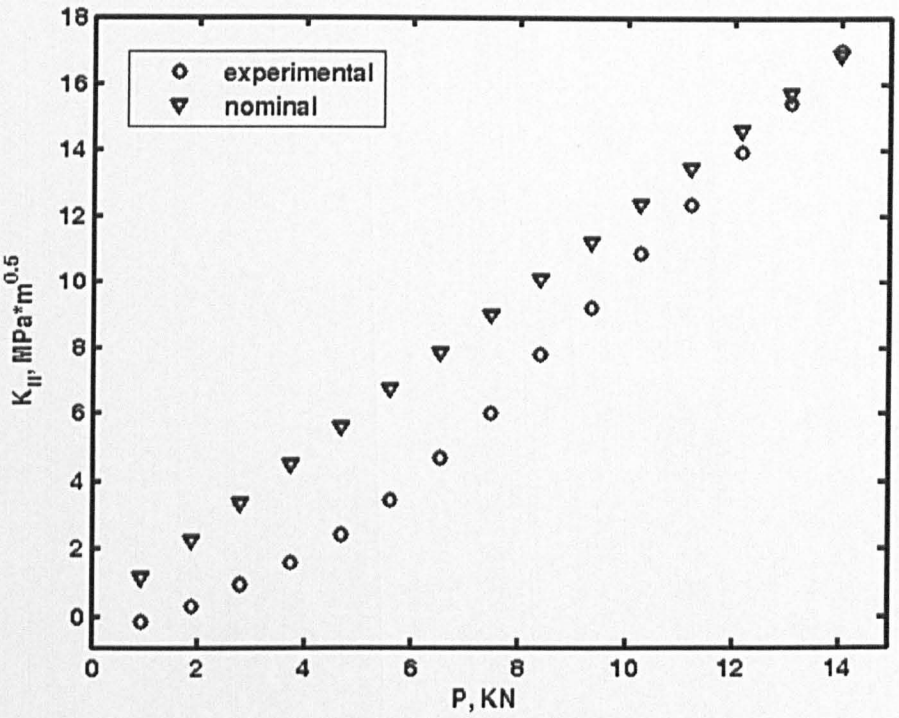

Figure 7.3: Sliding mode SIF measured during the loading portion of a fatigue cycle. The nominal values were calculated assuming that no closure was present in the sample.

7.4 General comments

The difficulty associated with the interpretation of the compliance traces is recognized [78 and 122]. The proposed approach for evaluating the closure level is also affected by some degree of subjectivity, since it can depend on judgement to decide which points of the plot lie within the first and the second region described in section 7.2.

The closure knee typically observed in fatigue appears very clearly in the case of ΔK_I, even though the sliding component of the load is almost three times bigger than the opening one. The behaviour of the ΔK_{II} trend seems also to be affected by the closure, but in a different manner, since although the closure knee is present, the change in slope is smoother. For this reason it was not possible to use a simple procedure to extract quantitative readings of closure level from the mode II SIF range. Therefore, the experimental results obtained for ΔK_{II} could be utilized for detection of closure effects in a body. Nevertheless in order to obtain accurate measurements of the opening point from the sliding component of the SIF, a more developed methodology than the one presented in section 7.2 should be employed.
The effects detected could be caused by plasticity- and roughness-induced crack closure. The plasticity-induced closure is expected since the crack was grown at low R ratios and low ΔK's [59] and the material investigated often exhibits plasticity-induced closure [120, 121]. The roughness-induced crack closure may also be present in the crack due to the irregular shape of the crack flanks and the high level of sliding mode applied [62 and 115].

7.5 Conclusions

The methodology described in the preceding chapter for evaluating the effective SIF range was applied to a 7010 aluminium alloy centre crack plate. The sample was previously fatigue pre-cracked at low load ratios.
It was found that the effective SIF range evolves from values of approximately half of the theoretical SIF when cycles with low load ratios were applied, to values close to the nominal SIF, with increasing R ratios.
Subsequently the technique developed in Chapter 6 for SIF monitoring was applied to the same specimen, subjected to mixed mode (I + II) conditions. The results obtained for the opening mode SIF range show clearly the existence of closure. Moreover, accurate measurements of the ΔK_{eff} can be taken for different load ranges, making it possible to obtain the opening point. The sliding mode SIF deviates also from the nominal values predicted by elastic theory. It is believed that this deviation

is also a consequence of the crack closure. A simple approach for evaluating quantitatively closure levels was described.

In summary the present chapter demonstrates the ability of the methodology to extract effective values of the SIF and its sensitivity to closure effect.

Chapter 8

Discussion

8.1 Discussion

Both linear elastic (SIF) or non-linear parameters (J-integral, CTOD, CTOA) are employed in the characterization of cracks. In the present work the SIF is utilized to describe the fields associated with fatigue cracks. Accordingly the elastic field is assumed to be dominant over the HRR or high strain fields.

In the last decade image correlation technique has become more widely used by the experimental mechanics community due to its clear advantages over other experimental techniques. It requires little or no surface preparation, does not need anything to be bonded to the surface, and is not restricted to any type of loading regime [110]. Moreover it is very cheap and relatively easy to apply compared with other stress analysis techniques. For these reasons it was selected to characterize fatigue cracks in the present work.

In 1993 a methodology was developed to infer the mixed-mode (I + II) SIF from experimental data, combining a very general methodology, based on Muskhelishvili's complex variable formulation [12] with photoelastic information of the stresses [26]. Both experimental data and elastic solution were combined by using the MPOD method [21]. The approach was then extended to thermoelastic stress analysis [42]. Both procedures were found to be sensitive to closure phenomena [43, 29]. The present study is a logical continuation of the above works, aimed at developing a similar methodology but taking advantage of the relatively new technique of image correlation. Given that the raw data provided by image correlation is not stress-based, but displacement information, a methodology based on Muskhelishvili's

approach was developed for relating displacement fields to the opening and sliding mode SIFs directly.

The methodology consisted of solving a series of coefficients from a system of equations containing information about the two Muskhelishvili's analytical functions, φ and ψ. Subsequently the mixed-mode SIF was related to the coefficients [105].

The stability of the system of equations was studied by evaluating the condition number of the system in different simulations. The condition number was computed with the help of the Singular Value Decomposition [104]. It was found that the stability increases by taking more data points and fewer terms in the series developments. In addition, in order to assure good stability [116], it was recommended that for 15 values of displacement, up to 5 terms in the series should be employed, and more than 500 data points would be required for 7 terms.

Subsequently the method was verified with artificial displacement data simulating a centre crack in an infinite panel subjected to uniform load applied at infinity. The artificial data were generated according to Westergaard's solution. The combination of a shape parameter, m, of 0.995, and a series limit, M, of 100 provided SIF errors better than 0.05%. These small errors are probably caused by the accumulation of rounding errors in the sums involving many terms [106] such as those in equations (3.30) to (3.33).

In this work the methodology was applied to determine the SIF. Nevertheless as it relates the displacements from the surface to the two analytical functions from Muskhelishvili's formulation, it could be easily employed for a broader class of problems, such as reconstructing the full elastic solution which can then be used for stress concentration analyses.

An attempt to calculate the SIF by using an optimization method previously applied in thermoelasticity [43] and photoelasticity [29] was made. The optimization method was based on genetic algorithms. The elastic model was very similar in both thermoelastic and photoelastic works, as both techniques are stress-based. In the present case, the model was based on Muskhelishvili's formulation as in the other works, but unlike them, it was developed in terms of displacements rather than stresses. For the current model, it was found that iterative methods based on genetic algorithms were computationally too expensive for solving the non-linear system of

equations arising from including the crack tip coordinates as unknowns. It is believed that the large number of function evaluations and the very slow convergence of the method are consequences of the system being highly non-linear [112]. For this reason a different approach was developed for solving the problem. It consisted of applying a Sobel edge-finding routine developed for image processing purposes [113, 114] to the displacement field measured around the crack. The routine was utilized for locating the coordinates of the crack tip as a previous step before solving the system of equations. In doing so, the system becomes linear and could be solved in a least-squares sense in few seconds with high accuracy. QR decomposition [103] was selected for carrying out this operation. Furthermore the error produced in the SIF as a consequence of locating the crack tip by the Sobel edge-finding routine was assessed by means of a sensitivity analysis. The proposed approach was found to provide satisfactory results in terms of SIF error. As a consequence of having an uncertainty of 60 μm, average errors of less than 1.9% and 1.2% in the opening mode and shear mode SIF respectively were determined. Nevertheless, it was also found that the edge-finding routine did not provide acceptable results for SIFs smaller than 3 MPa$\sqrt{m}$. In addition, the methodology was the fastest one among the different methodologies studied, being the processing time of the order of a few minutes.

The methodology was then applied to calculate the effective opening mode and the sliding mode SIF from image correlation data in three different geometries for which theoretical solutions were available [107]. The first geometry, the wedge opening loaded specimen, allowed only pure mode I load to be nominally applied. The centre crack panel was the second geometry tested, and by means of special grips designed by Otsuka et al. [108] allowed seven different mixed-modes to be applied, ranging from pure mode I to pure mode II. The last type of geometry investigated was the plate with a centred hole and a crack emanating from the hole. This specimen has more industrial relevance for its resemblance to fastener holes which are extensively used in aircraft structures. This last geometry was also subjected to mixed mode loading, from pure mode I loading to a K_{II}/K_I ratio of 0.89.

In previous works where the SIFs were inferred based on image correlation data, the experiments were conducted on artificially generated slits, with tip radius of at least

0.25 mm [51, 56]. By doing so, many factors which are present in real cracked components and do have an impact on the effective SIF were eliminated. For this reason in this work all the specimens were fatigue pre-cracked before the tests were conducted.

The number of points employed in the MPOD method was selected based on previous work using different experimental techniques [47, 26, 42]. It was shown that by increasing the number of data points so that the system of equations was massively over-determined, the effect of noise was minimized and the system became more stable. Moreover, the better signal to noise ratio in areas behind the crack tip motivated the collection of data points not only ahead of the crack tip, as is typical in photoelasticity and thermoelasticity, but also behind the crack tip. Accordingly a rectangular shape array was utilized, approximately centred in the crack tip.

The results obtained for the wedge opening loaded specimens were employed for estimating the uncertainty of the technique. The error bars were found to be $\pm$ 0.73 MPa$\sqrt{m}$ with 95% confidence, the location of the crack tip being the main source of contribution to these errors bars. This agreed well with previous work [21, 43, 47, 56] where the position of the tip of the crack was found to be the largest source of uncertainty. Moreover, the uncertainty improved slightly (reduction of 2.1%) compared with previous work [55] which calculated the SIF from image correlation data.

The performance of the methodology was assessed for different crack lengths in the wedge opening loaded specimen. No influence was observed of the crack length on the accuracy of the method.

The quality of the least-square fitting was evaluated by means of the relative residual [116], which measures the discrepancy between the constructed displacement field and the actual displacement field measured with image correlation. In all the cases the values were very small (of the order of 10^{-3} %), thus indicating that the number of terms employed in the series provided the model with enough flexibility to adapt itself to the experimental field. As a consequence, no substantial improvement would be achieved by increasing the number of terms in the series. However the stability of the system would be considerably reduced.

Very good correlation between theory and experiments was found in the wedge opening specimen, with K_I differences being consistently smaller than 5%. In some of the cases a small sliding mode component was measured, probably due to local mixed-mode occurring at the crack tip as a consequence of the roughness of the crack flanks (Figure 6.10). The differences between nominal values and experimental ones were approximately the same irrespectively of the absolute value of the load. Accordingly larger errors resulted when very small loads (giving SIFs less than 4 MPa$\sqrt{m}$) were applied.

In the cases of the angled centre crack panel and plate with a centred hole and an inclined crack emanating from the hole, the theoretical mixed-mode SIFs agreed well with the measured ones, and about the same differences were detected in both the opening and the sliding mode SIF. Nevertheless, as Figure 6.17 shows, the results for the mixed-mode geometries were overall more scattered than the wedge opening loaded ones. In these two geometries, a number of factors became more important due to the presence of a sliding component in the load, and made the differences between the experimental and the theoretical values larger. These include interlocking of fracture surface asperities and plastic deformation of the interlocking asperities [118] as a consequence of crack face contact and rubbing, and sliding crack displacements associated with the irregular shape of the fatigue crack. Moreover compressive residual stress ahead of the crack tip is likely to be present as no special care was taken during the pre-crack process to avoid its presence [119]. It is known that these factors can modify substantially the crack driving force [117] and their effects have been previously quantified [115]. Nevertheless its evaluation is not straightforward and lies beyond the scope of the present work. It involves obtaining relevant parameters such as the friction coefficient between the crack flanks, the extent of wear debris or the real displacements along the crack flanks which, in the case of image correlation data are very noisy due to the discontinuity generated at the crack.

In addition the effect of the crack being grown under mode I loads and then tested in different mixed-mode conditions decreased the matching between the serrated faces of the crack, compared with when only mode I load was applied [62], thus

creating additional contact points along the crack wake and promoting the crack to be wedged open at discrete contact points along the crack faces [115].

Furthermore, in the case of the crack emanating from a hole, the crack growth was not straight, i.e. 5.25 mm on one side and 4.70 mm on the other side, and the fatigue crack was not straight either, having a distinct curvature in the initial part (see Figure 4.5.d). The displacement fields were captured in a rectangular area centred at the crack tip, and therefore contained information about all these factors.

Two main reasons were thought to make the difference between theory and experiments larger in the mixed-mode geometries than in the pure mode I geometry. On the one hand the assumption of the crack as a traction-free contour made in the linear elastic model is not entirely fulfilled with the existence of contact points along the crack wake. On the other hand the aforementioned irregularities are not taken into account by the theoretical solutions, which assume ideal elastic conditions. Accordingly, the methodology would yield effective values of the crack driving force, but would include a small error arising from the contravention of the boundary condition at a few points in the crack flanks. No attempt was found in the literature to quantify the effect of satisfying partially the traction-free boundary condition in some points of the crack contour. Due to the complexity of the expressions involved, its evaluation lies out of the scope of the present work. Nevertheless, it is believed that its effect is small, as indicated by the good agreement between the values obtained and the theoretical values. The main source of discrepancy between nominal and experimental values is consider to be due to that fact that the theoretical solutions herein employed [107] did not describe the situation perfectly and, to some extent, they over-simplified the problem.

It was noticed that the proposed approach was able to generate satisfactory results even for a fatigue crack emanating from a hole geometry, where complex non-uniform passing stress fields were present.

Another set of experiments was conducted with the aim of monitoring the SIF through several fatigue cycles in a wedge opening loaded sample. The image correlation technique allowed a series of images to be captured while low frequency load with sine-wave shape was applied to the specimen. The same procedure employed for extracting the SIF in static experiments was repeated for each image so

that the SIF was evaluated around 27 times in each cycle. Good correlation was found between the nominal and the experimental SIFs, with the differences being of the same order as those measured in the pure mode I static experiments. The largest difference in the opening mode SIF was detected at the peak of the cycle and was 3.2%. It was also observed that the experimental ΔK_I was consistently lower than the theoretical values. Taking into account the fatigue behaviour of the aluminium alloy tested [120, 121], part of this lower value could be caused by some degree of closure exhibited by the material. Nevertheless these differences between theory and experiments were within the accuracy of the technique. For this reason, a final set of experiments was conducted to explore the sensitivity of the technique to closure effects.

The results for the monitored mode II SIF were always close to zero, as expected, since the test was performed under nominally pure mode I conditions.

Most of the crack closure studies are based on analysis of specimen compliance and fatigue crack growth rate measurements [122]. Nevertheless full-field experimental stress analysis techniques are starting to be applied to the characterization of crack closure [29, 43 and 71]. The experiments herein reported lie within this group, since the technique of image correlation was applied to the analysis of crack closure.

Two experiments were conducted to determine whether image correlation was able to detect the existence of closure and whether it was capable of quantifying the magnitude of the closure. Both experiments were performed on a centre crack panel, previously fatigue pre-cracked for about 100000 cycles at 10 Hz, under mode I loading, with a SIF range, ΔK, of 10 MPa$\sqrt{m}$ and a load ratio of, R, of 0.1. The length of the crack wake grown under these conditions was 12 mm. The two experiments were conducted under mixed-mode loads ($K_{II}/K_I = 1.73$).

The first experiment consisted of applying seven different load cycles to a centre crack panel. The load range was kept constant in all the cycles, while R was increased from 0.09 up to 0.35. The mode I ΔK was evaluated experimentally for each cycle. In all the cases the experimental ΔK values were lower than the nominally applied. In addition the experimental values tended towards the nominal ones as the load ratio was increased. The difference between theory and experiments was explained with the existence of crack closure, which can be visualized more clearly at low ratios [59,

43, 120 and 121]. Moreover, the results were qualitatively very similar to those obtained by Díaz et al. [43], where the SIF was evaluated experimentally by mean of thermoelastic stress analysis, also for a range of different load ratios. Nevertheless direct comparison of the results could not be made due to the experimental differences between the two investigations. Therefore, this experiment demonstrated the sensitivity of the technique to closure phenomena.

The second experiment was aimed at not only detecting crack closure, but also at providing a quantitative measure of the level of closure. It consisted of monitoring the mixed-mode SIF through the loading phase of one cycle. Fifteen images were collected while the load was applied, and the SIF was evaluated for each of the acquired images. The crack tip position was deduced from the image captured at maximum load, providing the best signal to noise ratio.

In all the cases the experimental SIFs were below the theoretical ones. At maximum load, the experimental mode I SIF was 30% lower than the nominal SIF. Furthermore, the plot of the experimental ΔK_I showed clearly two regions. Initially, for loads up to around 5.5 kN, the slope of the experimental curve was considerably lower than the theoretical one. At approximately 5.5 kN load the slope changed markedly and adopted values very close to the slope of the theoretical curve. In other words, the experimental points of the ΔK_I described the closure knee typically observed in closure studies [59]. The results resembled those obtained by Pacey et al. with photoelasticity [29]. Nevertheless, while in image correlation the displacement measures are found by comparing with an initial stage (normally the undeformed image), photoelasticity provides data independent of previous states. For that reason, in the current work, the curve of the experimental data appeared translated vertically and downwards if compared with the results obtained by Pacey et al. Moreover in the present study, the number of data captured in the loading phase of the cycle was increased, and consequently the plot was approximately twice as denser than in [29]. This allowed characterizing with higher precision the opening point.

The estimation of the opening point was done based on a procedure previously developed for COD – plots [85]. Nevertheless certain modifications were introduced to adapt it to the type of data herein obtained. By fitting two straight lines to the two regions existing in the ΔK_I – load plot, an intersection point was obtained (see Figure

7.2). The opening load was identified as the value corresponding to the intersection read on the load axis. Furthermore, the vertical projection of the intersection point with the theoretical curve gave an estimation of the opening SIF.

Even though the second region of the experimental curve was approximately parallel to the theoretical curve, the values were noticeably below the nominal ones. This was due to the low value of the slope in the initial part of the plot. In addition, it was appreciated that the last point of the experimental curve converged slightly towards the nominal data. It was suggested that this fact could be originated by a second increase of the compliance, which has been previously attributed to plastic deformation and crack growth [60]. Nevertheless, given that only one point showed that trend, and the variation was within the accuracy of the technique, it could not be assured whether the convergence perceived in the very last part of the experimental curve was produced by plastic deformation and crack growth or whether it was a variation due to experimental error.

Based on the opening SIF inferred from the second closure experiment, a further verification was done. This consisted of extrapolating the ΔK_I values that would result at load ratios lower (R = 0) and higher (R = 0.39) than those tested in the first closure experiment. The first point was extrapolated considering the crack remaining closed from zero load up to the opening load. The second point was extrapolated at the load such that closure effects could not be visualized, i.e. setting the minimum load equal the opening load. Both points agreed well with the trend shown by the experimental data. Therefore the estimations made based on the second experiment are consistent with the data presented in the first experiment.

Similarly to compliance based methods [78, 122], at present, the proposed procedure is affected by some degree of subjectivity, since judgement is required to assign points to the first or second regions discussed above.

The mode II SIF was monitored simultaneously with the mode I SIF. Analogously to the ΔK_I data, very similar values in the experimental and theoretical slopes were observed at high loads, the greater differences in slope being at low loads. By contrast, in the case of the sliding SIF the transition between both regions was much smoother than in the opening SIF. The closure knee was noticed in the ΔK_{II} data, but appeared less sharp than in the mode I data, even though the load was

predominantly shear. For this reason it is believed that the sliding component of the SIF could also be used to detect deviations caused by crack closure. In order to obtain accurate measurements, the opening component of the SIF should be analyzed.

Since the SIF was inferred using a single crack tip position, deduced from the image captured at maximum load, the error associated with the location of the crack tip was the same in all the points. Accordingly, the uncertainty of the shape of the curve was smaller than the uncertainty of the technique. In other words, the 4.4% error bars could be split into two parts: 3.8% and 2.4% associated with the positioning of the crack tip in K_I and K_{II} respectively, and 2.2% and 3.7% related to other factors, in K_I and K_{II} respectively. That is, looking at the ΔK_I curve (Figure 7.2) where the knee appears more clearly, the relative position between the points had an uncertainty of 2.2%. The other 3.8% was applicable to the curve as a whole.

Plasticity-induced and roughness-induced are possibly the two main closure mechanisms affecting the crack. The plasticity-induced closure was expected since the pre-cracking was performed at low ΔK levels and low R ratios [59] in a ductile material which was often found to exhibit plasticity-induced crack closure [120, 121]. In addition, the roughness-induced closure could presumably be motivated by a combination of the irregular shape of the crack flanks (see Figure 6.10) and the high level of sliding mode load applied [62, 115].

Crack closure effects can lead to retardation of the fatigue crack growth, thus improving the damage tolerance characteristics of many materials [59]. The incorporation in a simple way of closure concepts into fatigue life predictions would be very advantageous to many industries. By estimating closure levels with image correlation, important improvements can be obtained over other methods. In the case of compliance-based measurements, different closure levels were reported depending on the position of the strain gauges [78]. In the current work, the image correlation technique allowed us to collect a whole array of displacement data points in the region surrounding the crack tip. Accordingly, the effective SIF calculated included influences arising from the K-dominance zone and the crack wake. The closure level estimated based on effective SIF values can be considered as a sort of average of all the displacements occurring around the crack. These advantages are

shared with photoelasticity [29] and thermoelasticity [43]. The measurements are performed in a non-invasive fashion, as a consequence of the non-contacting nature of image correlation. This implies an important step forward for incorporating closure effects in fatigue life predictions of real structures.

In addition, the advantages of image correlation over other experimental techniques are also extended to the closure evaluation, as no coating needs to be bonded to the surface studied, no specific loading regime is required and the equipment is relatively cheap and easy to use.

The adoption of damage tolerance concept design has provided a growing demand for accurate material life prediction. The good results obtained for monitoring the effective mixed-mode SIF and evaluating crack closure levels, suggest that the approach could be used for health monitoring and estimation of residual life of real cracked structures, with the only need of increasing the capture rate of the camera, if the component is subjected to high loading frequencies.

8.2 Suggestions for future work

The methodology developed was applied to aluminium alloy specimens with thickness ranging from around 2 to 10 mm. No influence was detected between the thickness and the accuracy of the tool for SIF determination. The methodology could be applied to specimens with larger thickness in order to investigate if the same kind of errors arises, or on the contrary, for samples thicker than a determinate threshold, the elastic model no longer describes accurately enough the displacements occurring in the neighbourhood of the crack.

Given the recent developments in 3D image correlation developments [110], an interesting follow-up research field for making the methodology presented more comprehensive could be the extension of the mathematical analysis to the three dimensions so that the antiplane shear mode, K_{III}, can be taken into account. The elastic model could be then combined with displacement data in the three dimensions, including out-of-plane, giving as a result information for the three fracture modes of the crack driving force.

The last experimental chapter provides some results that are very promising for evaluating the opening point of a crack from a whole set of displacements surrounding the crack tip. To study the repeatability of these results in the same material would be an interesting additional area of research, and to compare with more traditional methods for closure evaluation based on compliance techniques.

By applying the methodology for closure evaluation to a whole cycle and studying the differences between opening and closure points occurring during the loading portion and unloading portion of the cycle, respectively. These results could then be compared with data available in the literature for the same material.

In addition, more reliable closure data could be obtained by developing an automatic and more objective method for evaluating the opening load. This could consist of identifying the opening load as the point where the slope of the SIF – load trend deviates by some small amount, e.g. 2% offset from the linear upper part of the plot.

By monitoring the SIF, but increasing the maximum K_I until fracture occurs could derive in an alternative fashion for measuring the fracture toughness of materials. In order to study the validity of the approach, some research would need to be done with different specimens for which analytical solutions are available. This could lead ultimately to a simple method for fracture toughness evaluation, without the need of machining standard specimen satisfying the requirements of [123].

The elastic model employed through this work assumed the crack being a traction-free contour. However, as discussed in previous chapters, this assumption can be infracted at some points of the crack, due to interaction between both upper and lower crack flanks. By taking into account important factors such as the asperity angle of the faceted crack surfaces or the friction coefficient, the boundary condition could be modified accordingly, and a model similar to that proposed by Tong and her co-workers [115] for sliding mode crack closure could be built. The model probably would provide more realistic results. These results could be then compared with the results obtained in the current work in order to assess the influence of contravening the boundary condition in some points along the crack.

Finally, although the approach was applied successfully to several cracked specimens, under a range of different conditions, including non-uniform passing stress field, the application of the tool to a real engineering component would bridge the gap

between laboratory based and industry based research work. The ease of utilization and portability of image correlation equipment would significantly aid the achievement of this new challenge.

Chapter 9

Conclusions

9.1 Overall conclusions

This thesis is the work conducted to investigate the potential of image correlation to evaluate the mixed-mode stress intensity factors of fatigue cracks. The main conclusions are summarized as follows:

- A new methodology for inferring mixed-mode (I + II) SIF has been developed. The methodology combines, by means of a multi-point over-deterministic method, experimental displacement data measured by image correlation with an elastic model describing the displacement field around a crack.
- The methodology has been proved to be sensitive to closure phenomena, giving information on effective values of the SIF rather than nominal ones. Closure and contact effects have been detected in both opening and sliding modes of crack displacements. Moreover the approach allows the identification of the opening load from the SIF on cyclic loading. Given that image correlation is a fast, non-contacting and relatively cheap and easy to use technique, the approach could be applied without difficulty in an industrial environment to real engineering components.
- Stress intensity factors for real fatigue cracks have been evaluated successfully for a range of conditions. Good agreement has been found between the experimental results and theoretical solutions. The main discrepancies are attributed to factors such as crack closure, wedging or crack face interlocking which make the theoretical solutions over-simplify the problem.

- The proposed method has been proved to be very successful in determining the opening mode SIF in samples subjected to pure mode I static loads. In addition it has been possible to monitor the SIF through several loading cycles with the same accuracy. Under these conditions of pure mode I nominally applied load, a noticeable mode II SIF was often measured, and this has been attributed to local mixed-mode conditions taking place at the crack tip.
- The methodology developed was able to describe, with the same accuracy, the opening mode and the sliding mode SIF in samples subjected to different levels of mixed-mode conditions.
- The combination of Muskhelishvili's approach with image correlation has been proved to be robust enough to handle complex situations where mixed-mode loads and stress concentrators were simultaneously present.
- The elastic model employed in the determination of the SIF has been built based on Muskhelishvili's approach, where two analytical functions were developed in terms of displacements. The two analytical functions can be used to reconstruct the full elastic solution, or, as in this work, to estimate the mixed-mode SIF.
- The methodology has been verified successfully with artificial images generated according to Westergaard's solution. The small errors measured arose from rounding errors accumulated throughout the computations. In addition, the methodology proved to be fast and stable in the presence of random and systematic noise.
- The accuracy of the technique in determining stress intensity factors has been found to be $\pm$ 0.73 MPa$\sqrt{m}$. The crack tip position has been identified as a critical factor affecting the accuracy of the technique. Uncertainty in locating the crack tip using the Sobel edge-finding routine is around 60 μm which results in less than 1.9% the error in the stress intensity factor, for the cases investigated.

Appendix A. Stress and displacement expressions in the mapping plane

This appendix shows the derivatives required to express the fundamental equations (3.1)-(3.3) in the mapping plane.

Taking (3.7) into account and applying the chain rule to the derivative of the analytical function $\varphi(z)$

$$\varphi'(\zeta) = \varphi'(z)z'(\zeta) = \varphi'(z)\omega'(\zeta) \tag{A.1}$$

or

$$\varphi'(z) = \frac{\varphi'(\zeta)}{\omega'(\zeta)} \tag{A.2}$$

Differentiating (A.2) with respect to z

$$\varphi''(z) = \frac{\omega'(\zeta)\frac{d}{dz}\varphi'(\zeta) - \varphi'(\zeta)\frac{d}{dz}\omega'(\zeta)}{[\omega'(\zeta)]^2} \tag{A.3}$$

or

$$\varphi''(z) = \frac{\omega'(\zeta)\varphi''(\zeta)/\omega'(\zeta) - \varphi'(\zeta)\omega''(\zeta)/\omega'(\zeta)}{[\omega'(\zeta)]^2} \tag{A.4}$$

or finally

$$\varphi''(z) = \frac{\varphi''(\zeta)\omega'(\zeta) - \varphi'(\zeta)\omega''(\zeta)}{[\omega'(\zeta)]^3} \tag{A.5}$$

Using the fundamental properties of functions of complex variable, the complex conjugates of (A.2) and (A.5) will be

$$\overline{\varphi'(z)} = \frac{\overline{\varphi'(\zeta)}}{\overline{\omega'(\zeta)}} \tag{A.6}$$

and

$$\overline{\varphi''(z)} = \frac{\overline{\varphi''(\zeta)\omega'(\zeta)} - \overline{\varphi'(\zeta)\omega''(\zeta)}}{\left[\overline{\omega'(\zeta)}\right]^3} \tag{A.7}$$

Similarly to (A.6)

$$\overline{\psi'(z)} = \frac{\overline{\psi'(\zeta)}}{\overline{\omega'(\zeta)}} \tag{A.8}$$

Substituting (3.7), (A.2), (A.6)-(A.8) into (3.1)-(3.3) one obtains the basic expressions in the mapping plane

$$\sigma_{xx} + i\sigma_{xy} = \frac{\varphi'(\zeta)}{\omega'(\zeta)} + \frac{\overline{\varphi'(\zeta)}}{\overline{\omega'(\zeta)}} - \omega(\zeta)\frac{\overline{\varphi''(\zeta)\omega'(\zeta)} - \overline{\varphi'(\zeta)\omega''(\zeta)}}{\left[\overline{\omega'(\zeta)}\right]^3} - \frac{\overline{\psi'(\zeta)}}{\overline{\omega'(\zeta)}} \tag{A.9}$$

$$\sigma_{yy} + i\sigma_{xy} = \frac{\varphi'(\zeta)}{\omega'(\zeta)} + \frac{\overline{\varphi'(\zeta)}}{\overline{\omega'(\zeta)}} + \omega(\zeta)\frac{\overline{\varphi''(\zeta)\omega'(\zeta)} - \overline{\varphi'(\zeta)\omega''(\zeta)}}{\left[\overline{\omega'(\zeta)}\right]^3} + \frac{\overline{\psi'(\zeta)}}{\overline{\omega'(\zeta)}} \tag{A.10}$$

$$2\mu(u + iv) = \chi\varphi(\zeta) - \frac{\omega(\zeta)}{\overline{\omega'(\zeta)}}\overline{\varphi'(\zeta)} - \overline{\psi(\zeta)} \tag{A.11}$$

Appendix B. Fourier series representation of the boundary condition and the displacement equation

Unless stated otherwise in the following, the sums are always assumed from minus to plus infinity. Accordingly only the sum index is given.

By substituting (3.14)-(3.16) into (3.13) and taking into account that

$$\bar{\eta} = e^{-i\theta} = \eta^{-1} \tag{B.1}$$

one obtains the boundary condition in the mapping plane, with the terms expanded in a Fourier series:

$$\sum_k a_k \zeta^k + \sum_l c_l \eta^l \sum_k k \bar{a}_k \eta^{-k+1} + \sum_k \bar{b}_k \eta^{-k} = 0 \tag{B.2}$$

and multiplying out the series in the middle term of the left-hand side

$$\sum_k a_k \zeta^k + \sum_l \sum_k k \bar{a}_k c_l \eta^{l-k+1} + \sum_k \bar{b}_k \eta^{-k} = 0 \tag{B.3}$$

Comparing coefficients of η^m (m = 1, 2, ...), one finds

$$a_m + \sum_k k \bar{a}_k c_{m+k-1} + \bar{b}_{-m} = 0 \tag{B.4}$$

similarly, one obtains from η^m (m = 0, 1, 2, ...)

$$b_k = -\bar{a}_{-k} - \sum_l l a_l \bar{c}_{l-k-1} \tag{B.5}$$

Substituting (B.5) into (5.15), $\psi(\eta)$ can be rewritten as

$$\psi(\zeta) = \sum_k \left(-\bar{a}_{-k} - \sum_l l a_l \bar{c}_{l-k-1} \right) \zeta^k \tag{B.6}$$

Substituting (3.14) and (B.6) into (3.10) one obtains the displacements equation in the mapping plane with the terms developed in Fourier series:

$$2\mu(u+iv) = \chi \sum_k a_k \zeta^k - \frac{\omega(\zeta)}{\omega'(\zeta)} \sum_k k \bar{a}_k \overline{\zeta^{k-1}} - \sum_k \left(-a_{-k} - \sum_l l \bar{a}_l c_{l-k-1} \right) \overline{\zeta^k} \tag{B.7}$$

Equation (B.7) is a linear equation with respect to an infinite number of complex unknowns, a_k, where the near field boundary condition is implicit, halving the number of unknowns.

Because of the symmetry of the series in (B.7), from minus to plus infinity, the summation index k may be substituted by $-k$. Applying this property to the last series in (B.7) and using (5.17), expression (B.7) can be rewritten as

$$\chi\sum_k a_k\zeta^k - \Omega(\zeta)\sum_k k\bar{a}_k\overline{\zeta^{k-1}} + \sum_k\left(+a_k + \sum_l \bar{l}\bar{a}_l c_{l+k-1}\right)\overline{\zeta^{-k}} = 2\mu(u+iv) \tag{B.8}$$

By splitting the complex variables into real and imaginary parts

$$a_k = \alpha_k + i\beta_k \tag{B.9}$$

(B.8) will yield two real linear equations with respect to an infinite number of real unknowns, $\alpha_k = \mathrm{Re}a_k$ and $\beta_k = \mathrm{Im}a_k$.

$$\begin{aligned}\chi\sum_k(\alpha_k+i\beta_k)(\mathrm{Re}\,\zeta^k+i\,\mathrm{Im}\,\zeta^k) - \\ -\Omega\sum_k k(\alpha_k-i\beta_k)(\mathrm{Re}\,\zeta^{k-1}-i\,\mathrm{Im}\,\zeta^{k-1}) + \\ +\sum_k\left((\alpha_k+i\beta_k)+\sum_l l(\alpha_l-i\beta_l)(\mathrm{Re}\,c_{l+k-1}+i\,\mathrm{Im}\,c_{l+k-1})\right)(\mathrm{Re}\,\zeta^{-k}-i\,\mathrm{Im}\,\zeta^{-k}) = \\ = 2\mu(u+iv)\end{aligned} \tag{B.10}$$

In order to obtain a non-infinite number of unknowns, the series in (B.10) have to be limited. Let us designate N and M as the limits for the series sub-indexed k and l respectively. After a series of simple but lengthy transformations, and limiting the series, (B.10) can be written as two equations in real variables

$$\sum_{k=-N}^{N} C_k\alpha_k + \sum_{k=-N}^{N} D_k\beta_k = 2\mu u \tag{B.11}$$

$$\sum_{k=-N}^{N} E_k\alpha_k + \sum_{k=-N}^{N} F_k\beta_k = 2\mu v \tag{B.12}$$

where

$$\begin{aligned}C_k = \chi\,\mathrm{Re}\,\zeta^k - k\,\mathrm{Re}\,\Omega\,\mathrm{Re}\,\zeta^{k-1} - k\,\mathrm{Im}\,\Omega\,\mathrm{Im}\,\zeta^{k-1} + \mathrm{Re}\,\zeta^{-k} + \\ + k\sum_{l=-M}^{M}\mathrm{Re}\,c_{l+k-1}\,\mathrm{Re}\,\zeta^{-l} + k\sum_{l=-M}^{M}\mathrm{Im}\,c_{l+k-1}\,\mathrm{Im}\,\zeta^{-l}\end{aligned} \tag{B.13}$$

$$\begin{aligned}D_k = -\chi\,\mathrm{Im}\,\zeta^k + k\,\mathrm{Re}\,\Omega\,\mathrm{Im}\,\zeta^{k-1} - k\,\mathrm{Im}\,\Omega\,\mathrm{Re}\,\zeta^{-k} + \mathrm{Im}\,\zeta^{-k} - \\ - k\sum_{l=-M}^{M}\mathrm{Re}\,c_{l+k-1}\,\mathrm{Im}\,\zeta^{-l} + k\sum_{l=-M}^{M}\mathrm{Im}\,c_{l+k-1}\,\mathrm{Re}\,\zeta^{-l}\end{aligned} \tag{B.14}$$

$$E_k = \chi \operatorname{Im}\zeta^k + k \operatorname{Re}\Omega \operatorname{Im}\zeta^{k-1} - k \operatorname{Im}\Omega \operatorname{Re}\zeta^{-k} - \operatorname{Im}\zeta^{-k} - \\ - k \sum_{l=-M}^{M} \operatorname{Re} c_{l+k-1} \operatorname{Im}\zeta^{-l} + k \sum_{l=-M}^{M} \operatorname{Im} c_{l+k-1} \operatorname{Re}\zeta^{-l} \tag{B.15}$$

$$F_k = \chi \operatorname{Re}\zeta^k + k \operatorname{Re}\Omega \operatorname{Re}\zeta^{k-1} + k \operatorname{Im}\Omega \operatorname{Im}\zeta^{k-1} + \operatorname{Re}\zeta^{-k} - \\ - k \sum_{l=-M}^{M} \operatorname{Re} c_{l+k-1} \operatorname{Re}\zeta^{-l} - k \sum_{l=-M}^{M} \operatorname{Im} c_{l+k-1} \operatorname{Im}\zeta^{-l} \tag{B.16}$$

(B.11)-(B.12) is a system of 2 equations and $2(2N + 1)$ unknowns ($2N + 1$ unknowns α_k and $2N + 1$ unknowns β_k), obtained from a single point ζ. Considering p points ζ the system will have $2p$ equations:

$$\sum_{k=-N}^{N} C_k^j \alpha_k + \sum_{k=-N}^{N} D_k^j \beta_k = 2\mu u^j \tag{B.17}$$

$$\sum_{k=-N}^{N} E_k^j \alpha_k + \sum_{k=-N}^{N} F_k^j \beta_k = 2\mu v^j \tag{B.18}$$

where $j = 1, 2, \ldots p$, u^j and v^j are the displacements at point j, and C_k^j, D_k^j, E_k^j and F_k^j are coefficients defined by (B.13)-(B.16) calculated at a point j.

Appendix C. Mapping a unit circle onto an ellipse

By working out the variable ζ from (3.21)

$$\zeta = \frac{z \pm \sqrt{z^2 - 4R^2 m}}{2R} \tag{C.1}$$

Expression (C.1) has two solutions, one inside the unit circle, $|\zeta| \leq 1$ and another outside the unit circle $|\zeta| \geq 1$. In the following only $|\zeta| \geq 1$ will be considered. Differentiating (3.21) and using the properties of complex numbers one obtains

$$\omega'(\zeta) = R\left(1 - \frac{m}{\zeta^2}\right); \qquad \overline{\omega'(\zeta)} = R\left(1 - \frac{m}{\overline{\zeta}^2}\right) \tag{C.2}$$

Substituting (3.21) and (C.2) into (B.8) one arrives at

$$\Omega(\zeta) = \frac{R(\zeta + m/\zeta)}{R(1 - m/\overline{\zeta}^2)} = \frac{\zeta + m/\zeta}{1 - m/\overline{\zeta}^2} \tag{C.3}$$

By considering the points in the unit circle, (C.3) becomes

$$\Omega(\eta) = \frac{\eta + m/\eta}{1 - m/\overline{\eta}^2} \tag{C.4}$$

or using (B.1)

$$\Omega(\eta) = \frac{\eta + m/\eta}{1 - m\eta^2} = \frac{m}{\eta} + \eta(m^2 + 1)\frac{1}{1 - m\eta^2} \tag{C.5}$$

The term $1/(1 - m\eta^2)$ can be developed in Maclaurin's series as

$$\frac{1}{1 - m\eta^2} = \sum_{k=0}^{+\infty} (m\eta^2)^k \tag{C.6}$$

The series (C.6) will absolutely converge if $|m\eta^2| < 1$ [124]. Because

$$|m\eta^2| = \sqrt{m\eta^2 \cdot m\overline{\eta}^2} = \sqrt{m\eta^2 \cdot m\eta^{-2}} = m \tag{C.7}$$

the series (C.6) will only converge for $m < 1$.

Combining (C.5) and (C.6) one obtains

$$\Omega(\eta)=\frac{m}{\eta}+\eta(m^2+1)\sum_{k=1}^{+\infty}\left(m\eta^2\right)^k=m\eta^{-1}+(m^2+1)\sum_{k=0}^{+\infty}m^k\eta^{2k+1} \tag{C.8}$$

Accordingly the truncated series for $\Omega(\eta)$ can be written as

$$\Omega(\eta)=\sum_{l=-M}^{+M}c_l\eta^l \tag{C.9}$$

where

$$c_l=\begin{cases} m & l=-1 \\ (m^2+1)m^{\frac{l-1}{2}} & l=2n+1 \quad n=0,\ 1,\ 2,\ \ldots \\ 0 & \text{all other } l \end{cases} \tag{C.10}$$

Appendix D. Loads employed in the experiments

Specimen	Identification	Load, KN	Specimen	Identification	Load, KN
WOL	a = 24 mm	8.95	CCP	θ = 0 deg	16.00
WOL	a = 24 mm	5.18	CCP	θ = 15 deg	16.00
WOL	a = 24 mm	1.17	CCP	θ = 30 deg	15.00
WOL	a = 31 mm	5.86	CCP	θ = 45 deg	9.75
WOL	a = 31 mm	5.02	CCP	θ = 60 deg	14.00
WOL	a = 31 mm	4.40	CCP	θ = 75 deg	8.77
WOL	a = 34 mm	6.45	CCP	θ = 90 deg	8.45
WOL	a = 34 mm	4.46	CFH	θ = 0 deg	17.00
WOL	a = 34 mm	2.93	CFH	θ = 15 deg	17.00
WOL	a = 49 mm	2.10	CFH	θ = 30 deg	17.00
WOL	a = 49 mm	1.83	CFH	θ = 45 deg	17.00
WOL	a = 49 mm	1.61	CFH	θ = 60 deg	17.00
WOL	a = 54 mm	1.66	CFH	θ = 75 deg	17.00
WOL	a = 54 mm	0.98	CFH	θ = 90 deg	17.00
WOL	a = 54 mm	0.26			

Table D.1: Loads employed in the different experiments for the wedge opening loaded (WOL), centre crack plate (CCP) and crack emanating from a hole (CFH) geometries.

References

1. Inglis, C. E. (1913) Stresses in a plate due to the presence of cracks and sharp corners. Transactions of the Institution of Naval Architects **55**, 219-230.
2. Sneddon, I. N. (1946) The distribution of stress in the neighbourhood of a crack in an elastic solid. In *Proceedings of the Royal Society A*, Vol. 187, 229-260.
3. Westergaard, H. M. (1939) Bearing pressures and cracks. *Journal of Applied Mechanics.* **61**, A49-53.
4. Kobayashi A. S. (1985) Linear Elastic Fracture Mechanics, in *Computational Methods in the Mechanics of Fracture* (S. N. Atluri, Ed.), North-Holland, Amsterdam, 21-53.
5. Sih, G. C. On Westergaard method of crack analysis. *International Journal of Fracture Mechanics*, v. 2, pp. 628-631 (1966).
6. Eftis, J., Liebowittz, H. On the modified Westergaard equations for certain plane crack problems. *International Journal of Fracture Mechanics*, 8(4), 383-392 (1972).
7. Schroedl, M. A., McGowan, J. J. and Smith, C. W. (1972) An assessment of factors influencing data obtained by the photoelastic stress freezing technique for stress fields near crack tips. *Engineering Fracture Mechanics* **4**, 801-809.
8. Evans, W. T. and Luxmoore (1976) Limitations of the Westergaard equations for experimental evaluations of stress intensity factors. *Journal of Strain Analysis* **11**(3), 177-185.
9. Sanford, R. J. (1979) A critical re-examination of the Westergaard method for solving opening-more crack problems. *Mechanics Research Communications* **6**(5), 289-294.

10. Eftis, J., Subramonian, N. and Liebowitz, H. (1977) Crack border stress and displacement equations revisited. *Engineering Fracture Mechanics* **9**, 189-210.
11. Theocaris, P. S. and Michopoulos, J. G. (1983) A closed-form solution of a slant crack under biaxial loading. *Engineering Fracture Mechanics* **17**(2), 97-123.
12. Muskhelishvili, N. I. (1953) *Some basic problems of the mathematical theory of elasticity.* Noordhoff Ltd, Netherlands.
13. Barenblatt, G. I. (1962) The mathematical theory of equilibrium cracks in brittle fracture, in *Advances in Applied Mechanics* (H. L. Dryden and Th. Von Kármán, Ed.), **7**, 55-129. Academic Press, Inc.
14. Bowie, O. L. (1956) Analysis of an infinite plate containing radial cracks originating at the boundary of an internal circular hole. *Journal of Mathematics and Physics* **35**, 60-71.
15. Bowie, O. L. (1964) Rectangular tensile sheet with symmetric edge cracks. *Journal of Applied Mechanics* **31**, 208-212.
16. Bowie, O. L. and Neal, D. M. (1970) A modified mapping-collocation technique for accurate calculation of stress intensity factor. *International Journal of Fracture* **6**(2), 199-206.
17. Bowie, O. L., Freese, C. E. and Neal, D. M. (1973) Solution of plane problems of elasticity utilizing portioning concepts. *Journal of Applied Mechanics* 40, 767-772.
18. Paris, P. C. and Sih, G. S. (1965) Stress Analysis of Cracks. *Fracture Toughness and Its Applications, ASTM STP* **381**, pp. 30-83.
19. Post, D. (1954) Photoelastic stress analysis for an edge crack in a tensile field. In: *Proceedings of SESA* **12**, 99-116.
20. Wells, A. A. and Post, D. (1958) The dynamic stress distribution surrounding a running crack – a photoelastic investigation. In *Proceedings of SESA* **16**, 69-96.
21. Sanford, R. J. and Dally, J. W. (1979) A general method for determining mixed-mode stress intensity factors from isochromatic fringe patterns. *Engineering Fracture Mechanics* **11**(4), 621-633.
22. Dally, J. W., Fourney, W. L. and Irwin, G. R. (1985) On the uniqueness of the stress intensity factor – crack velocity relationship. *International Journal of Fracture* **27**, 159-168.

23. Wang, W. C. and Chen, T. L (1989) Half-fringe photoelastic determination of opening mode stress intensity factor for edge cracked strips. *Engineering Fracture Mechanics* **32**(1), 111-122.

24. Prabhu, M. M., Gobdole, P. B., Bhave, S. K. and Srinath, L. S. (1987) New approaches for photoelastic determination of stress intensity factors. *Mechanics Research Comunications* **14**(4), 237-244.

25. Gdoutos, E. E. and Aifantis, E. C. (1990) Solute distribution in crack tips under mixed mode I/II conditions. *Acta Mechanica* **82**, 1-9.

26. Nurse, A. D. and Patterson, E. A. (1993) Determination of predominantly mode II stress intensity factors from isochromatic data. *Fatigue and Fracture of Engineering Materials and Structures*, **16**(12), 1339-1354.

27. Picón, R., París, F., Canas, J. and Marín, J. (1995) A complete field method for the photoelastic determination of K_I and K_{II} in general mixed-mode fracture. *Engineering Fracture Mechanics* **51**(3), 505-516.

28. Patterson, E. A. and Olden, E. J. (2004) Optical analysis of crack tip stress fields: a comparative study. *Fatigue and Fracture of Engineering Materials and Structures*, **27**(7), 623-635.

29. Pacey, M. N., James, M. N. and Patterson, E. A. (2005) A new photoelastic model for studying fatigue crack closure. *Experimental Mechanics*, **45**(1), 42-52.

30. Lai, Z. G. and Sun, P. (1983) Photoelastic determination of mixed-mode stress-intensity factors K_I, K_{II} and K_{III}. *Experimental Mechanics* **23**(2), 228-235.

31. Razumovskii, I. A. (1989) Determination of stress intensity factor K_I, K_{II} and K_{III} by polarization-optical methods in homogeneous and piecewise-homogeneous components and specimens with cracks. *Industrial Laboratory*, **54**(10), 1158-1165.

32. Patterson, E. A. and Gungor, S. (1997) A photoelastic study of an angle crack specimen subject to mixed mode I-III displacements. *Engineering Fracture Mechanics*, **56**(6), 767-778.

33. Dally, J. W., Fourney, W. L. and Irwin, G. R. (1985) On the uniqueness of the stress intensity factor – crack velocity relationship. *International Journal of Fracture*, **27**, 159-168.

34. Parameswaran, V. and Shukla, A. (1999) Crack-tip stress fields for dynamic fracture in functionally gradient materials. *Mechanics of Materials*, **31**, 579-596.

35. Theocaris, P. S., Tsamasphyros, G. J. and Mikroudis, G. (1982) A combined integral-equation and photoelastic method for solving contact problems. *Acta Mechanica*, **45**, 215-231.

36. Dally, J. W. and Chen, Y. M. (1991) A photoelastic study of friction at multipoint contacts. *Experimental Mechanics*, **31**(2), 144-149.

37. Lu, H. and Chiang, F. P. (1993) Photoelastic determination of stress intensity factor of an interfacial crack in a bi-material. *Journal of Applied Mechanics – Transactions of ASME*, **60**(1), 93-100.

38. Soh, A. K. (1999) An improved photo-elastic technique for determining the mixed-mode stress intensity factors for interfacial cracks in a bi-material. *Composite Science and Technology*, **59**(7), 1033-1039.

39. Tirosh, J. and Ladelski, A. (1980) Note on residual-stresses induced by fatigue cracking. *Engineering Fracture Mechanics*, **13**(3), 453-461.

40. Stanley, P. and Chan, W. K. (1986) The determination of stress intensity factors and crack-tip velocities from thermoelastic infra-red emissions. In *Proceedings of the Institution of Mechanical Engineers, Sheffield, UK*, 105-114.

41. Stanley, P. and Chan, W. K. (1986) Mode II crack studies using the "SPATE" technique. In *Proceedings of the 1986 SEM Spring Conference on Experimental Mechanics, New Orleans, LA, USA*, 916-923.

42. Tomlinson, R. A., Nurse, A. D. and Patterson, E. A. (1997) On determining stress intensity factors for mixed mode cracks from thermoelastic data. *Fatigue and Fracture of Engineering Materials and Structures*, **20**(2), 217-226.

43. Díaz, F. A., Patterson, E. A., Tomlinson, R. A. and Yates, J. R. (2004) Measuring stress intensity factors during fatigue crack growth using thermoelasticity. *Fatigue and Fracture of Engineering Materials and Structures*, **27**(7), 571-583.

44. Kalthoff, J. F. (1993) Shadow optical method of caustics, in *Handbook of Experimental Mechanics* (Kobayashi, A. S., Ed) Prentice Hall, Englewood Cliffs, New Jersey, 407-478.

45. Carazo-Álvarez, J. D. and Patterson, E. A. (1999) A general method for automated analysis of caustics. *Optics and Lasers in Engineering*, **32**, 95-110.

46. Younis, N. T. and Libii, J. N. (1992) Determination of K_I and K_{II} by using a least-squares method with caustics. *Engineering Fracture Mechanics*, **42**(4), 629-641.

47. Barker, D. B., Sanford, R. J. and Chona, R. (1985) Determining K and related stress-field parameters from displacement fields. *Experimental Mechanics*, **25**(4), 399-405.

48. Moore, A. J. and Tyrer, J. R. (1995) Phase-stepped ESPI and Moiré interferometry for measuring stress-intensity factor and J integral. *Experimental Mechanics*, **35**, 306-314.

49. Moore, A. J. and Tyrer, J. R. (1994) Evaluation of fracture mechanic's parameters using electronic speckle pattern interferometry. *Journal of Strain Analysis*, **29**(4), 257-262.

50. Shterenlikht, A., Díaz Garrido, F. A., López-Crespo, P., Withers, P. J. and Patterson, E. A. (2004) Mixed mode (K_I + K_{II}) stress intensity factor measurement by electronic speckle pattern interferometry and image correlation. *Applied Mechanics and Materials*, **1-2**, 107-112.

51. McNeill, S. R., Peters, W. H. and Sutton, M. A. (1987) Estimation of stress intensity factor by digital image correlation. *Engineering Fracture Mechanics*, **28**(1), 101-112.

52. Durig, B., Zhang, F., McNeill, S. R., Chao, Y. J. and Peters III, W. H. (1991) A study of mixed mode fracture by photoelasticity and digital image correlation. *Optics and Lasers in Engineering*, **14**, 203-215.

53. Abanto-Bueno, J. and Lambros, J. (2002) Investigation of crack growth in functionally graded materials using image correlation. *Engineering Fracture Mechanics*, **69**, 1695-1711.

54. Samarasinghe, S. and Kulasiri, D. (2004) Stress intensity factor of wood from crack-tip displacement fields obtained from digital image correlation. *Silva Fennica*, **38**(3), 267-278.

55. Hild, F. and Roux, S. (2006) Measuring stress intensity factors with a camera: integrated digital image correlation (I-DIC). *C. R. Mecanique*, **334**, 8-12.

56. Yoneyama, S., Morimoto, Y. and Takashi, M. (2006) Automatic evaluation of mixed-mode stress intensity factors utilizing digital image correlation. *Strain*, **42**, 21-29.
57. Elber, W. (1970) Fatigue crack closure under cyclic tension. *Engineering Fracture Mechanics*, **2**(1), 37-45.
58. Elber, W. (1971) The significance of fatigue crack closure. *ASTM 486, American Society of Testing Materials*, 230-242.
59. Suresh, S. (2004) *Fatigue of Materials.* Cambridge University Press, Cambridge.
60. Carman, C. D., Turner, C. C. and Hillberry, B. M. (1988) A method for determining crack opening load from load-displacement data. *Mechanics of Fatigue Crack Closure, ASTM STP* **982**, pp. 214-221.
61. Suresh, S., Zamiski, G. F. And Ritchie, R. O. (1981) Oxide-induced crack closure: as explanation for near threshold corrosion fatigue crack behaviour. *Metallurgical Transaction A*, **12A**, 1435-1443.
62. Ritchie, R. O. and Suresh, S. (1982) Some considerations on fatigue crack closure at near-threshold stress intensities due to fracture surface morphology. *Metallurgical Transaction A*, **13A**, 937-940.
63. Endo, K., Okada, T. and Hariya, T. (1972) Fatigue crack propagation in bearing metals lining of steel plates in lubricating oil. *Bulletin of the Japan Society of Mechanical Engineers*, **15**, 439-445.
64. Pineau, A. G. and Pelloux, R. M. N. (1974) Influence of strain-induced martensitic transformations on fatigue crack growth rates in stainless steel. *Metallurgical Transactions*, **5A**, 1103-1112.
65. Shijve, J. (1988) Fatigue crack closure, observations and technical significance, in *ASTM STP 982*, 5-34.
66. Jones, J. W., Macha, D. E. and Corbly, D. M. (1978) Observations on fatigue crack opening determinations. *International Journal of Fracture*, **14**, 25-30.
67. Evans, W. J. and Spence, S. H. (1997) Characterization of crack tip and geometry induced crack closure. *International Journal of Fatigue*, **19**(1), 205-210.
68. Bowman, R., Antolovich, S. D. and Brown, R. C. (1988) A demonstration of problems associated with crack closure measurements techniques. *Engineering Fracture Mechanics*, **31**(4), 703-712.

69. Vecchio, R. S., Crompton, J. S. and Hertzberg, R. W. (1986) Anomalous aspects of crack closure. *International Journal of Fracture*, **31**, R29-R33.

70. Davidson, D. L. (1991) Fatigue crack closure. *Engineering Fracture Mechanics*, **38**(6), 393-402.

71. Sutton, M. A., Zhao, W., McNeill, S. R., Helm, J. D., Piascik, R. S. and Riddell, W. T. (1999) Local crack closure measurements: developments of a measurement system using computer vision and a far-field microscope, in *ASTM STP* **1343**, 145-156.

72. Sehitoglu, H. (1985) Crack opening and closure in fatigue. *Engineering Fracture Mechanics*, **2**, 329-339.

73. Vasudévan, A. K., Sabananda, K. and Louat, N. (1993) Two critical stress intensities for threshold fatigue crack propagation. *Scripta Metallurgica et Materalia*, **28**, 65-70.

74. Lal, D. N. (1996) A detailed physical analysis of the R-effect on LEFM fatigue crack growth – II. On the combined roles of growth mechanisms and stress ratio. *Engineering Fracture Mechanics*, **55**(2), 289-312.

75. Vasudeven, A. K., Sabananda, Louat, N. (1994) A review of crack closure, fatigue crack threshold and related phenomena. *Materials Science and Engineering*, **A188**, 1-22.

76. Shih, T. T. and Wei, R. P. (1974) A study of crack closure in fatigue. *Engineering Fracture Mechanics*, **6**, 19-32.

77. Chen, D. L., Weiss, B. and Stickler, R. (1991) A new evaluation procedure for crack closure. *International Journal of Fatigue*, **13**(4), 327-331.

78. James, M. N. (1996) Some unresolved issues with fatigue crack closure measurement, mechanisms and interpretation problems. In *Advance in Fracture Research, Proceedings of the Ninth International Conference on Fracture* (B. L. Karihaloo et al. Ed.), Pergamon Press, **5**, 2403-2414.

79. Clarke, C. K. and Cassatt, G. C. (1977) A study of fatigue crack closure using electric potential and compliance techniques. *Engineering Fracture Mechanics*, **9**, 675-688.

80. Gan, D. and Weertman, J. (1981) Crack closure and crack propagation rates in 7050 aluminium. *Engineering Fracture Mechanics*, **15**, 87-106.

81. Vasudevan, A. K., Sabananda, K. and Louat, N. (1992) Reconsideration of fatigue crack closure. *Scripta Metallurgica et Materalia*, **27**, 1673-1678.

82. James, M. N. and Knott, J. F. (1985) Critial aspects of the characterization of crack tip closure by compliance techniques. *Materials Science and Engineering*, **72**, 1-4.

83. Garz, R. E. and James, M. N. (1989) Observations on evaluating fatigue crack closure from compliance traces. *International Journal of Fatigue*, **11**(6), 437-440.

84. Pippan, R. (1988) The sensitivity to measure crack closure with strain gauges near the crack tip. *Engineering Fracture Mechanics*, **31**(5), 867-871.

85. Yisheng, W. and Schijve, J. (1995) Fatigue crack closure measurements on 2024-T3 sheet specimens. *Fatigue and Fracture of Engineering Materials and Structures*, **18**(9), 917-921.

86. Peters, W. H. and Ranson, W. F. (1982) Digital imaging techniques in experimental stress analysis. *Optical Engineering*, **21**(3), 427-432.

87. Chu, T. C., Ranson, W. F., Sutton, M. A. and Peters, W. H. (1985) Application of digital-image correlation techniques to experimental mechanics. *Experimental Mechanics*, **25**(3), 232-244.

88. Sutton, M. A., McNeill, S. R., Jang, J. and Babai, M. (1988) Effects of subpixel image restoration on digital correlation error estimates. *Optical Engineering*, **27**(10), 870-877.

89. Bruck, H. A., McNeill, S. R., Sutton, M. A. and Peters III, W. H. (1989) Digital image correlation using Newton-Raphson method of partial differential corrections. *Experimental Mechanics*, **29**(3), 261-267.

90. Sutton, M. A., Bruck, H. A., Chae, T. L. and Turner, J. L. (1992) Experimental investigations of three-dimensional effects near a crack-tip using computer vision. *International Journal of Fracture*, **53**, 201-228.

91. Han, G., Sutton, M. A. and Chao, Y. J. (1995) A study of stable crack growth in thin SEC specimens of 304 stainless steel. *Engineering Fracture Mechanics*, **52**(3), 525-531.

92. Peters, W. H., Zheng-Hui, H., Sutton, M. A. and Ranson, W. F. (1984) Two-dimensional fluid velocity measurements by use of digital speckle correlation techniques. *Experimental Mechanics*, **24**(2), 117-121.

93. Wu, W., Peters, W. H., Hammer, M. (1987) Basic mechanical properties of retina in simple elongation. *Transactions of ASME, Journal of Biomechanical Engineering*, **109**(1), 65-67.

94. Han, G., Sutton, M. A. and Chao, Y. J. (1994) A study of stationary crack-tip deformation fields in thin sheets by computer vision. *Experimental Mechanics*, **34**(2), 125-140.

95. Dawicke, D. S. and Sutton, M. A. (1994) CTOA and crack tunneling measurements in thin sheet 2024-T3 aluminum alloy. *Experimental Mechanics*, **34**(4), 357-368.

96. Dawicke, D. S., Sutton, M. A., Newman, J. C. and Bigelow, C. A. (1995) Measurement and analysis of critical CTOA for an aluminum alloy sheet, in *ASTM STP 1220 on Fracture Mechanics*, **25**, 358-379.

97. McNeill, S. R., Sutton, M. A., Miao, Z. and Ma, J. (1997) Measurement of surface profile using digital image correlation. *Experimental Mechanics*, **37**(1), 13-20.

98. Amstutz, B. E., Sutton, M. A. and Dawicke, D. S. (1995) Experimental study of mixed mode I/II stable crack growth in thin 2024-T3 aluminum, in *ASTM STP 1256 on Fracture Mechanics*, **26**, 256-271.

99. Quinta da Fonseca, J., Mummery, P. M. and Withers, P. J. (2005) Full-field strain mapping by optical correlation of micrographs acquired during deformation. *Journal of Microscopy*, **218**(1), 9-21.

100. Clocksin, W. F., Quinta da Fonseca, J., Withers, P. J. and Torr, P. H. S. (2002) image processing issues in digital strain mapping, in *Proceedings of SPIE, Application of Digital Image Processing XXV* (A. G. tescher, Ed.), **4790**, 384-395.

101. LaVision GmbH. (2005) *PIV Software Manual: DaVis*. Gottingem, Germany, 7.1 edition.

102. England, A. H. (1971) *Complex Variable Methods in Elasticity*. Wiley – Interscience.

103. Press, W. H., Teukolsky, S. A., Vetterling, W. T. and Flannery, B. P. (1992) *Numerical Recipes in FORTRAN: the Art of Scientific Computing*. Cambridge University Press, 2nd edition.

104. Golub, G. H. and Van Loan, C. F. (1996) *Matrix Computations.* The John Hopkins University Press, 3rd edition.

105. Sih, G. C., Paris, P. C. and Erdogan, F. (1962) Crack-tip stress-intensity factors for plane extension and plate bending problems. *Journal of Applied Mechanics*, **29**, 306-312.

106. Goldberg, D. (1991) What every computer scientist should know about floating-point arithmetic. *ACM Computing Surveys*, **23**(1), 5-48.

107. Murakami, Y. (1987) *Stress Intensity Factors Handbook.* Oxford: Pergamon Press.

108. Otsuka, A., Tohgo, K. and Matsuyama, H. (1987) Fatigue crack initiation and growth under mixed mode loading in Aluminium alloys 2017-T3 and 7075-T6. *Engineering Fracture Mechanics*, **28**(5/6), 721-732.

109. Nurse, A. D., O'Brien, E. W. and Patterson, E. A. (1994) Stress intensity factors for cracks at fastener holes. *Fatigue and Fracture of Engineering Materials and Structures*, **17**(7), 791-799.

110. Sutton, M. A., McNeill, S. R., Helm, J. D. and Chao, Y. J. (2000) Advances in two-dimensional and three-dimensional computer vision, in *Photomechanics, Topics in Applied Physics* (P. K. Rastogi, Ed.), **77**, 323-372.

111. Sanford, R. J. (1980) Application of the least-squares method to photoelastic analysis. *Experimental Mechanics*, **20**(6), 192-197.

112. Goldberg, D. E. (1989) *Genetic Algorithms in Search, Optimization, and Machine Learning.* Addison-Wesley.

113. The MathWorks, Inc. (2001) *Image Processing Toolbox User's Guide, For Use With Matlab.* Version 3.0.

114. Sonka, M., Hlavac, V. and Boyle, R. (1993) *Image Processing, Analysis and Machine Vision.* Chapman and Hall International.

115. Tong, J., Yates, J. R. and Brown, M. W. (1995) A model for sliding mode crack closure. Parts I and II. *Engineering Fracture Mechanics*, **52**(4), 599-623.

116. Higham, N. J. (1996) *Accuracy and Stability of Numerical Algorithms.* Society for Industrial and Applied Mathematics, Philadelphia..

117. Tschegg, E. K. (1983) Sliding mode closure and mode III fatigue crack growth in mild steel. *Acta Metallurgica*, **31**(9), 1323-1330.

118. Smith, M. C. and Smith, R. A. (1988) Towards an understanding of mode II fatigue crack growth. *Basic Questions in Fatigue, ASTM STP* **924**, pp.260-280.

119. Tong, J., Yates, J. R. and Brown, M. W. (1994) The influence of precracking technique on branch crack threshold behaviour under mode I/II loading. *Fatigue and Fracture of Engineering Materials and Structures*, **17**(11), 1261-1269.

120. Newman Jr., J. C., Irving, P. E., Lin, J. and Le, D. D. (2006) Crack growth predictions in a complex helicopter component under spectrum loading. *Fatigue and Fracture of Engineering Materials and Structures*, **29**(11), 949-958.

121. Zitounis, V. and Irving, P. E. (2007) Fatigue crack acceleration effects during tensile underloads in 7010 and 8090 aluminium alloys. *International Journal of Fatigue*, **29**(1), 108-118.

122. Stoychev, S. and Kujawski, D. (2003) Methods for opening load and crack tip shielding determination: a review. *Strain*, **26**, 1053-1067.

123. ASTM (1997) Standard test method for plane-strain fracture toughness of metallic materials, E399-90. *Annual Book of ASTM Standards*, pp. 431-461.

124. Sokolnikoff, I. S. and Sokolnikoff, E. S. (1941) *Higher Mathematics for Engineers and Physicists*. McGraw-Hill, 2nd edition.

Papers written during the course of this work

The following papers have been written:

- P. López-Crespo, E. A. Patterson, A. Shterenlikht, P. J. Withers and J. R. Yates. Study of a crack at a fastener hole by image correlation. Society of Experimental Mechanics Annual Conference and Exposition, 3-6 June 2007, Springfield, Massachusetts, USA. Accepted.

- Y. H. Tai, P. López-Crespo, S. Ayvar, A. Shterenlikht, J. R. Yates, E. A. Patterson and P. J. Withers. Optical experimental methods for determining fatigue and fracture properties. In: Proceedings of Fatigue 2007 – The 6th Engineering Integrity Society International Conference on Durability and Fatigue, 26-28 March 2007, Cambridge, UK. Accepted.

- P. López-Crespo, A. Shterenlikht, J. R. Yates, E. A. Patterson and P. J. Withers. Crack monitoring around a hole under mixed mode (I + II) loading by image correlation. In: Crack Paths, 14-16 September 2006, Parma, Italy. Paper invited for special issue of Engineering Fracture Mechanics.

- P. López-Crespo. Fatigue and fracture assessment with image correlation. Winner of the Young Stress Analyst Competition of the 6th International Conference on Modern Practice in Stress and Vibration Analysis, 5-7 September 2006, Bath, UK.

- A. Shterenlikht, P. López-Crespo, P. J. Withers, J. R. Yates and E. A. Patterson. Mixed mode (I + II) stress intensity factor measurement using crack tip displacement fields acquired by image correlation. In: Proceedings of the 16th European Conference of Fracture, 3-7 July 2006, Alexandroupolis, Greece.

- P. López-Crespo, A. Shterenlikht, E. A. Patterson, J. R. Yates, P. J. Withers and R. Burguete. Towards real time crack monitoring using image correlation. In: Proceedings of the Society for Experimental Mechanics Annual Conference and Exposition, 4-7 June 2006, St Louis, Missouri, USA.

- A. Shterenlikht, P. López-Crespo, P. J. Withers, E. A. Patterson and J. R. Yates. Crack monitoring based on image correlation. In: Proceedings of the 9th International Fatigue Congress, 14-16 May 2006, Atlanta, Georgia, USA.

-A. Shterenlikht, F. A. Díaz Garrido, P. López-Crespo, P. J. Withers and E. A. Patterson. Mixed mode (KI + KII) stress intensity factor measurement by electronic speckle pattern interferometry and image correlation. In: M. Lucas, editor, Advanced Materials, Vol.1-2, pages 107-112, Switzerland, 2004. British Society for Strain Measurements, Trans Tech Publications Ltd.

- A. Shterenlikht, F. A. Díaz Garrido, P. López-Crespo, P. J. Withers and E. A. Patterson. SIFs from strain fields using ESPI and image correlation. In: Proceedings of the Society for Experimental Mechanics 10th International Congress and Exposition on Experimental and Applied Mechanics, Paper 100, Session 105, 7-10 June 2004, Costa Mesa, California, USA.

The following papers are in preparation at present:

- P. López-Crespo, A. Shterenlikht, E. A. Patterson, J. R. Yates and P. J. Withers. Stress intensity factor determination by image correlation. Experimental Mechanics.

- A. Shterenlikht, P. López-Crespo, E. A. Patterson, P. J. Withers and J. R. Yates. Determining stress and K from displacement fields using Muskhelishvili approach. International Journal of Fracture.